NORTHWESTERN UNIVERSITY

Numerical and Experimental Study of Aperture Based Laser Induced Forward Transfer Technique

A DISSERTATION

SUBMITTED TO THE GRADUATE SCHOOL
IN PARTIAL FULFILLMENT OF THE REQUIREMENTS

for the degree

DOCTOR OF PHILOSOPHY

Field of Civil and Environmental Engineering

By

Li Zhang

EVANSTON, ILLINOIS

December 2018

ABSTRACT

Numerical and Experimental Study of Aperture Based Laser Induced Forward Transfer Technique

Li Zhang

Additive manufacturing (AM) processes have advanced rapidly over the last three decades to the point where they have the potential to fundamentally change the way complex parts will be designed and fabricated in the future. Additive methods leverage the ability to join metal particles or molten droplets in a layer-by-layer fashion, allowing for efficient use of raw materials, to minimize waste, and enable cost effective production. Among the existing metal AM techniques available in the literature, the laser induced forward transfer (LIFT) technique is one of the notable methods well suited for three-dimensional (3D) printing of metal structures at the microscale. In the technique, a metallic donor thin film is locally melted by a pulsed laser, and small molten droplets liberated from the film are re-deposited on a target substrate in a layer-by-layer fashion in order to print a 3D object. The minimum feature size of the printed object is limited by a combination of the size of the metal droplets ejected from the donor film and the poor landing accuracy of droplets on the target substrate.

In this project, the droplet size and landing accuracy achievable in the LIFT technique will be controlled through the use of patterned micron sized apertures in the donor. The aperture provides two functionalities, (1) the aperture size will control the droplet size, and (2) the aspect ratio will facilitate the formation of vertical liquid jets that promote highly directional ejection of single droplets from the apex of the jet. The objective of this project is to study the hydrodynamics of the liquid jet growth through the donor film aperture, and the ejection of the droplets from the apex of the jet. Specifically, multi-physics (laser heating and fluid dynamics) based numerical models are

developed to investigate the transient heating and jetting hydrodynamics of liquid jets from high aspect ratio apertures in the donor film material. Furthermore, the modeling work is complimented with experimental results in patterned copper donor films, where transfer of micron sized single and multiple droplets are demonstrated. The modeling work facilitated the understanding of laser heating and molten metal hydrodynamics under different conditions, laser fluence, donor film thickness, flow velocity, and surface.

The aperture based LIFT approach has the potential to enable voxel-by-voxel printing of metal micro- and nanostructures, which can open up new opportunities to fabricate complex nanostructures comprised of inhomogeneous properties, and 3D anisotropic structures with spatially varying properties.

ACKNOWLEDGEMENT

I would like to thank my advisor, Dr. Balogun for his invaluable guidance, patience and support throughout the course of this research. This research would not have been possible without his thoughts and financial support.

I would also like to thank my committee members, Dr. Krishnaswamy and Dr. Wagner for their serving on my committee for their vision and thoughts. Thanks are also extended to the faculty and staff at Northwestern University for providing the friendly academic atmosphere for my study.

I would like to show my gratitude to my colleagues, Dr. Joel Fenner, Dr. Matt Ford, Dr.Jun Zhu, Jialun Han, Hong-cin Liou, Baojie Lu for their friendly suggestions during this research. Furthermore, my appreciation is extended to my friends Yaxin Cai, Pan Zhang, Yi Yang, Jialiang Wang who helped me to go through the 5-year study.

Last but not least, I would like to thank my grandparents who raised me up. Thanks also extend to my father and my mother for their constant support.

TABLE OF CONTENTS

LIST OF FIGURES

Chapter 1

Introduction

Additive manufacturing (AM), colloquially described as “3D printing” is a topic of broad interest in my disciplines. The technology has advanced over the last two decades to the point where they have the potential to fundamentally change the way complex parts will be designed and fabricated in the future. AM allows for fabrication of three dimensional objects of near-arbitrary shapes, sizes, and material constituents from a computer-generated model of a finished product, by joining materials in a layer-by-layer fashion [1-4]. Unlike conventional subtractive manufacturing techniques, such as machining, stamping, etc, AM allows for efficient use of raw material, minimizes waste, and enables cost effective production. Integration of AM with computer-aided technologies offer new opportunities to produce objects with complex geometries, and manufactured components can be tailored to design needs and client demand. For example, replacement parts for, military weapon systems, commercial land, air, and marine vehicles can be fabricated on site, and medical parts can be produced using patient specific anatomical information. The ability to manufacture products near customers with AM has the potential to impact the supply chain by reducing costs associated with warehousing, transportation, and packaging. In 2017, the 3D printing market generated a revenue of about 8.8 billion, which is projected to expand to 26.5 billion by 2021, as shown in Figure 1. 1.(The data is obtained from Statista)

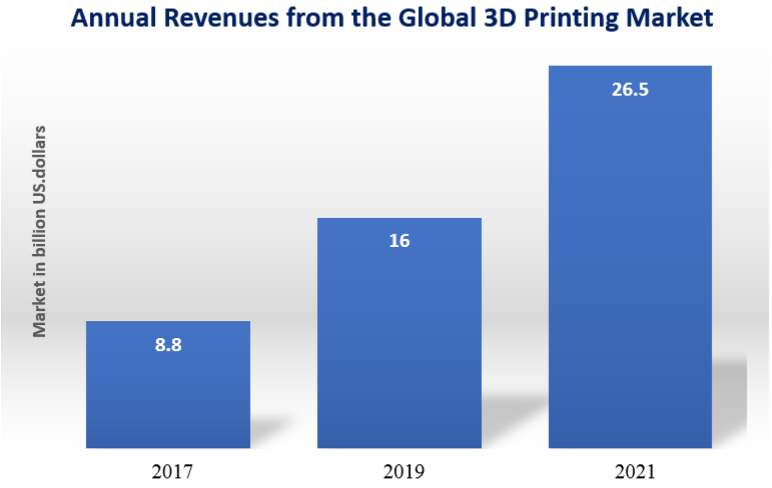

Source: Oerlikon

Figure 1. 1: Annual revenues from the global 3D printing market. Data obtained from Statista.

AM has been used for printing a wide range of materials including plastics [5,6], metals [7,8], biomaterials [9,10], ceramics [11], wax [12], etc. The state of most used AM printing material is shown in Figure 1. 2. It can be noticed that, currently, plastics are the most common 3D printing material, and these products have reached the level of customer satisfaction. Metals AM can be used to fabricate parts for aircraft engines [13] and automobiles [14], and biomedical implants in the healthcare industry [15]. Unlike plastic AM, which now mainstream, metal AM processes due to its complex material and process physics, is still in the research stage. To better understand the needs of metal 3D printing, it is important to examine the three main categories of AM techniques, which include the powder, wire, film based processes.

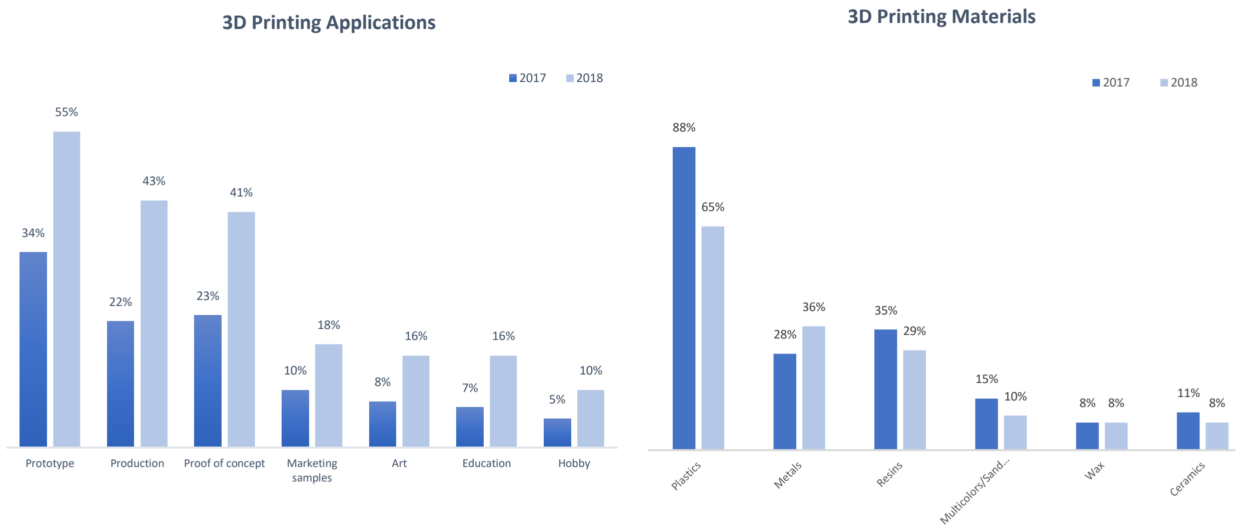

Figure 1. 2: 3D printing applications and material in 2017 and 2018.

Data obtained from Statista

1.1 Powder Based Metallic Additive Manufacturing

1.1.1 Powder bed system

The powder based system is illustrated in Figure 1. 3. In this system, metal powder is fed into hopper and a rake spreads the powder across a build platform. A laser or local thermal source scans the surface build platform guided by digital computed aided design(CAD) file of the final printed product, and selectively heats and melts the metal powder, fusing into the layer of particles below, as melt front cools down. The selective heating, melting, and fusion process continues in a layer-by-layer fashion until the three-dimensional component is completed. Typically, each layer is between 20-100 μm thick, depending on the metal particle size. At end of the process, the fused product is removed from unmelted loose powder bed and subjected to further post-processing methods. The powder bed AM approach offers several advantages including, printed features with high resolution details, internal passages, and strong dimensional control. Furthermore, the build chamber in this process is typically maintained in inert environment to protect the metal powders from oxygen contamination and maintain consistency of the melt pool temperature during the build. However, the final printed product may be porous due to the presence of lack of fusion disbands and air-voids, which reduce the mechanical integrity of the product. Selective laser sintering (SLS) and selective laser meting (SLM) are two examples of power bed based metal AM processes. Power bed AM printing equipments are now commercially available.

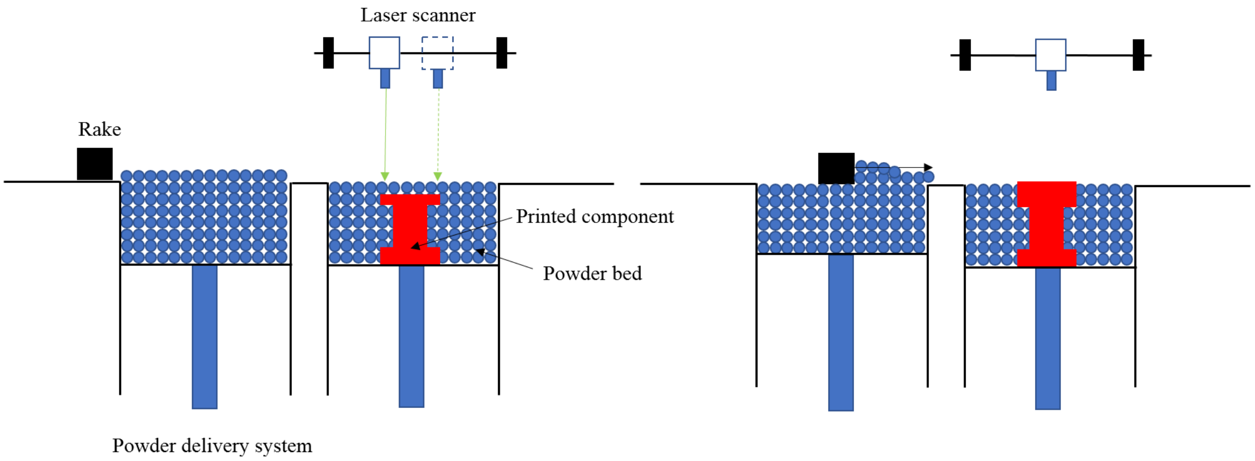

(a). Laser scanning on powder bed (b). Powder delivering to powder bed

Figure 1. 3: Schematic illustration of powder bed system

1.1.2 Powder fed system

The powder fed system, also known as laser metal deposition (LMD) or direct energy deposition (DMD) method, allows for precise deposition of materials layers with thinckness in the range of 0.1 mm to several centimeters. The processes involved in the powder fed system are illustrated in Figure 1. 4. In this process, metal powder is sprayed on build substrate through an oblique inclined nozzle, and a process laser is rastered scanned on the build plane to heat and melt the particles, following the 3D CAD file of the intended final product. The melt pool solidifies to produce a fused solid film on the substrate. A new batch of metal particles are then deposited on the solidied layer and melted with the laser to produce a new layer. The layered powder deposition and melting process is repeated until the 3D object is printed. One major advance of the powder fed system is that it allows for addition of material layers or coatings to existing products that may be damaged. As such, it facilitates the repair of expensive metal products like chipped turbine blades, and forming tools. The approach also shares the limitations of the power bed system stemming from the porosity of the finished final product.

1.2 Wire based Metal Additive Manufacturing

The wire based metal AM process uses wire feedstock as the raw material and the final product is created by heating the wire in controlled steps using an electron beam. The approach is illustrated in Figure 1. 5. Other energy sources like, lasers or plasma arcs can also be used. Initially, a single bead of material is deposited on the target substrate in a vacuum controlled environment, and multiple beads layers are fabricated in a layer-by-layer fashion. In general, wire feed systems are well suited for high deposition rate processing; and offer a low cost option as compared to the powder based approaches due to the availability and cost of the metal wire feedstocks compared to the powder raw materials. Significant quality control is needed to achieve high quality printed parts. The fabricated product usually requires more post processing steps compared to the powder bed or powder fed systems.

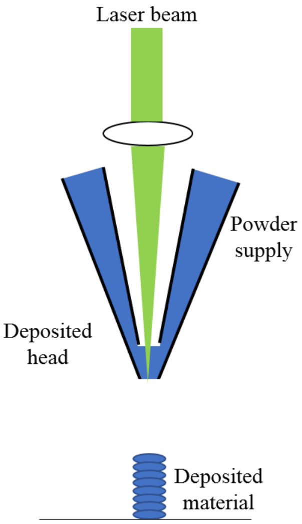

Figure 1. 4: Schematic illustration of LMD

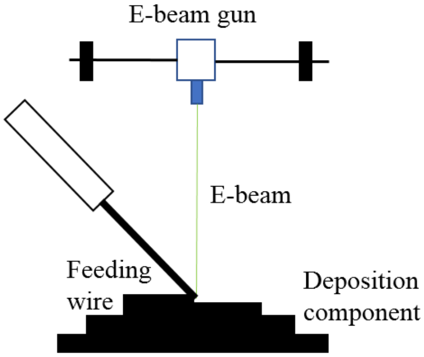

Figure 1. 5: Schematic illustration of wire feed system

1.3 Thin Film Based Metal Additive Manufacturing

1.3.1 Conventional Laser induced forward transfer

The laser induced forward transfer (LIFT) technique facilitates 3D printing of metal structures at the microscale based on thin metal film feedstocks. This technique was first proposed and demonstrated by Bohandy *et al.* [16] in 1986. The LIFT technique uses pulsed lasers to print metal structures on a target substrate by assembling molten droplets in a layer-by-layer fashion. The processes involved in the LIFT process are schematically illustrated in **Figure 1. 6**. In the LIFT process, the interface between a thin metal film (donor) and a transparent carrier substrate is irradiated by a pulsed laser, where the laser energy is absorbed by the film leading to localized heating. A small portion of the donor layer close to the substrate is melted and possibly vaporized, depending on the input laser energy. The melt front propagates to the donor film surface, where a molten liquid jet is formed. At a critical threshold laser energy, where the inertia force on the liquid jet overcomes the surface tension at the apex of the jet, single or multiple droplets of molten metal are pinched off from the liquid jet and deposited on the target substrate. The heating and droplet transfer process is repeated by translating the carrier substrate to stack droplets on top of each other, which upon cooling, solidify to form vertical metal structures. Alternatively, the laser is scanned to deposit droplets laterally on the target substrate, allowing for printing of structures in a layer-by-layer fashion. The technique has been used for printing a wide range of materials including, deoxyribonucleic acid (DNA) [17], biomaterials [18], polymers [19, 20], pure metals [21, 22], particles [23], graphene [24], semiconductors [25], and organic dielectrics [26]. Recent demonstrations of LIFT-based metal deposition of single droplets [27,28], lines [29, 30], and high-aspect ratio micron scale pillars [31] by stacking micron scale droplets, point to a promising future for three-dimensional (3D) AM applications including, the filling of through-silicon vias for electronic interconnects [32], fabrication of microscale antennas structures, out-of-plane electrodes, etc. The size and quality of LIFT parts depend on the laser spot size and duration, the input laser fluence, and the dynamics of the heating process and the hydrodynamics of the melt zone. Nanosecond lasers, for example, allow for uniform heating of the metal film feedstock, and provide large energy per laser pulse sufficient to melt the donor film, and eject molten droplets towards the target substrate. However, variations in the pulse energy from shot to shot makes it difficult to control the size of the melt zone, the flow dynamics of the molten film, and the landing accuracy of the ejected droplets. Ultrafast lasers with duration in the picoseconds and femtoseconds range, facilitate the reduction in the heat penetration depth in the donor film, making it possible to work with thin donor films, leading to small ejected donor droplets. The use of ultrafast lasers leads to high cost manufacturing costs and the poor landing accuracy of the ejected droplets is sometime overcome by the use of short offset distance (in the micron range) between the donor film and target substrate.

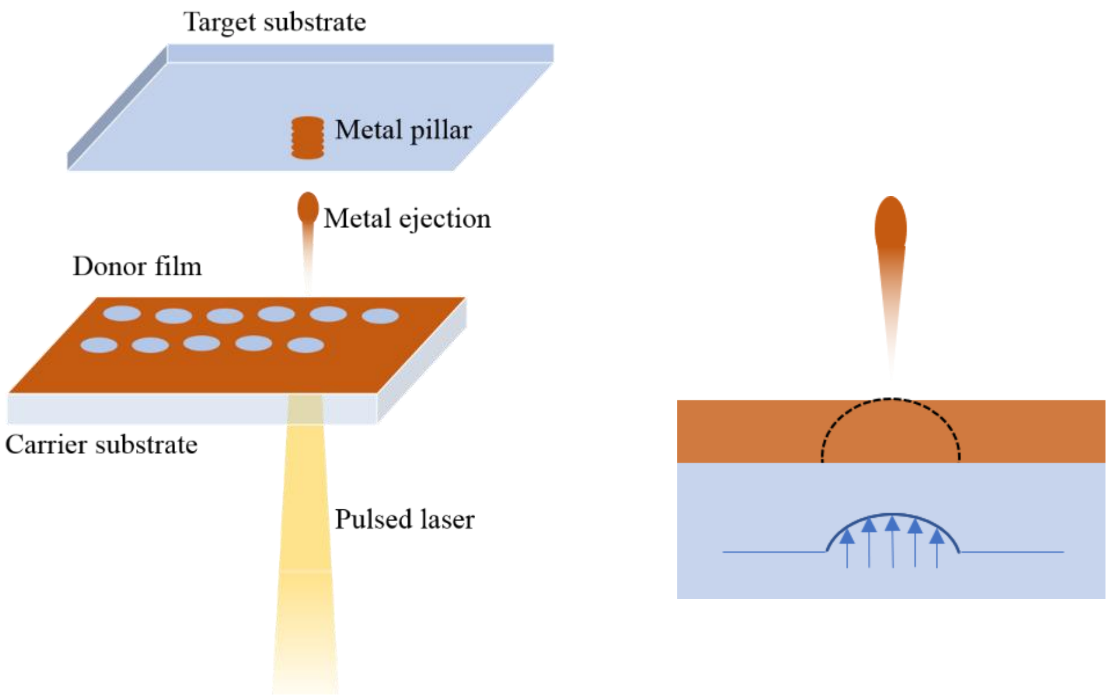

(a) 3D LIFT process (b) 2D LIFT process

Figure 1. 6: Schematic illustration of LIFT process

1.3.2 Patterned laser induced forward transfer

Previous work in the literature suggest that the droplet landing accuracy is strongly influenced by the pulse laser fluence (energy per pulse), thickness of the donor layer, and the donor-target separation distance. *The droplet size and landing accuracy can be controlled with the use of patterned apertures in the donor film or a capping layer that acts as mask. The central hypothesis driving the proposed approach is that the aperture will provides two functionalities, (1) the aperture size will control the droplet size, and (2) the aspect ratio of the aperture will control the direction of the ejected droplets.* In this work, we modify the conventional LIFT approach by patterning micron-sized apertures in the donor film to control the size of molten droplets transferred to the target substrate. The ability to control the droplet size using the LIFT technique is relevant in, photonic applications where plasmonic antennas that efficiently confine light within ultra-small volumes are achieved using metal particles with nanoscale dimensions, and micro-ballistic impact studies where micron-sized particles are used as hypervelocity projectiles. In particular, the ability to create particles of different sizes and composed of different materials can diversify current micro-ballistic impact studies of materials to include, projectile-size-dependent and projectile-material-dependent investigations. Aperture controlled droplets are an integral aspect of the conventional LIFT process. For example, Zenou *et. al.* [33] showed that at moderately low input laser fluence, the donor film melts from the film-substrate interface to the free surface of the film without experiencing vaporization, and the intersection of the melt front and free surface creates an aperture through which droplets can be transferred to the target substrate. One advantage of aperture-based droplet ejection is the ability to transfer droplets with low angular divergence angle to a target substrate, and with a large offset distance (~ 1 mm) between the donor film and target. Consequently, the landing accuracy of the droplets on the target substrate can be well controlled. The aperture size obtained in conventional LIFT processes is limited by the heating dynamics of the donor film, and the input laser source parameters (spot size, fluence, and pulse duration). Alternatively, the droplet size can be controlled by the use of apertures in a mask layer covering the donor film. These apertures can be directly patterned on the donor film by standard lithographic processes, as demonstrated in this work, or fabricated in a capping layer with a higher melting point than the donor film as illustrated in Figure 1. 7.

The aperture based LIFT approach has the potential to enable 3D printing to metal-based nanophotonic devices including, optical metamaterials that exhibit negative permittivity and permeability at the visible wavelengths in the electromagnetic spectrum, sensors based on periodic arrays of metal nanowires and nanoantennas, metal-interconnect wires, etc. Unlike standard lithographic methods, which allow for 2D metal printing, the proposed technique will enable the printing of high aspect ratio. Furthermore, the proposed approach has the potential to enable voxel-by-voxel engineering of metal nanostructures. This can open up new opportunities to fabricate complex microstructures comprised of inhomogeneous (compositionally graded) by patterning the donor film with different metals, and creating 3D structures with anisotropic density by controlling the overlap between ejected droplets on the target substrate leading to spatially varying porosity. The ability to create porous metal architectures with local properties at the scale of a few droplets can increase the degrees of freedom in designing new ultralight materials [34] with unique thermal, mechanical, and electrical properties.

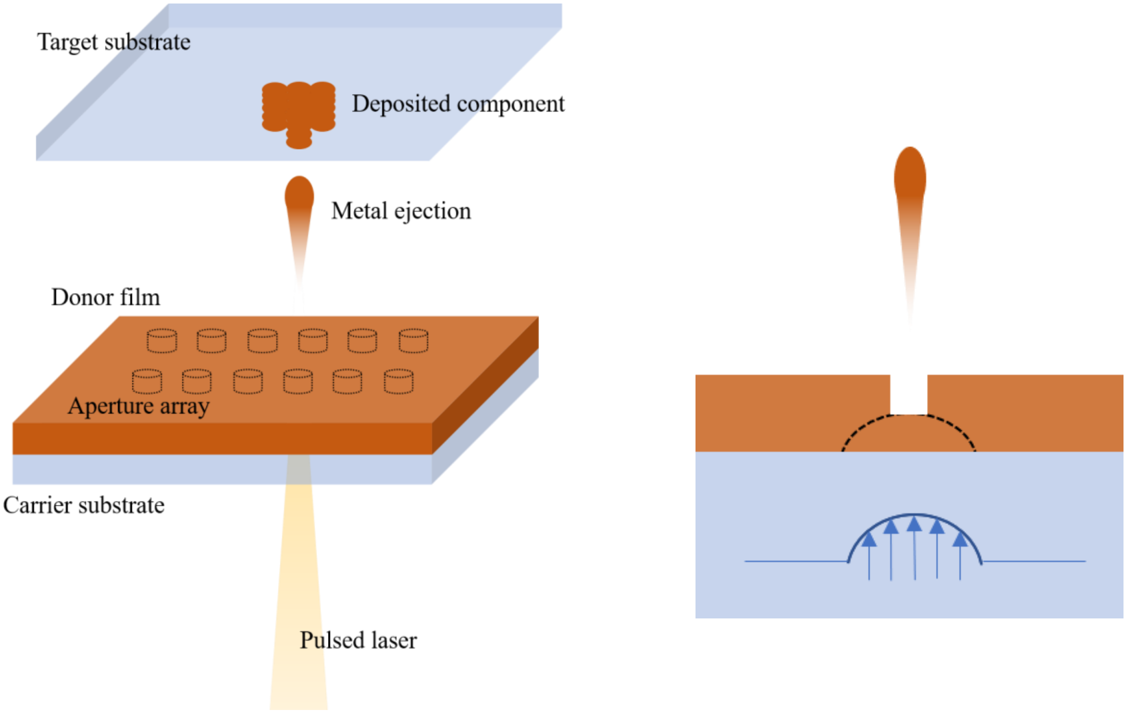

(a)3D patterned LIFT process (b)2D patterned LIFT process

Figure 1. 7: Schematic illustration of patterned LIFT process

1.4 Research objective

Fabrication of desired metal micro- and nanostructures based on the LIFT technique requires a quantitative understanding of local transient heating and deformation of the donor film, and the jetting dynamics of melted droplets. This will be achieved in this project by numerical simulation of pulsed laser heating process, interaction between the moving molten and vaporized portions of the donor film, and the unmelted solid donor film structure, and the jetting hydrodynamics of the individual droplets from apertures in the donor film. Accomplishing these tasks will enable prediction and control of the growth of LIFT fabricated micro- and nanostructures. The knowledge gained from studying the influence of critical parameters such as laser fluence, donor film properties, donor-target separation, etc., on the droplet size and ejection hydrodynamics, will facilitate efficient selection of process parameters prior to performing experiments to fabricate the metal structures of desired feature sizes at micron and nanoscales, and to control the deposition direction and angle of the ejected droplets. Control of the fabrication process using the numerical modeling and experimentation components of the project will facilitate overcoming critical technical barriers to micro- and nanoscale AM using the LIFT approach, and achieving the goal of voxel-on-demand printing of individual droplets, which is a requirement for layer-by-layer fabrication of complex structures made of interconnected metal intricate parts. The following technical tasks are accomplished in this dissertation,

Task 1: Numerical investigation of the heating dynamics involved in LIFT Processes

LIFT technique has received a lot of attention, researchers have achieved deposition of silver nanopastes, copper pillars, aluminum micro-structure, liquid propelling and DNA/drug delivery. However, the basic mechanism for the LIFT process is still unclear. A.I. Kuznetsov *et al.* [27] proposed that the relaxation of thermally induced stress is the responsible mechanism for the ejection; D.A.Willis *et.al* and L.Zentrum *et al.* [35,36] has confirmed that hydrodynamics of the molten material is the major concern, and M.Martin *et.al* [37] claim that influence of vaporized bubbles in the melt pool as the driving force for droplet ejection. In this task, a finite different model is explored to study the heating, melting, and vaporization history of a donor film resulting from irradiation by nanosecond pulsed laser. Details of the phase change within the heat-zone will provide important information for the associated flow hydrodynamics of the molten metal.

Task 2: Numerical investigation of melt pool hydrodynamics in the presence of an aperture

This task involves the fluid dynamics of the laser melted donor film, the physics of the liquid jets formed in the presence of an aperture in the donor film, and the ejection dynamics of molten droplets from the apex of the liquid jet. This study will be conducted under different fluid parameters, controlled by the Reynolds and Weber number of the molten metal, and the geometry of the donor film aperture.

Task 3: Experimental analysis of conventional and proposed LIFT processes

This task involves a detailed experimental comparison of features produced by the conventional and proposed LIFT processes under different processing conditions –laser fluence, donor film thickness, and aperture geometry. The experimental results will also provide a means of validating the numerical calculations.

1.5 Outline of this dissertation

Chapter 1 provides a background of metal additive manufacturing processes and lay out the technical problem that is addressed in this dissertation. Chapter 2 provides a review of the state-of-the art of the LIFT technique. Chapter 3 describes a numerical analysis of the heating dynamics of the donor film based on the solution to 2D axisymmetric heat conduction equation. The numerical analysis addresses the temperature change resulting from local irradiation by a single laser pulse, the corresponding phases change that can occur with laser fluence and small film thicknesses. The analytical results are used to identify the regimes favorable for controlled-uniform melting of the donor film by a nanosecond pulsed laser. Chapter 4 focuses on the melt pool hydrodynamics. A numerical solution to Navier-Stokes equation is explored to understand the flow dynamics of the molten metal, the formation of narrow liquid jets through an aperture, and the fluid instability that leads to the pinch of droplets from the liquid jet. In particular, two modes of liquid jet formation are identified, namely, the dripping or jetting mode, depending on the velocity of the molten metal. Parametric studies of the jetting dynamics are presented to describe the influence on the droplet size and velocity on ejected droplets in the two modes. Chapter 5 provides experimental results on the pulsed laser transfer of droplets from thin copper films on a fused silica substrate, using the conventional LIFT and proposed approach. The chapter details the unique features of the LIFT process achieved with an aperture in the donor film. Chapter 6 provides a summary of key accomplishments and knowledge gained from the aperture based LIFT approach, and suggestions for future research endeavors.

Chapter 2

Review of the State of the art of the LIFT Process

2.1 Introduction

The LIFT technique was originally proposed by Bohandy *et al.* [16] as a local deposition approach, in which a metal film on an optically transparent substrate is ablated by a high power pulsed laser, and the resulting molten droplets are re-deposited on a substrate in close proximity to the film. Compared to other thin film deposition methods, the LIFT technique offers the advantages of great simplicity, it does not depend on the optical and thermal properties of the target substrate, special lithographic processing of the substrate is not required, and processing under atmospheric conditions is possible. Following the seminal work of Bohandy *et al*. [38] in which, micron wide copper lines were printed on a silicon substrate, variations of the LIFT approach have merged, motivated by the need to broaden the range of printable film materials, to minimize the defect content of the printed films, and to improve the minimum size of droplets that can be deposited on the target substrate. The following sections provide background description of the state of the art of LIFT processes in three categories: LIFT of solid materials, LIFT of liquid materials and LIFT of solid materials in liquid phase.

2.2 LIFT of solid materials

Figure 2. 1 illustrates the processes involved in the solid phase LIFT technique. A pulsed laser irradiates the donor film through a transparent carrier substrate, where the film is not only melted, but also partially vaporized. Vaporization of small amount of the donor film leads to the formation of trapped gas at the interface between the donor film and glass substrate. The resulting cavity pressure leads to blistering of the un-melted solid donor film, and when the shear force at the perimeter of the blistered film exceeds the film shear strength, the solid film is released from the

carrier substrate and accelerated towards the target substrate as a solid pellet. Owing to large inertia force involved in the process, the ejected pellet can disintegrate upon landing on the target substrate. In addition, the circumferential shear forces on the blistered film leads to varying rupture patterns and different pellet shapes. For thin donor films, it is also possible to melt the film completely without ejection of the solid pellets. It is therefore desirable to control of the ejection of the solid pellets by other means, such as, stress loading of the un-melted film interface as demonstrated by Shugaev *et. al.* [39], or to control of the shape of the solid pellets by shaping the spatial intensity profile of the pulsed laser source[40,41]. Other approaches have also been explored by various authors to overcome the short comings of the solid-phase LIFT techniques. For example, one variant of the LIFT approach, called the Laser-induced Thermal Imaging (LITI) was reported by [42]. In this technique, an optically absorbing sacrificial layer is moderately heated and the target substrate is placed in contact with the donor layer. Upon heating the absorbing layer, its adhesion to the donor film decreases, leading to stamping of the donor film on the target substrate. In addition, Banks *et al*. [43] introduced the "Ballistic Laser Assisted Solid Transfer (BLAST)" method, in which the pulsed laser is defocused at the interface between the donor-film and carrier substrate to achieve irradiation shapes with stronger intensity around the circumference of the laser beam, thus leading to smaller forces around the blistered edges of the donor film.

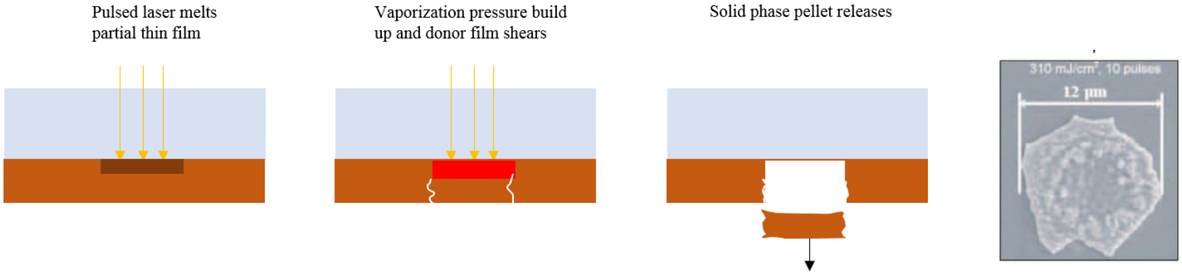

(a) (b)

Figure 2. 1: (a). Schematic illustration of solid phase LIFT mechanism (b) deposited Cr pellet on target substrate [43]

Rapp *et al.* [40] reported a mask-based Smart Beam Shaping approach, where the irradiation pattern is optimized to achieve strong intensity concentration around the circumference of the laser beam. The mask-based approach provides broad versatility in engineering different laser beam patterns, some which are shown in Figure 2. 2a. Recently, Pohl *et al.* [41] explored a liquid-crystal spatial light modulator (SLM) to generate grayscale spatial intensity distribution profiles that allowed for the ejection of pellets with controllable shapes. Pohl *et al.* [41] were able to transfer solid-phase pellets with complex shapes from a 100 nm gold donor layer, as shown in Figure 2. 2b.

The conventional LIFT cannot be applied to transferring delicate materials. To overcome this problem, Tolbert *et. al.* [44] developed the Dynamic Release Layer (DRL) LIFT approach, which allows for shielding the donor layer from adverse heating effects. In DRL-LIFT, an optically absorbing film, called the DRL, is sandwiched between the donor film and the transparent carrier substrate. Pulse laser heating and partial vaporization of the DRL leads to the generation of a confined high pressure blister cavity that spontaneously launches the donor layer towards the target substrate. With the DRL-LIFT approach, arbitrary donor materials can be used including, polymers [45,46], liquids [47], high and low viscosity pastes [48], living cells [49], etc. A particularly well suited material for a sacrificial layer is triazene polymer, which has a low ablation threshold and can be decomposed into small gaseous fragments, providing the necessary propelling force for transferring of solid phase droplet. One drawback of the DRL approach is the possibility for contamination of the deposited materials by the intermediate layer.

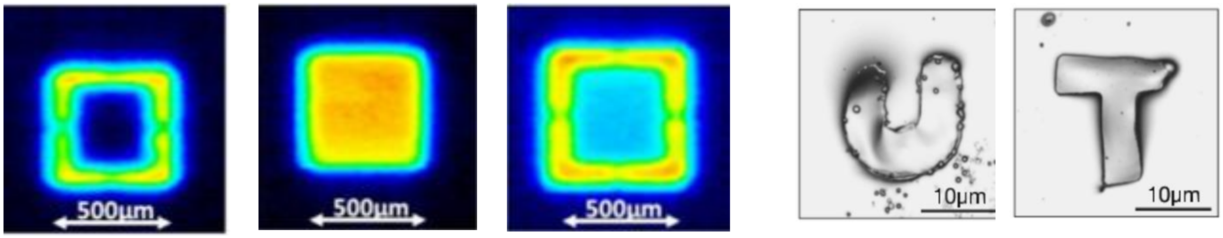

Laser profile #1 Laser profile #2 Merged laser profile

(a) (b)

Figure 2. 2: (a) The laser itentisy profile after mergence [40] (b). Two desired pellet shape[41]

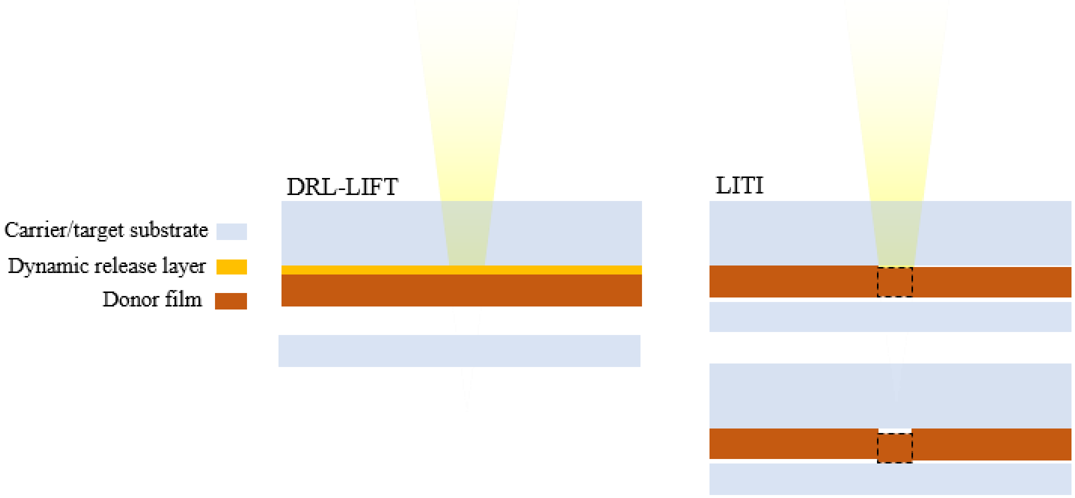

(a) (b)

Figure 2. 3: Schematic illustration of DRL LIFT and LITI

2.3 LIFT of liquid materials

The central feature distinguishing solid and liquid phase LIFT is nature of the transferred material to the target substrate. In the latter, liquid droplets from the donor film are transferred to the target substrate, where they are assembled in a layer-by-layer fashion to build the final product. A simple illustration of processes involved in the transfer of liquids in the LIFT approach is illustrated in the work of M. Duocastella *et al.*[50], where the transfer of droplets from a liquid solution comprised of a mixture of water and glycerol and sodium dodecyl sulfate surfactant, to a target substrate, is visualized by time-resolved optical imaging at different laser fluences. This work showed that at low laser fluence, a needlelike liquid jet develops, and if the jet is not energetic enough to overcome the surface tension force, and it begins to recoil until it finally disappears. In this case, no droplet ejected from the jet. At high laser fluence, a bubble expands violently from within the liquid jet leading to bubble collapse and splashing of droplets on the target substrate. At an intermediate fluence, the bubble expands gradually, and the jet with sufficient inertia advances stretches and thins down, as illustrated in Figure 2. 4. Finally, when the liquid jet attains a critical length, it breaks up into droplets that are directed towards to the target substrate. Various materials including protein [51], DNA [52] and cells [53] have been successfully transferred based on the liquid-phase lift without a significant damage, using a sacrificial heating layer on which these materials are deposited.

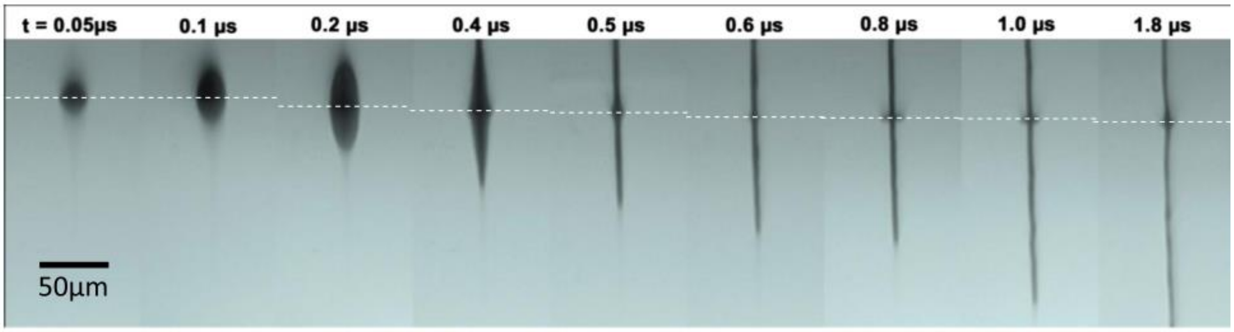

Figure 2. 4: Time resolved images of jetting at an intermediate fluence (5.6J/cm^2) [50]

Recently, the blister-actuated laser induced forward transfer (BA-LIFT) was developed by Brown *et.al* [54] for controlled transfer of liquid materials. In this technique, a thick polymide film serving as the UV optical absorption layer is used. A liquid layer is deposited on the polymide film. The latter is deposited on a transparent carrier substrate. Upon irradiation of the polymide layer, the film heats up and partially vaporizes, forming a sealed blister under the un-melted polymer. The transient movement of the polymer blister leads to the release of liquid droplets from the polymer surface. Figure 2. 5 shows time-resolved optical images of the formation of liquid jets, local thining around the apex of the jet, the formation of spherical droplets, and the breakup of the droplets from the polymer surface.

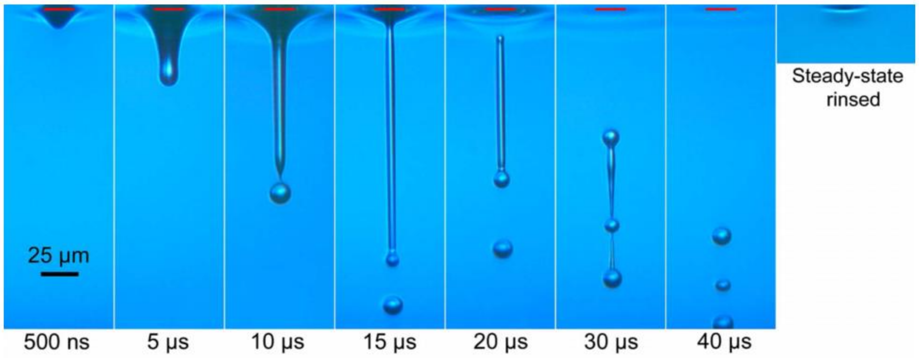

Figure 2. 5: Transfer from a 10µm film of NMP spread on 6 µm polyimide film with a 20 µm beam at 1.3J/cm^2 [54]

There are a few notable recent innovative technologies developed based on the concept of liquid phase LIFT. Amongst these includes a micro drug injector developed by Han *et.al*.[55], illustrated in Figure 2. 6. A nanosecond laser pulse is focused in distilled water, inducing a plasma with high temperature and pressure. A bubble generated at the focal point expands and collapses violently, creating a shockwave through water. The shockwave propagates to a flexible membrane between the driving fluid and the drug, and the latter is transferred by the mechanical pressure induced by the mechanical wave. In practice, the shockwave on the membrane generates liquid microjets that propel the drug through a micro-nozzle towards the intended target. The authors used this technique to deliver black ink into fatty pork tissue.

The majority of the liquid phase LIFT techniques rely on the use of pulsed lasers. P. Sopena *et al.* [56] recently showed that continuous wave (CW) lasers can be used for printing liquid inks. This technique is significant due to the low cost of CW lasers and good quality of the printed materials. P.Sopena *et al.* printed silver conductive lines with good electrical properties. Optical imaging of the drop ejection dynamics revealed significantly difference from the pulsed laser based LIFT approaches.

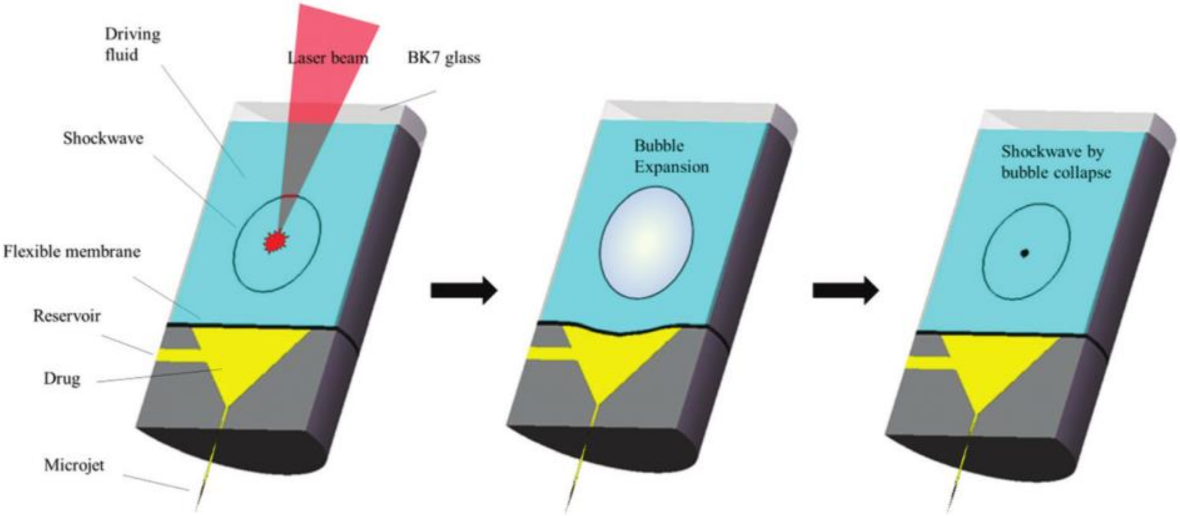

Figure 2. 6: Schematic illustration of LIFT based drug delivery process [55]

2.4 LIFT of solid in liquid phase

One of the most important applications of LIFT is for fabrication of metallic micro-and nanostructures. Unlike the previous approaches used for transfer of liquid inks and solvents, metal droplets can be generated directly melting the donor film with the pulsed laser. Individual droplets are ejected from the molten metal by control of the inertia and surface tension forces on molten metal. For this approach to work, proper selection of the laser fluence, pulse duration, and donor film thickness is needed to avoid unwanted temperature gradients and stresses in the melted film. Banks *et al.* [28] transferred small droplets of chromium with diameter of close to 300 nm to target substrate. In their work, an ultrafast pulsed laser with duration in the femtosecond range was used to melt the thin chromium donor film. Although ultrafast lasers are more expensive compared to nanosecond lasers, the short duration of the laser limits the heat penetration in the donor film and the heat affected zone. The pulse energy has limited amplitude variation from laser shot to laser shot, thus facilitating reproducible deposition of droplets on the target substrate. Furthermore, the low laser fluence allows for working below the vaporization threshold of the donor film. The work of Banks *et al.* [28] demonstrates the capability of the LIFT technique for printing individual droplets with sub-diffraction limited diameters, much smaller than the size of the pulsed laser. This work represents the state-of-the art of LIFT transferred droplets in the literature.

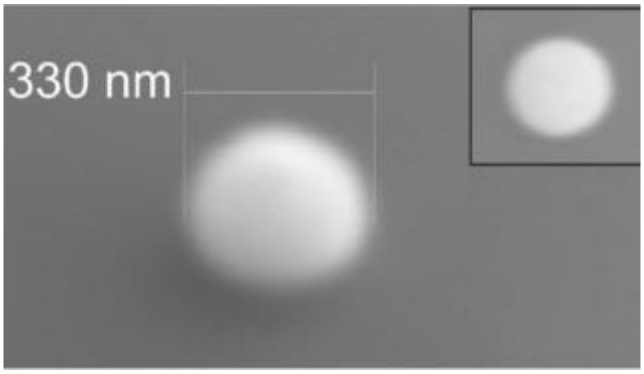

Figure 2. 7: SEM of a Cr deposit at laser fluence of 325mJ/cm^2 [28]

Visser *et al.* [31] reported the fabrication of 3D vertical copper micro-pillars, illustrated in by stacking multiple droplets on top of each other, using a femtosecond laser. In their experiments, the target substrate was held stationary, while the donor film was translated between successive pulsed laser exposures. The morphology of the micro-pillars was found to depend strongly on the impact velocity of the droplets, which is controlled by the laser fluence. Furthermore, the unpredictable ejection trajectories of the molten droplets was avoided by limiting of the offset distance between the donor film and target substrate. Figure 2. 8 shows printed copper pillars with an aspect ratio's of up to 400, where the diameter is below 5 μm and length is up to 2mm. The pillars are shown to have low porosity, strong electrically conductivity, and mechanically homogeneity.

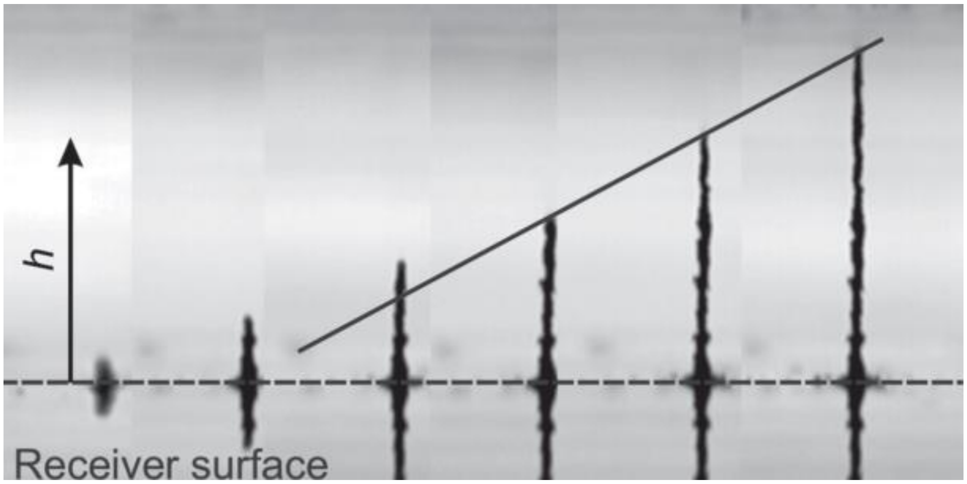

Figure 2. 8: Snapshots of copper pillars [31]

Kuznetsov *et al.* [57] also reported a novel method for fabrication of large periodic arrays of nanoparticles based on a combination of LIFT and lithography. In their experiments, a hexagonal structure of gold triangles was first fabricated on a glass substrate by conventional lithographical method. Subsequently, ultrafast laser pulses with duration of close to 30 femtoseconds irradiates several triangles, melting them, and ejected the droplets towards the substrate. The process is shown in Figure 2.9.

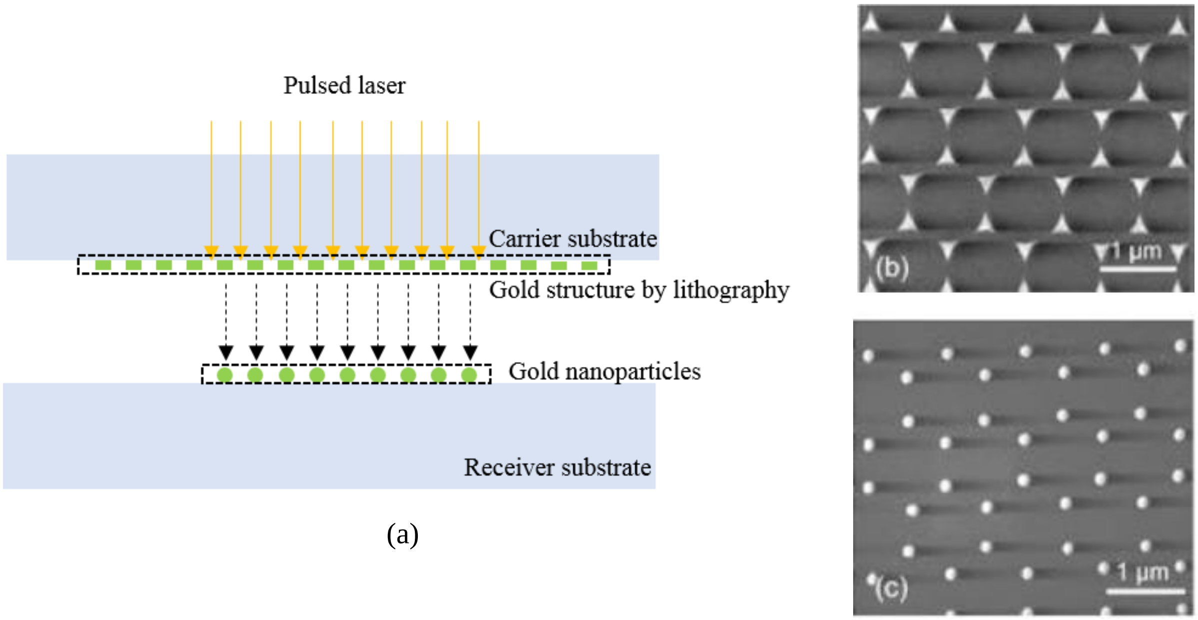

Figure 2. 9: (a) Schematic illustration of nanoparticle structure fabrication

(b) SEM image of gold triangles fabricated by lithography [57]

(c). SEM image of a nanoparticle array fabricated by a single laser pulse [57]

2.5 Aperture based LIFT of metals in liquid phase

So far, the minimum feature size of LIFT fabricated 3D metal structures is close to 5 µm, limited by the poor landing accuracy of ejected droplets on the target substrate. However, the diameter of the individual droplets can be in the submicron range. The droplet landing accuracy is strongly influenced by the input laser fluence and donor film thickness. Recently, Zenou et. al. [58-60] identified a regime of stable droplet ejection in the LIFT technique where well-directed jetting occurs, and is achieved close to a critical threshold fluence. This regime is the so-called thermally induced-nozzle (TIN) regime, where the laser generated heat diffusion length into the donor film is smaller than the film thickness. As such, the donor film is partially melted across its thickness. The melt front advances as a spherical front towards the free surface of the donor film. The intersection of the melt front and surface of the donor film creates a small quazi-nozzle that allows for ejection of liquid metal with low angular divergence over donor-target separation distances of up to 1 mm. Figure 3 shows SEM images of micron-sized quasi-nozzles formed in aluminum donor film by sub-nanosecond pulsed laser with duration of close to 500 picoseconds. Single and multiple droplet ejection from the nozzle can be controlled based on the laser fluence.

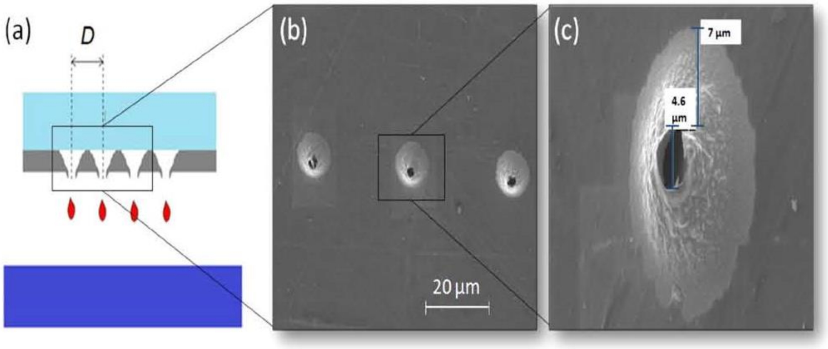

Figure 2. 10: (a) Schematic of a nozzle based directional ejection of molten droplets in the LIFT technique, (b) scanning electron microscopy images of thermally induced nozzle apertures in an aluminum donor film after printing, (c) magnified image of a single aperture.
Images were taken from [58].

2.6 Summary

The LIFT approach offers several unique advantages over the existing printing method such as fast printing speed, nano- and micron-scale metal droplets, bulk-like material properties of printed objects, and the ability to print combinations of metals and complex microstructures such as compositionally graded and anisotropic material properties. The aperture based LIFT approach allows for inexpensive operation with the use of the sub-nanosecond laser pulses, as compared to the expensive ultrafast lasers. However, what is unclear in the works of Zenou *et al.*[58-60], is how the thermal induced nozzle size can be controlled. Furthermore, the minimum feature size of the printed metal structures are in the tens of microns range. To address these limitations, this project seeks to control the feature size of deposited structures by patterning the donor film using micron- or nanoscale sized apertures and controlling the location of droplets deposited on the target substrate based on the aspect ratio of the aperture. This new approach will enable on-demand printing of single metal droplets and facilitate control of the feature size of metal structures.

Chapter 3

Heating Dynamics of a Donor Film in the Laser Induced Forward Transfer Technique

3.1 Introduction

Owing to the complex processes (heating, vaporization, flow, ejection *etc.*) involved in the LIFT method, the controlling mechanisms involved have been investigated using numerical techniques including the finite element (FE) and finite difference time domain (FDTD) methods. For ultrashort laser pulses with femtosecond and picoseconds duration, the heating and melting dynamics in metal films have been investigated using FDTD solution of the two-temperature model (TTM) for heat transport based on electron and phonon carriers. Using this approach, Shugaev *et al.* [39] demonstrated that impulsive generation of compressive elastic stress waves with short wavelengths follows the heating of the donor film, which upon reflection and mode-conversion from the free surface leads to the generation of tensile waves that releases the donor layer from the transparent carrier substrate without melting and vaporization, and ejecting it towards the target substrate. For high laser fluencies sufficient to produce donor film melting and vaporization, Willis *et al.* [35] developed a numerical model based on the volume of fluid method to account for laser absorption, heat transfer, phase change, and fluid flow processes that occur in the donor layer prior to material transfer to the target. In their model, phase change from solid to liquid occurs when the film temperature obtained from the solution to the classical heat equation exceeds the liquidous temperature.

3.2 Model description

A numerical model that predicts the temperature history of the donor film and carrier substrate, upon absorption of a nanosecond pulsed laser is described in this section. The geometry of the numerical model is shown in Figure 3. 1. Since the duration of the pulsed laser used in this work is longer than the time scale of electron-phonon relaxation in the metal film, we assume that the laser energy is absorbed in the donor film under conditions of thermal equilibrium and the thermal history of the film and substrate follows the classical heat equation. An axisymmetric classical heat equation is adopted, where the axis of symmetry is the *z*-axis, owing to the Gaussian spatial distribution of the input laser pulse. The heat equations for the donor film and substrate are formulated in cylindrical coordinates as ,

$$\rho_f \frac{dh(T_f)}{dt} = \frac{1}{r}\frac{\partial}{\partial r}\left(k_f(T_f) r \frac{\partial T_f}{\partial r}\right) + \frac{\partial}{\partial z}\left(k_f(T_f)\frac{\partial T_f}{\partial z}\right) + Q, \tag{3.1}$$

$$\rho_s \frac{dh(T_s)}{dt} = \frac{1}{r}\frac{\partial}{\partial r}\left(k_s(T_s) r \frac{\partial T_s}{\partial r}\right) + \frac{\partial}{\partial z}\left(k_s(T_s)\frac{\partial T_s}{\partial z}\right), \tag{3.2}$$

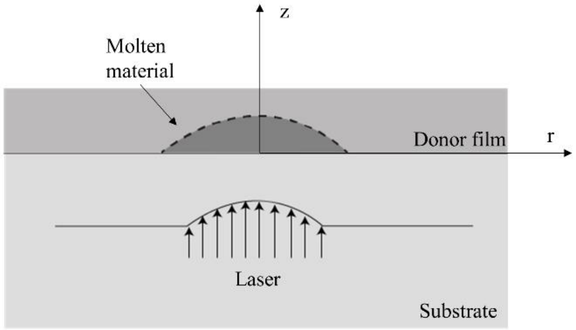

Figure 3. 1: Geometry of the numerical model

where *T* is instantaneous temperature, *ρ* is the material property, and *k* is the temperature dependent thermal conductivity, the subscripts, *s* and *f*, represent the substrate and film, *h* is the temperature-dependent enthalpy, the variable *r* represents the local radial distance from the center of the input laser spot, and *z* represents the local distance from the donor film and substrate interface. The use of the enthalpy based heat equation allows one to account for the change of phase as the donor film temperature goes through the melting or vaporization points, and to satisfy energy conservation at all times. The function Q in Eq. (3.3) represents the input heat source expressed below,

$$Q(r,z,t) = (1-R)\alpha \exp(-\alpha z)\, I_0 e^{\frac{-2r^2}{r_0^2}} e^{\frac{-(t-\tau)^2}{t_0^2}}, \tag{3.3}$$

where R and α are the donor film reflectivity and absorption coefficient, which depend on the wavelength of the laser, I_0 is peak laser intensity, and Gaussian functions are used to approximate the temporal and radial dependence of the intensity distribution characterized by r_0 and t_0, which are the spot size and pulse width of the laser source.

Boundary and initial conditions are imposed on the solutions to the heat equation. The initial temperature at any point in the film and substrate is assumed to be the same as the room temperature T_{room},

$$T_f(r,z,t=0) = T_s(r,z,t=0) = T_{room}. \tag{3.4}$$

At the interface between the donor film and the substrate, continuity of temperature and heat flux are imposed, as expressed below,

$$T_f(r,z=0,t) = T_s(r,z=0,t), \tag{3.5}$$

$$k_f \frac{\partial T_f(r,z=0,t)}{\partial z} = k_s \frac{\partial T_s(r,z=0,t)}{\partial z}. \tag{3.6}$$

Adiabatic conditions are imposed at the free surfaces of the film and substrate.

To account for phase change of the donor film, which leads to a reduction in the total energy in the system through the latent heat of melting L_m or the latent heat of vaporization L_v, the temperature dependent enthalpy for the different phases are described below,

$$h(T) = \int_0^T C_p(T)dT, \text{ for } T < T_m, \tag{3.7}$$

$$h(T) = \int_0^T C_p(T)dT + L_m, \text{ for } T_m < T < T_v, \tag{3.8}$$

$$h(T) = \int_0^T C_p(T)dT + L_v, \text{ for } T > T_v, \tag{3.9}$$

where T_m and T_v represent the melting and boiling point temperatures of the donor film. The heat equations are solved with the implicit backward finite difference time domain (FDTD) numerical simulation approach.

3.3 Validation of numerical method

Numerical results for the temperature and time-dependent position of the melt front in a copper half-space are validated against numerical results by Bogaerts *et. al.* [61] in Figure 3. 2. For the calculation from Bogaerts, *et al*. [61] the input laser has the following characteristics: wavelength=226 nm, pulse width=10 ns, peak intensity=10^9 W/cm^2. The input laser energy is absorbed at the free surface of the half-space. Due to the high input laser intensity used, a strong plasma is formed above the free surface, which shields the surface from continued absorption of the laser energy for a portion of input pulse laser duration. This ultimately modifies the temporal profile of the absorbed laser energy. The same laser intensity profile, after the laser passes through the plasma plume, is applied in our calculation. In addition, the same temperature dependent material properties are used. The numerical results show that the surface temperature rises rapidly from room temperature to a peak value close to 6700 Kelvin within 10 ns and then reduces gradually due to heat conduction into the half-space. The melting and vaporization points for bulk copper at 1 atmosphere are 1358 Kelvin and 2836 Kelvin, suggesting that the free surface goes through melting and vaporization. Figure 3. 2(b) shows the depth of the melted (liquid) copper, i.e., the position of the melt front from the free surface, where the local temperature is equal to the melting point. The calculated maximum depth of the melt front is less than 2.5 μm from the free surface, in agreement with Bogaerts *et al.*[61]

Table.1 Material property used in the model verified with *Bogaerts, et al.*

Parameters	Values for Copper
Thermal conductivity (W/m/k)	380 (solid), 170 (liquid)
Specific heat (J/kg/K)	420 (solid), 494 (liquid)
Density(kg/m^3)	8960 (solid), 8000 (liquid)
Absorption coefficient(m^{-1})	7.44×10^7
Reflectivity	0.34
Melting point(K)	1358
Boiling point (K)	2836
Heat of fusion (J/mol)	1.3×10^4
Heat of vaporization (J/mol)	3.048×10^5

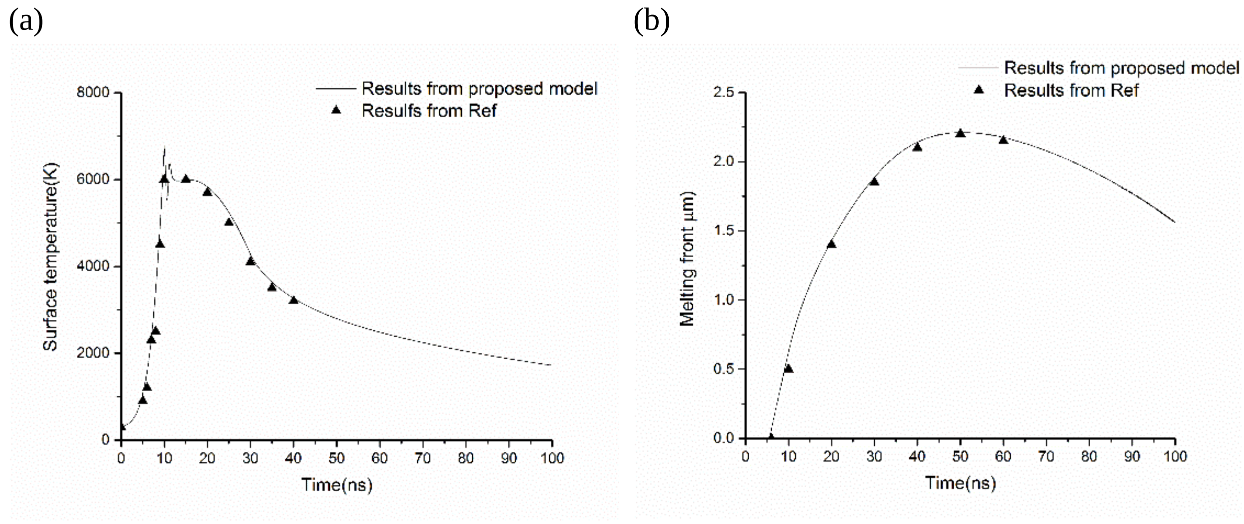

Figure 3. 2: (a) Time dependent surface temperature,

(b) Time dependent melt depth from the free surface of a copper half-space.

Furthermore, the numerical heat conduction model is validated against experimental results in the literature obtained by Zenou *et. al.* [58] in a 500 nm aluminum donor film on a soda-lime glass substrate. The followings are laser parameters wavelength = 532 nm, pulse duration = 400 ps, fluence = 0.76 J/cm^2, and diameter = 15 μm at the full at half maximum intensity level, and the material property parameters are listed in the Table. 2. The laser and material parameters are used as inputs to the numerical model. In the calculations, the phase distribution in the donor film and the size of the melt zone obtained when the melt front reaches the free surface, is compared to experimental observations by Zenou *et. al*. [58]. Figure 3. 3 shows the calculated time dependent absolute temperatures at the film-substrate interface and the film surface, and the melt front profile at different time points during the heating cycle of the donor film. The interface

Table.2 Aluminum material property used in the model verified with *Zenou, et al.*

Parameters	Values for Aluminum
Thermal conductivity (W/m/k)	205 (solid), 105 (liquid)
Specific heat (J/kg/K)	900 (solid), 1180 (liquid)
Density(kg/m^3)	2700 (solid), 2375 (liquid)
Absorption coefficient(m^{-1})	1.516×10^8
Reflectivity	0.91
Melting point(K)	933
Boiling point (K)	2792
Heat of fusion (J/mol)	1.079×10^4
Heat of vaporization (J/mol)	2.934×10^5

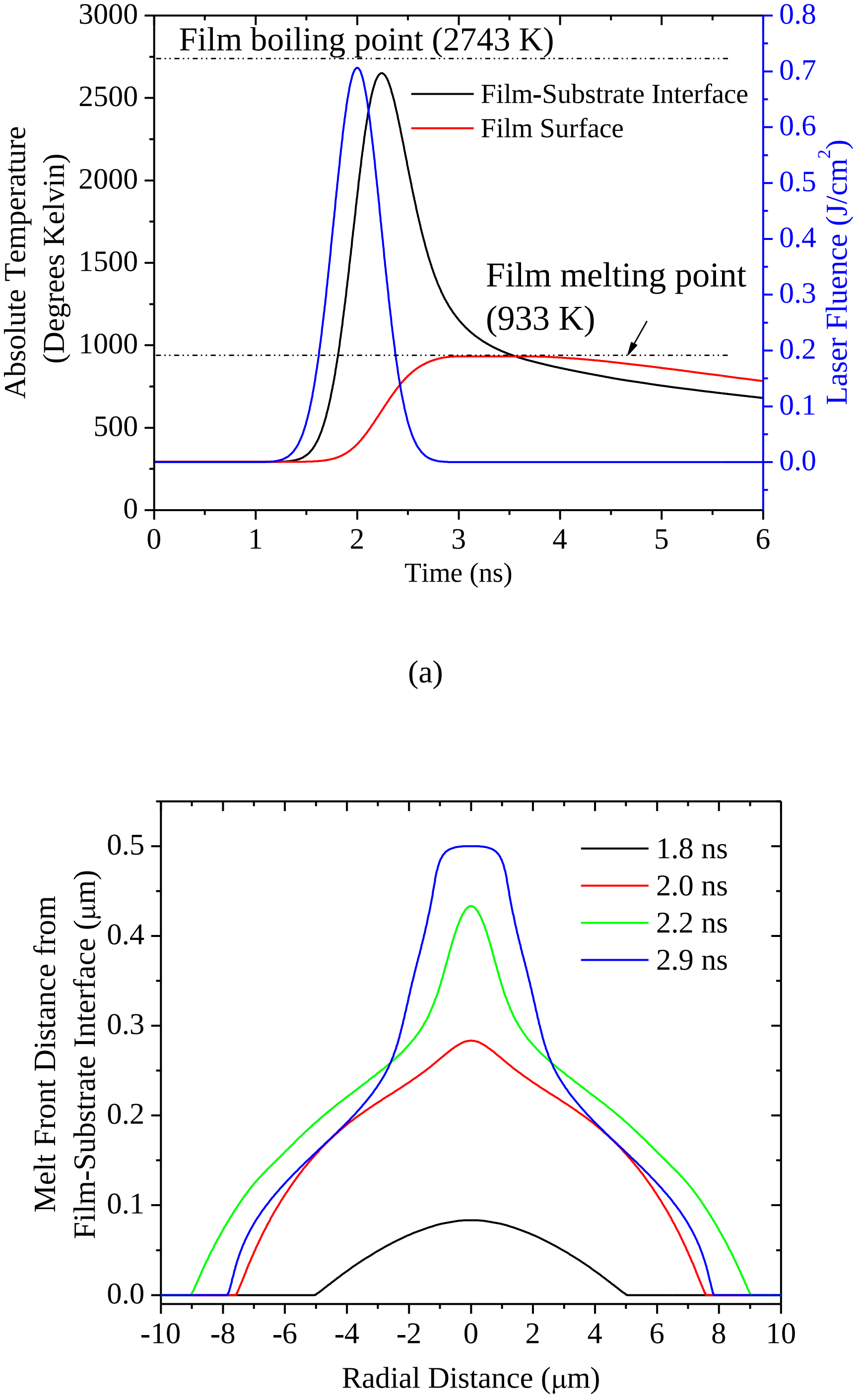

(a)

(b)

Figure 3. 3: Numerical calculation of (a) the absolute temperatures at the interface between an aluminum film and a soda-lime glass substrate, and the film surface; and (b) the melt front profile at different times after the interface is subjected to the input laser source.

temperature reaches the threshold for melting in the aluminum film at a laser fluence of 0.2 J/cm^2. The melting and boiling points of the aluminum film are 933 K and 2743 K respectively. The interface temperature increases with laser fluence, reaching a peak value of 2657 K at about 0.2 ns after the peak laser fluence of 0.76 J/cm^2 is attained. The temperature of the film at the free surface reaches the melting point after about 1 ns from the peak of the laser fluence, leading to complete melting of the film from the interface to the free surface. The absolute film temperature remains below the boiling point of the film. The melt front profiles are symmetric with respect to the center of the laser spot, and the melt front distance from the film/substrate interface is seen to increase with time as heat is dissipated radially into the donor film and from the interface towards the free surface. The melt front profiles become tapered near the free surface, as a result of heat buildup in the film. We remark that the surrounding medium is vacuum, as such, close to the free surface, there is an infinite thermal resistance for heat conduction away from the film, which leads to heat build-up near the surface. The melt front profile at 2.9 ns has a flat top with a width of 1.8 μm, which represents an aperture for molten metal to be ejected from. Free surface aperture diameters of close to 5 μm are observed experimentally by Zenou *et. al.* [58] being larger than the estimate from the thermal model. This discrepancy is expected since the thermal expansion of the molten metal and the non-melted film is expected to occur, which are not accounted for in the numerical model. The numerical calculations confirm the complete melting of the aluminum donor film for a threshold laser fluence of 0.76 J/cm^2 as suggested by Zenou *et. al*. [58] Furthermore, the tapered structure of the melt front close to the free surface predicted in the numerical calculations, may play a role in the nozzle geometry of the donor film obtained after the molten metal is ejected from the film aperture.

3.4 Results and Discussion

We examine the time dependent absolute temperature and melt front profiles in the copper thin films heated by the nanosecond pulsed laser. For the numerical calculations, the following laser parameters are used; laser wavelength = 1064 nm, pulse width t_0 = 15 ns, and spot radius r_0 = 15 µm. The laser pulse width and spot size are experimentally verified based on optical scattering intensity measurements of single laser shots using a 1 GHz photoreceiver, and knife edge measurements taken across the laser beam at the focal plane of the microscope objective. The copper material property parameters are listed in Table.1. Figure 3. 4 shows the calculated absolute temperature in the 800 nm and 1.5 µm thick copper film on the fused silica substrate after the film and substrate interface is illuminated by the pulsed laser. To compare the numerical results quantitatively, the peak input laser fluence for each case is selected to match the film surface temperature to the melting temperature of copper, which is 1358 K. A peak input laser fluence of 2.1 J/cm^2 is used for the 800 nm film and 12.3 J/cm^2 for

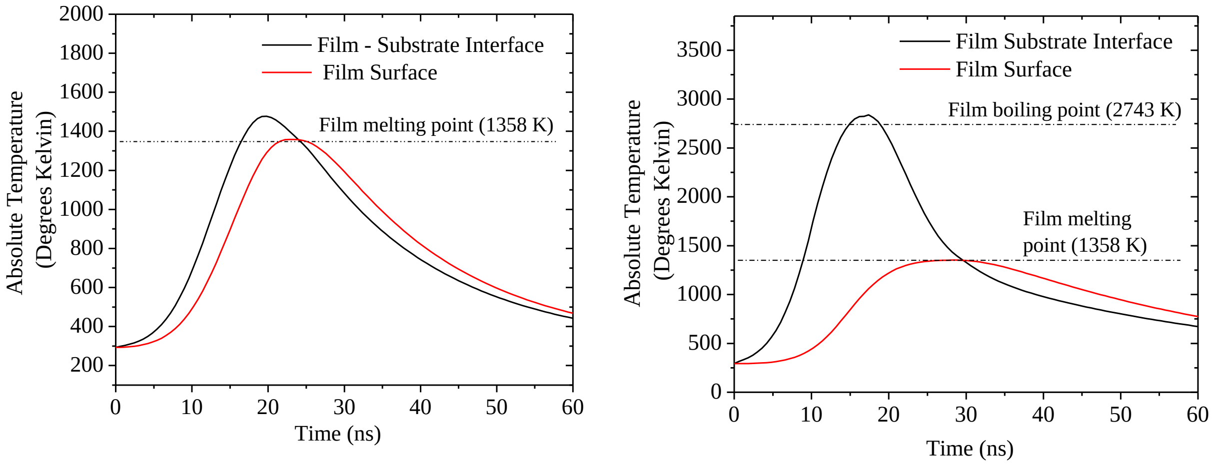

(a) (b)

Figure 3. 4: Numerical calculation of (a)&(b) the absolute temperature in the 800nm and 1.5µm thick copper films after irradiation of the film and substrate interface

the 1.5 μm film, which represent the thresholds for complete melting of the copper films. In the 800 nm film, the absolute temperature is reasonably uniform through the film thickness, and this occurs because the time scale for heat conduction from the film-substrate interface to the free surface, $\tau \propto h/\alpha$, where h is the film thickness and α is the thermal diffusivity, is much smaller than the duration of the laser pulse, allowing for a uniform temperature distribution to be achieved through the film thickness. Since a larger laser fluence (or laser intensity) is needed for the 1.5 μm film to reach the threshold for complete melting of the film, the absolute temperature obtained at the film-substrate interface is larger than the boiling point of the film, as such, the film is partially vaporized, forming a vapor cavity between the fused silica substrate and the melted film. Figure 3. 5 shows three snapshots of material phase distribution for the 1.5 μm thick copper film for different times up the initiation of vaporization at the film-substrate interface. Between 12 ns and 18 ns after the laser source is turned on, the diameter of the melt zone increases from about 6 μm to 14 μm, purely based on film melting, and the maximum melt depth from the interface attained within this time window is close to 0.7 μm. The vapor pocket initiated close to the film-substrate interface grows with time until the peak interface temperature is reached. It is expected that since the peak interface temperature is larger than the melting point of fused silica, the substrate will be partially melted.

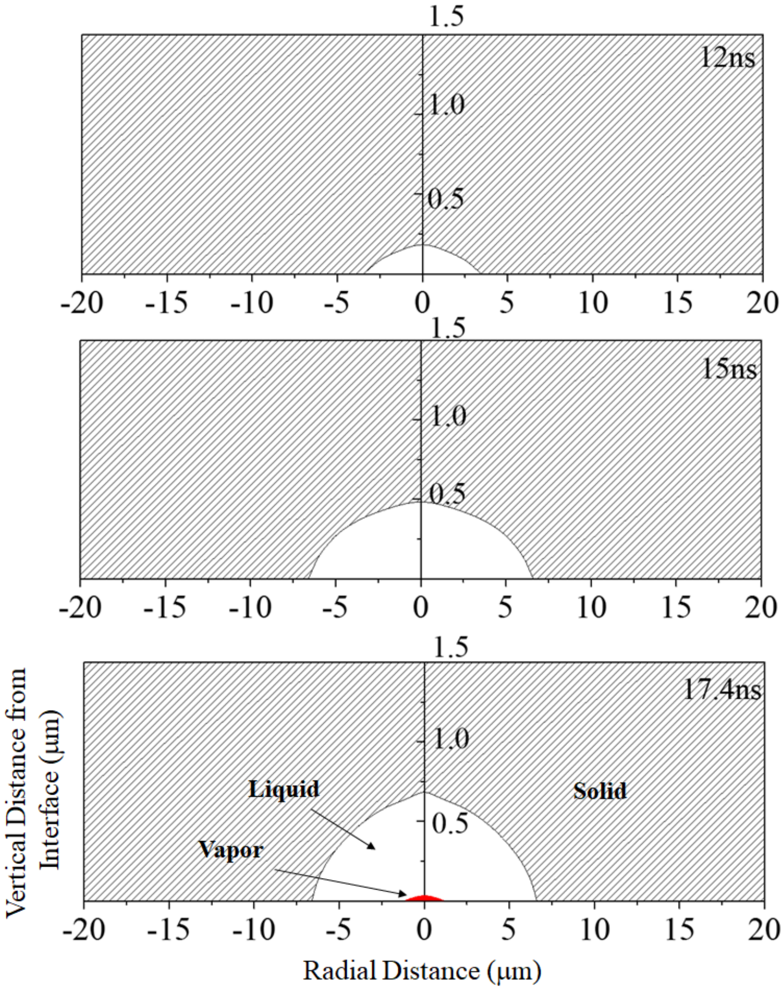

Figure 3. 5: Three snapshots of the material phase distribution in the film

We examine the parameter space of laser fluence and film thickness to identify the regimes in the LIFT process in which the copper donor film can be completely melted by the nanosecond laser, with and without film vaporization. For the numerical calculations, combinations of laser fluence and film thicknesses are chosen, the temperature distribution in the donor film is calculated as a function of time, and the material phase distribution within the film is monitored. In Regime 1, the donor film is partially melted by the input laser energy. This is most likely the regime in which micro-bumps are formed due to the difference in density between the molten and solid regions of copper film. Above the melting point of copper, the density of the molten metal decreases with temperature[Error! Reference source not found.], and the resulting volumetric expansion of the molten copper is constrained by the carrier substrate and the un-melted film. Results in the literature suggest that micro-bumps are generated as a means of relieving the compressive stress in the molten copper, and as such, the bumps tend to have a hollow interior. In Regime 3, the melt front reaches the free surface while the film-substrate interface temperature remains below the boiling point of the copper film. The threshold laser fluence required in this regime increases with film thickness. Regimes 2 and 4 cover the range of fluences at the donor film is partially vaporized. Consequently, the hydrostatic pressure from the confined vapor can lead to the generation of a compressional wave pulse that propagates through the film and substrate, transfer of molten metal to the target substrate by the large pressure of vaporized film, fracture of the un-melted film due to excessive expansion and large edge tensile forces, and other undesirable features.

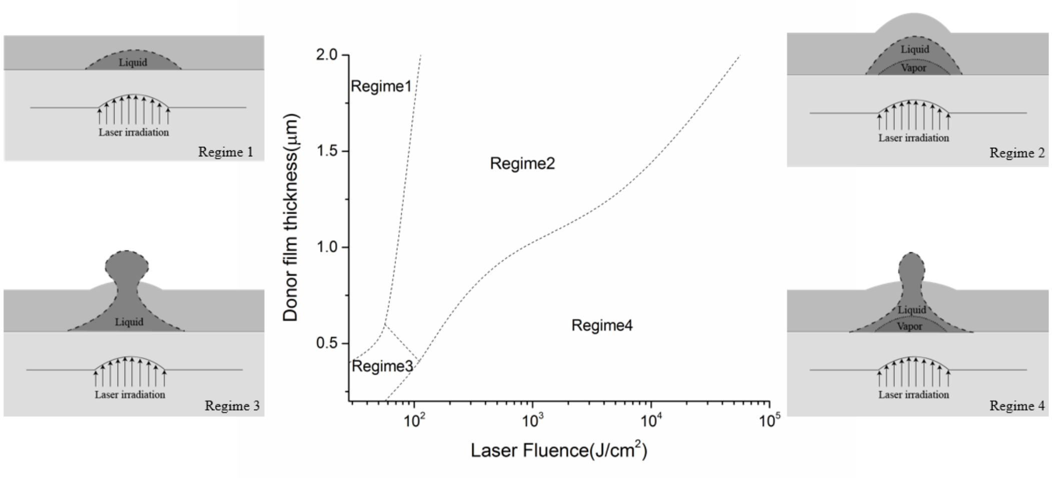

Figure 3. 6: Simulated threshold fluence for different regimes of the LIFT technique in a copper donor film of different thicknesses on a glass substrate. Illustrations are added to graph clarity.

For the numerical simulation on the pattered films, it is desirable to limit the melt zone to the region from the donor film-substrate interface to the bottom of the aperture in the donor film. This allows for retaining the function of the aperture, which is to funnel molten metal to the free surface. Figure 3. 7 shows a numerical calculation of the absolute temperature at a distance of 1 μm from the film-substrate interface in the 1.5 μm thick donor film. A peak laser fluence of 8.6 J/cm^2 is used in this case, and the peak temperature in the film remains below the vaporization threshold for the copper film. In the case of the 800 nm donor film, a laser fluence of 1.7 J/cm^2 is selected, for the peak temperature to match the melting point at a distance of 400 nm from the film substrate interface. Also, the temperature distribution in the melted region of the film, which is mostly uniform, is lower than the boiling point of the copper film. These values of laser fluence and the geometry of the donor film are used for our further experimental exploration.

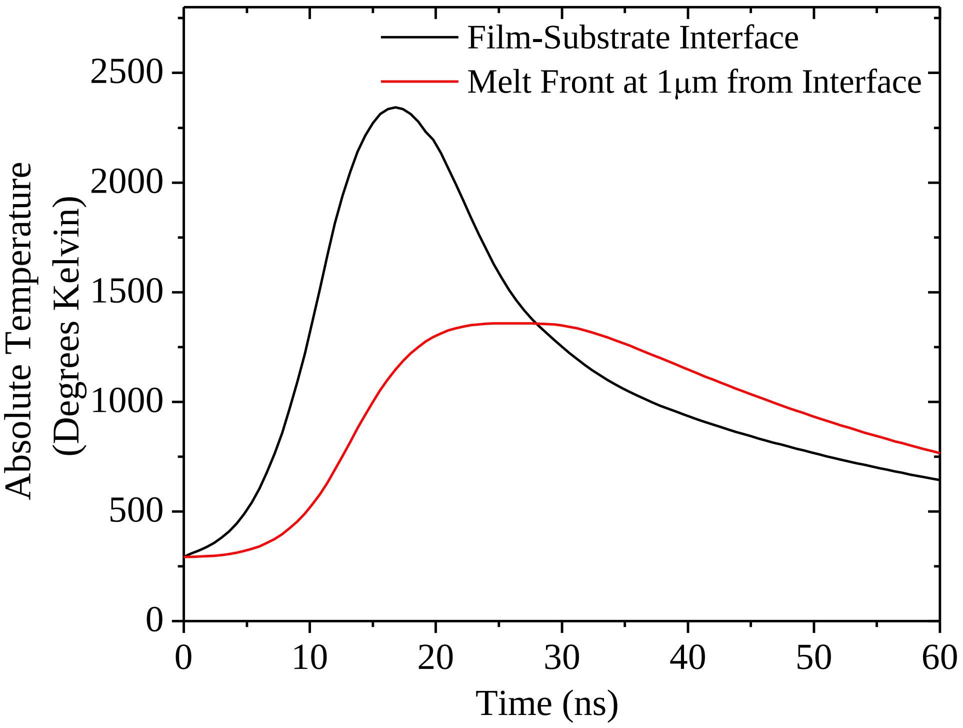

Figure 3. 7: Numerical calculation of the absolute temperature at a distance of 1μm from the film-substrate interface.

Chapter 4

Numerical Modeling of Jetting Hydrodynamics in the Laser Induced Forward Transfer

4.1 Introduction

In this chapter, a numerical model is presented that can predict the hydrodynamic flow of molten metal in the donor film, formation of liquid jets through an aperture, and the pinch-off of droplets at the tip of the jet. The model compliments the numerical heat conduction model presented in Chapter 3 to calculate the thermal history of a donor film after it is subjected to a nanosecond pulsed laser illumination. The numerical results of the droplet ejection dynamics presented in this chapter provides a fundamental understanding of the role of an aperture in the donor film on the jetting hydrodynamics. Liquid droplet ejection processes have been a subject of intense research interest over the past two decades, owing to the complex nature of the flow physics involved. Recently, advancement in optical imaging techniques have made it possible to time-lapsed images of the liquid jet formation, and droplet ejection dynamics, which in turn have enabled the development of better predictive models of the ejection processes. In spite of these advancements, precise control of the volume, velocity, and trajectory of ejected droplets in LIFT processes remain a formidable challenge. Numerical modeling tool continue to be of great importance to understand the process parameters that control these quantities and the quality of the transferred droplets to a target substrate. Bennett *et al.* [62] is one of the first researchers, who proposed a comprehensive description of the laser material interaction combining the transient heat transfer with phase change and the hydrodynamic development of surface. The model provides sufficient insight into the thermal condition and the evolution of the surface droplets. The model shows that the inertial force of the molten material is due to the acceleration of the interface between the solid and liquid phase, and the hydrodynamic phenomena results from the balance of inertial force and the surface tension restraining force. However, the model is simplified based on one-dimensional assumptions, which is not representative of the practical LIFT process.

Seifert *et al.* [63,65] investigated the thermal and hydrodynamic behavior of a gold surface under pulse laser irradiation based on a two-dimensional (2D) model coupling thermal and hydrodynamic behaviors. By solving Navier-Stokes equations under the influence of surface tension allowed for the prediction of droplets formation and desorption processes. In particular, their work demonstrated the growth and ejection of molten droplets from the melted film are strongly impeded by large values of surface tension. Recently, Brown *et al.* [66], explored the finite element method to study the dynamics of blister formation in the blister actuated LIFT method, under condition of finite deformation. Furthermore, the model was coupled with a computational fluid dynamics model, where the fluid layer is forced by the solid boundary deformation. The model was validated against the experimental results from time resolved deformation measurements, where the blistering dynamics, blister shape and temporal evolution of the liquid ink jets are predicted. The model enabled parametric studies of the effect of the ink density, surface tension, viscosity and film thickness as well as the blister size on the droplet jetting dynamics. Kattamis *et al.* [67] used a combination of the finite volume and volume-of-fluid methods to investigate the ejection of liquid donor films by rapid thermal expansion of the boundary of micron-sized blisters in a polymeric DRL layer. The blister-actuated LIFT provides a simpler framework to investigate the dynamics of the fluid droplet jet formation, pinch-off, and subsequent transfer to the target substrate, while confining the laser-material interaction and associated heating processes to the low thermal conductivity DRL. However, it is important to remark that the blister-actuated LIFT is suitable for printing liquid donor inks, as such these models are not directly applicable to laser melted donor films.

The physics of liquid jet formation and breakup mode have also been studied by various workers over the last two decades. Homma *et al.* [68] presented numerical analysis of the formation and breakup mode of liquid jet. In their analysis, a liquid material is injected vertically into a secondary medium through a nozzle. Non-dimensional Navier-Stokes equations, combined with the conservation of mass, are solved to describe the unsteady motion of the injection material, which is an incompressible Newtonian fluid. A Front-Tracking method is adopted to track the motion profile of the liquid material. In their work, three breakup modes for the liquid jet were identified, (1) dripping, (2) jetting with uniform droplets ejected, and (3) jetting with the ejection of non-uniform droplets. Furthermore, three dimensionless numbers were found to characterize the jetting dynamics in these modes: the Reynolds number, which measures the ratio of inertial forces to viscous forces; the Weber number, which is the ratio between the inertial force and the surface tension force, and the Froude number, defined as the ratio of the flow inertia to the external field. The first two modes are illustrated in Figure 4. 1.

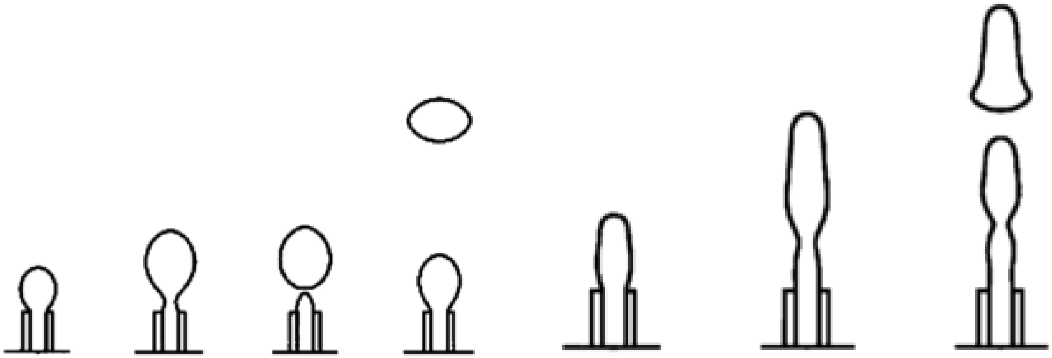

a). Dripping mode b). Jetting mode

Figure 4. 1: Schematic illustration of two modes [68]

In this chapter, a numerical scheme is presented that solves the Navier-Stokes equation for the case of a molten metal flowing through a hole in a rigid screen. The model is intended to provide representative results of the flow dynamics involved in the aperture based LIFT approach. Using velocity boundary condition derived from the thermal model described in Chapter 3, the numerical model predicts the hydrodynamic behavior of the molten metal under the influence of the aperture. The model accounts of the influence of surface tension, gravitational force, and inertia in the calculations simulation. The model predicts the occurrence of the dripping and jetting modes, depending on the Reynolds and Weber numbers involved. In particular, for low Reynolds number flows, droplets are formed at the aperture, and no jet is generated throughout the process. This breakup mode is called dripping mode. As the Reynold number increases, a liquid jet appears after a critical flow velocity. When the jet reaches a maximum length, droplets break off from the top of the jet. Details of the numerical model and numerical calculations of these cases are presented.

This chapter is framed as follows: First, details of the model description are explained in Section 4.2, as well as the numerical method. Next, in Section 4.3, the simulation results are validated by comparison with experimental reports in the literature. Furthermore, a parametric study of the influence of the material property (fluid viscosity), aperture geometry, and the laser fluence on jetting mode are discussed in Section 4.4.

4.2 Numerical Model

After absorbing laser energy, the metal material experiences a phase change from solid to liquid. The molten liquid flows throughout the aperture. In this simulation model, both the local molten metal and air phase are assumed to be incompressible, Newtonian fluid of density, ρ_j and viscosity, μ_j, the location of the interface separating the two different fluids are tracked by front tracking method. The other assumption is that the capping layer is regarded as a rigid body, that means the deformation of the capping layer is neglected. Beyond critical laser fluence, metal material is melted and injected into the aperture. The injection velocity in the aperture is assumed to be ideally vertical and uniform across the bottom surface, as shown in Figure 4. 2. The estimation of the injection velocity due to phase change can be given as,

$$v_a = \frac{dV_m}{dt}\left(\frac{\rho_s}{\rho_l} - 1\right)\frac{1}{A_a} \tag{4.1}$$

V_m is the volume of melting material, $A_a$is the aperture area, ρ_s and ρ_l are densities for solid and liquid material.

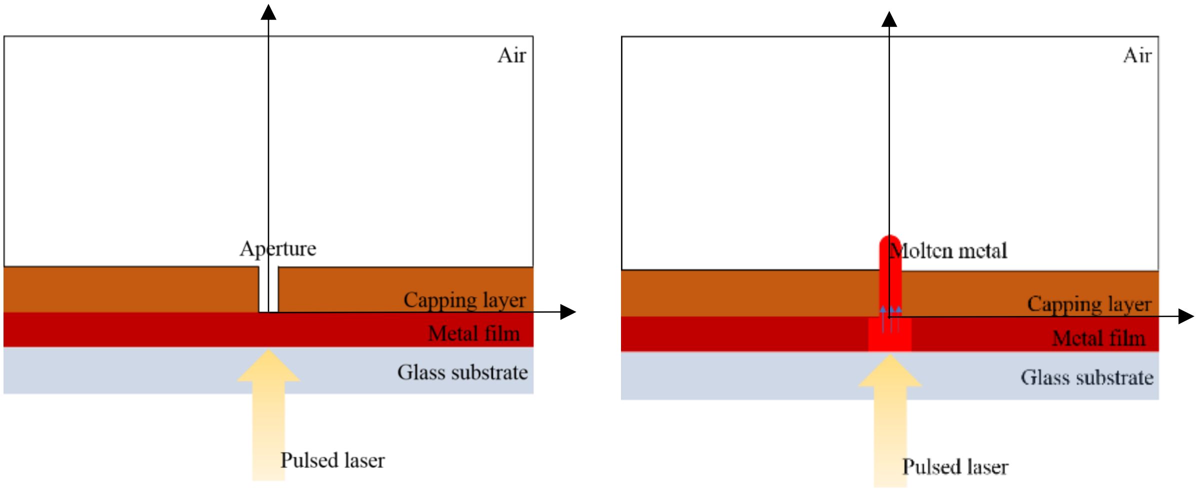

Figure 4. 2: The geometry of the hydrodynamic model

4.2.1 Governing equations

A single field form of the momentum equation, representing two incompressible fluids, is used in this model, the molten material and air are treated with different physical properties. The surface tension and gravity are considered. The unsteady momentum equation for variable density and viscosity is

$$\rho\frac{\partial \boldsymbol{u}}{\partial t}+\rho\nabla\cdot\boldsymbol{uu}=-\nabla p+\rho g+\nabla\cdot\mu(\nabla\boldsymbol{u}+\nabla^{T}\boldsymbol{u})+f \tag{4.2}$$

where, $\boldsymbol{u}$ is the velocity vector, p is the pressure, ρ is the density, μ is the viscosity, g is the gravity acceleration and f is the surface tension.

The conservation of the mass equation for incompressible flow is

$$\nabla\cdot\boldsymbol{u}=0 \tag{4.3}$$

4.2.2 Numerical Integration in the time domain

Chorin's project method is used to integrate the governing equation. The algorithm of projection method consists of two stages. In the first stage, an intermediate velocity $\boldsymbol{u}^{*}$ is calculated at each time step, which does not satisfy the incompressibility constraint. Eq. 4.2 is decomposed as follows, the pressure field is removed in the calculation of $\boldsymbol{u}^*$**,**

$$\frac{\boldsymbol{u}^* - \boldsymbol{u}^{\boldsymbol{n}}}{dt} = -\nabla \cdot \boldsymbol{u}^{\boldsymbol{n}}\boldsymbol{u}^{\boldsymbol{n}} + g + \nabla \cdot \mu(\nabla \boldsymbol{u}^{\boldsymbol{n}} + \nabla^T \boldsymbol{u}^{\boldsymbol{n}}) + \frac{f}{\rho} \tag{4.4}$$

where $\boldsymbol{u}^{\boldsymbol{n}}$is the velocity at *n*th time step. In the second stage, which is the projection step, the pressure field is used to project the intermediate velocity $\boldsymbol{u}^*$ onto a space of divergence-free velocity field to get the next update of velocity and pressure as follows,

$$\frac{\boldsymbol{u}^{\boldsymbol{n+1}} - \boldsymbol{u}^*}{dt} = -\frac{1}{\rho}\nabla p \tag{4.5}$$

Given the intermediate velocity from Eq. 4.5, there are still two unknowns to be solved: the pressure term on the right-hand side and $\boldsymbol{u}^{\boldsymbol{n+1}}$, the velocity at *n+1th* time step on the left-hand side. The solution is obtained by taking the divergence on both sides, and continuity equation requires , the velocity at *n+1th* time step to satisfy the incompressibility constraint, $\nabla \cdot \boldsymbol{u}^{\boldsymbol{n+1}} = 0$, thereby the pressure filed can be derived after the following Poisson equation based on the intermediate velocity,

$$\nabla^2 p^{n+1} = \frac{\rho}{\Delta t}\nabla \cdot \boldsymbol{u}^* \tag{4.6}$$

Once the pressure is found after the calculation of the intermediate velocity through Eq. 4.4, the velocity at next time step can be updated by Eq. 4.5.

4.2.3 Spatial discretization

An axisymmetric model is used to represent the problem. A Finite-Volume approach is used to discretize the governing equations. The incompressibility and momentum governing equations are applied to a small control volume, $\boldsymbol{V}$. In a control volume, the average velocity is defined as follows:

$$\mathbf{u} = \frac{1}{V}\int_{v} \boldsymbol{u}(x)dv \tag{4.7}$$

Moreover, the numerical approximations for other terms such as the advection term $\nabla \cdot \boldsymbol{u}^{\boldsymbol{n}}\boldsymbol{u}^{\boldsymbol{n}}$, $\nabla^2\boldsymbol{u}$ and the pressure term are averaged over a control volume, and furthermore, the volume integrals are developed as a surface integral based on the divergence theorem, the development is as follows for all the terms:

$$\frac{1}{V}\int_{V} \nabla \cdot \boldsymbol{u}\boldsymbol{u}dv = \frac{1}{V}\oint_{\boldsymbol{S}} \boldsymbol{u}(\boldsymbol{u}\cdot\boldsymbol{n})\, ds \tag{4.8}$$

$$\frac{\mu_o}{V}\int_{V} \nabla^2\boldsymbol{u}dv = \frac{\mu_o}{V}\int_{V} \nabla \cdot \nabla\boldsymbol{u}dv = \frac{\mu_o}{V}\oint_{S} \nabla\boldsymbol{u}\cdot\boldsymbol{n}ds \tag{4.9}$$

$$\nabla_h p = \frac{1}{V}\int \nabla p dv = \frac{1}{V}\oint_{S} p\boldsymbol{n}\, ds \tag{4.10}$$

The entire computational domain is divided into equal sized control volumes, as shown in Figure 4. 3. A staggered mesh domain is adopted to calculate the velocity and pressure. The pressure is assumed to be placed at the center of the control volume. The velocity is decomposed into two components, the radial velocity component and vertical velocity component. The radial velocity components are stored at the middle of the left and right edges of the control volume, and the vertical velocity components are stored at the middle of the top and bottom of edges. The positions of the pressure and velocity component in one single computational domain are shown in Figure 4. 4. The staggered mesh domain makes the calculation of the conservation of mass straightforward, integrating the mass equation over a control volume and converting the volume integral to a surface integral gives,

$$\int_V \nabla \cdot \boldsymbol{u} dv = \oint_S \boldsymbol{u} \cdot \boldsymbol{n} ds = 0 \tag{4.11}$$

This equation shows that the inflow in the control volume is equal to the outflow. The equation is expressed in the axisymmetric domain as follows,

$$\frac{u_{i,j}}{dr} - \frac{r_{j-1} u_{i,j-1}}{r_j dr} + \frac{v_{i-1,j}}{dz} - \frac{v_{i,j}}{dz} = 0 \tag{4.12}$$

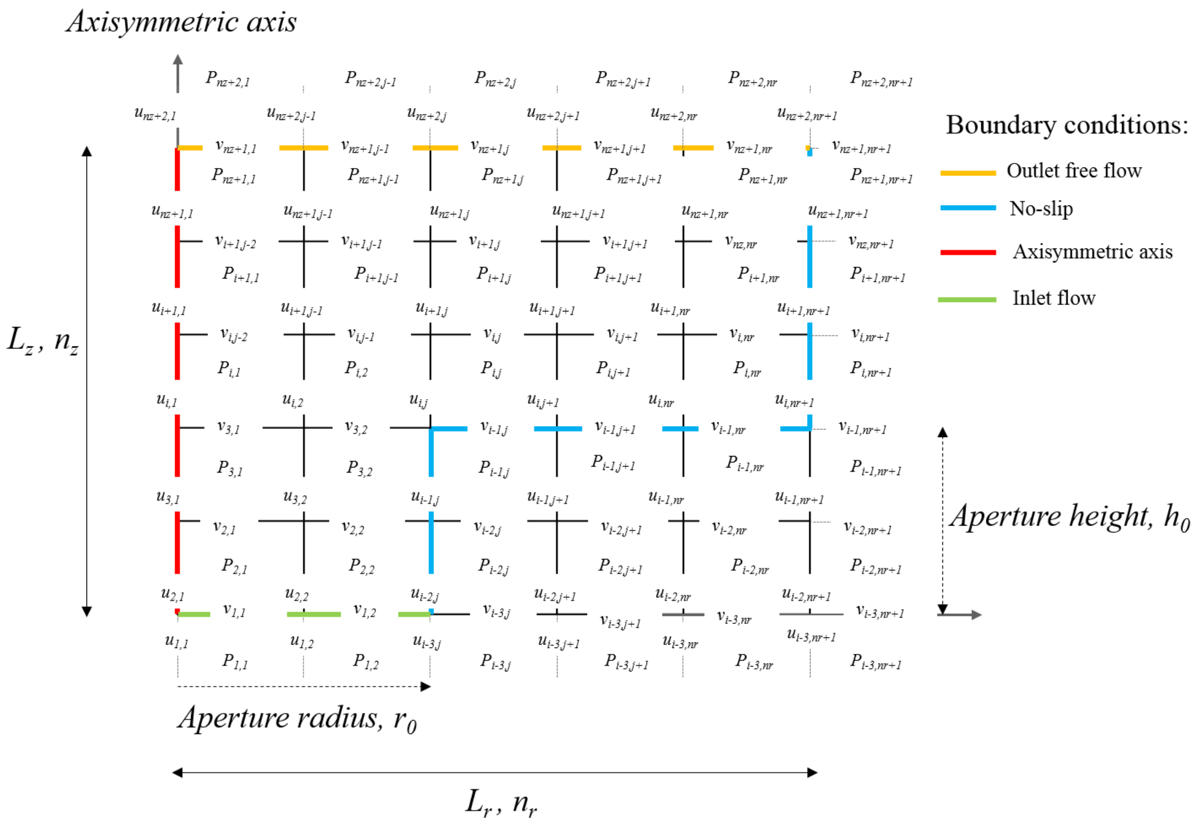

Figure 4. 3: Spatial dimerization of the computational domain

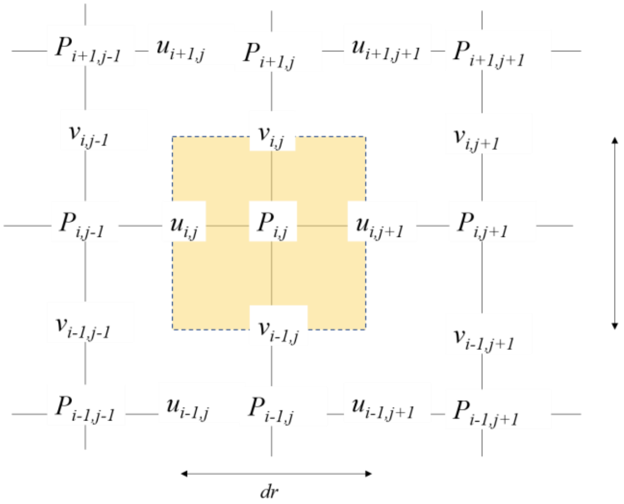

Figure 4. 4: The standard staggered mesh

4.2.4 Boundary conditions

a). Dirichlet boundary condition

The other advantage of using a staggered mesh is making boundary conditions particularly straightforward, especially for the Dirichlet boundary conditions, where the normal velocities are given directly. There are two scenarios for the application of the boundary conditions. In the first scenario, either the top/bottom or left/right edges of the control volume coincides with the boundary, we can simply set the velocity equal to what it should be on the radial or the vertical direction. For a rigid wall, Figure 4. 4(a) and (b), the normal velocity is zero, and for inflow boundary condition, at the bottom surface of the aperture, the normal velocity is generally given. In the second scenario, tangential velocity needs to be specified. It is not that straightforward because the velocity is not directly clarified on the boundary. However, we have the velocity at half a grid spacing inside the flow, together with the given tangential value on the boundary, we can specify the "ghost" value at the center of the ghost cell outside the boundary. The wall tangential velocity is given by a linear interpolation between the ghost velocity and the velocity inside the domain

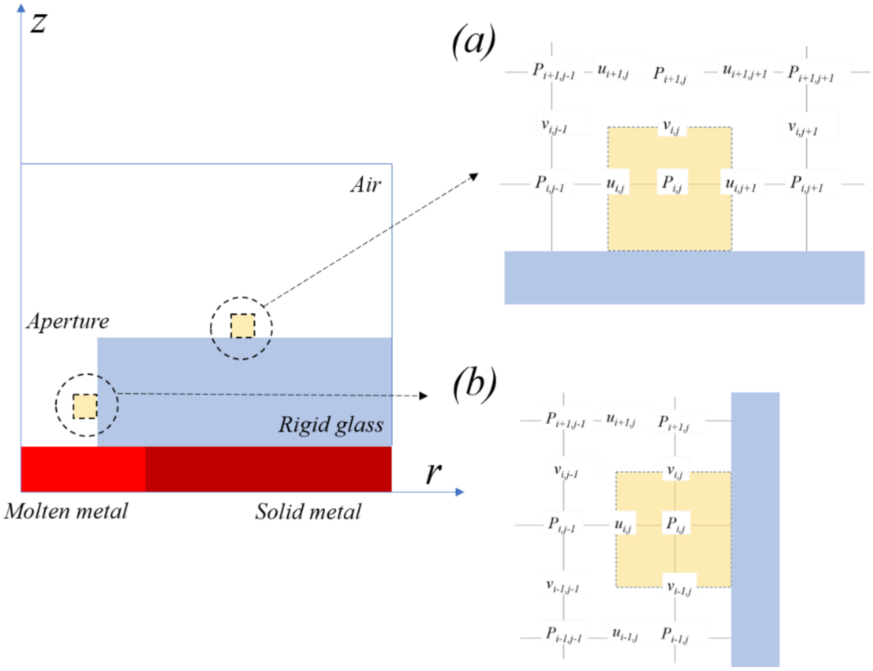

Figure 4. 5:. A control volume, (a) where the normal velocity is restricted on the bottom side, (b) where the normal velocity is restricted on the left side

b). Neumann boundary condition and axisymmetric condition

Free flow on the top boundary condition is simple, the flow flux across the top surface of the computational domain is zero, as follows,

$$\frac{\partial u}{\partial z} = \frac{\partial v}{\partial z} = 0 \tag{4.13}$$

At the axisymmetric axis, the restraint of the velocity component is as follows,

$$u_{i,0} = 0, \frac{du}{dr}|_{r=0} = 0 \tag{4.14}$$

4.2.5 Front tracking method

The interface is the internal boundary to distinguish the molten metal and air phase. The interface can be tracked between the different fluids and reconstruct the density from its location at each time step. This method is called front tracking method. For each time step, we interpolate the velocity component on the front based on the calculated velocity components on fixed grids, then the front can be moved based on the front velocity radially and vertically, as described in the following equation.

$$r_f^{n+1} = r_f^n + \Delta t u_f^n$$

$$z_f^{n+1} = z_f^n + \Delta t v_f^n \qquad (4.15)$$

4.2.6 Surface tension

Surface tension is significantly important in the simulations of two immiscible flows. In the case of molten metal interacting with air phase, the surface tension results from the greater attraction force of metal molecules to each other than to the molecules in the air. Surface tension exists only at the interface and the force per unit area is calculated as follows,

$$f_{surface} = \sigma k \boldsymbol{n} \qquad (4.16)$$

Where σ is the surface tension coefficient and k is the curvature, $\boldsymbol{n}$ is the normal direction along the interface. The unit normal is calculated as follows,

$$k\boldsymbol{n} = \frac{\partial \boldsymbol{t}}{\partial s} \qquad (4.17)$$

where $\boldsymbol{t}$ is the tangent to the interface, s is an interface segment. So the total force on an interface segment is calculated,

$$\delta f_{surface}^{l} = \sigma \int_{\Delta s_l} \frac{\partial \boldsymbol{t}}{\partial s} ds = \sigma(\boldsymbol{t}_{l+1/2} - \boldsymbol{t}_{l-1/2}) \tag{4.18}$$

Once the force at each interface point has been found, it can be interpolated onto the grid points. In that way, the surface tension is incorporated in the Navier-Stokes equations. Since the surface tension only exists at the interface, it can be regarded as a singular force expressed as a delta function,

$$\sigma k \boldsymbol{n} \delta(n) \tag{4.19}$$

Where, δ is a delta function of the normal coordinates n.

4.3 Model Validation

The numerical method is validated against reported experimental and numerical calculations in the literature. Details of the calculations are presented below.

4.3.1 Dripping mode

In this case [68], kerosene (ρ_k=890kg/m^3, μ_k=2.3mPa s) is injected into water (ρ_w=992kg/m^3, μ_w=1.04mPa s), the injection organic material is lighter than the continuous phase of a water solution. Figure 4. 9 shows the unsteady formation of kerosene droplet in water for the dripping mode. These are experimental pictures taken by a high-speed camera of 400frames/s with 480*128 pixel resolution. A domed interface appears at the early stage (t=1.00s), and then a neck is formed at t=1.60s. A cusp is observed behind the primary droplet just after its break off. The cusp moves back toward the nozzle due to the strong interfacial tension at the tip of the cusp. The droplets rise due to buoyancy and inertial forces. As shown in, the size of the primary is in good agreement with the observed sizes in the experiments. The surface tension is σ=36.5mN/m, injection velocity is 0.6cm/s and the nozzle radius is 4.7mm.

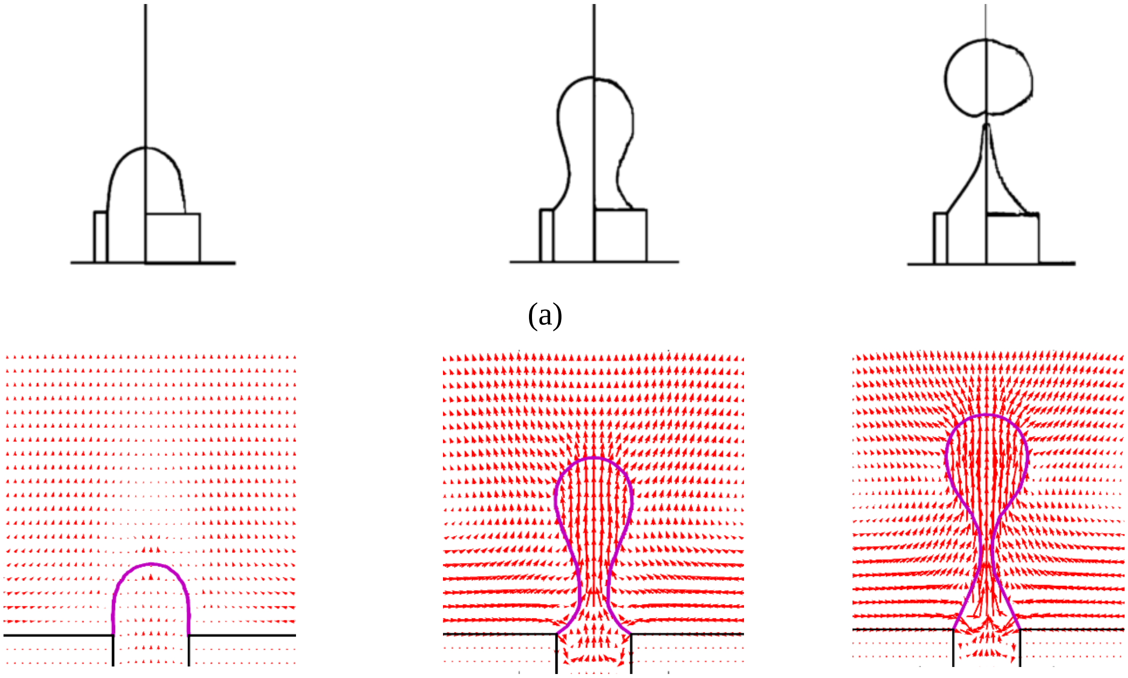

(a)

t=1.00s t=1.60s t=1.68s

(b)

Figure 4. 6: Experimental (a) and simulated (b) results for dripping mode

4.4 Results and Discussion

The characteristic of the dripping mode is described in validation section, there is the other important mode explained in this section. A copper film with a thickness of 60nm is irradiated with nanosecond pulsed laser is melted into liquid phase (ρ_{Cu}=8020kg/m^3, μ_{Cu}=3mPa s). The liquid phase copper material is ejected into the air phase (ρ_{air}=1.16kg/m^3, μ_{air}=18.45μPa s) through a 1 μm diameter nozzle. The surface tension of the molten copper is 1257 mPa s. It is apparent that a straight jet is generated from the nozzle and the length is dependent on the laser fluence. The part of the jet starts to narrow down at 1.5 μs. A droplet is formed at the top of the jet and a necking occurs at the connection between the jet and the droplet. When the necking decreases to a critical diameter, the droplet can be ejected from the jet. As shown in Figure 4. 7.

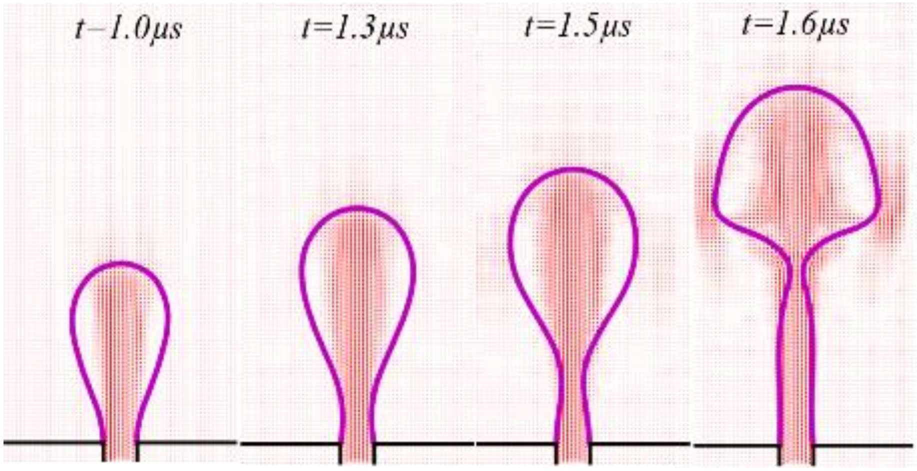

Figure 4. 7: A jetting mode, molten copper injected into air phase at velocity of 15cm/s, and the nozzle size is 1µm.

Dripping mode and jetting mode are the two major modes for the material injection problem. They have entirely different characteristics as mentioned. The dripping mode has a primary droplet ejected from a cusp, and the jetting mode has a high aspect ratio jet behind the ejections. In order to understand the ejection mechanism, it is important to identify the specific mode based on the different parameters.

In this simulation model, copper film is considered as a molten metal material, which is injected into the aperture. The density and viscosity of molten copper is 8020kg/m^3, 3mPa s, and for the air phase, the density is 1.16kg/m^3, and the viscosity is 18.45µPa s. It is assumed that the molten material is injected vertically into the aperture so that the height of the aperture is not able to affect the flow motion of the material. Two parameters are considered in this analysis, injection velocity through the aperture and aperture size. The mode identification is shown in Fig. 34. When the aperture radius is larger than 1.0m/s or the injection velocity is larger than 16m/s, the molten copper is always in jetting mode. Previous thermal calculation estimates a minimum melting front propagation speed is 150m/s, so the minimum injection velocity from Figure 4. 8 is about 15 m/s. It proves that for the copper film, it is always the jetting mode occurring in the patterned LIFT.

Three dimensionless numbers are always used to characterize the fluid dynamics, which are the Reynolds number (Re), Weber number (We) and Froude number (Fe). They measure the ratio of inertial forces to viscous forces, inertial force to the surface tension force and the flow inertia to the external field, separately, as calculated in Eq. 4.19. In patterned LIFT, the only external body force is the gravity, the inertia of molten copper is much larger than the gravity force, so the consideration of Froude number effect is neglected in this analysis. The results are shown in Figure 4. 9.

$$
\begin{aligned}
Re &= \frac{2Ru\rho_{copper}}{\mu_{copper}} \\
We &= \frac{2Ru^2\rho_{copper}}{\sigma} \qquad (4.20) \\
Fr &= \frac{u^2\rho_{copper}}{2Rg(\rho_{copper} - \rho_{air})}
\end{aligned}
$$

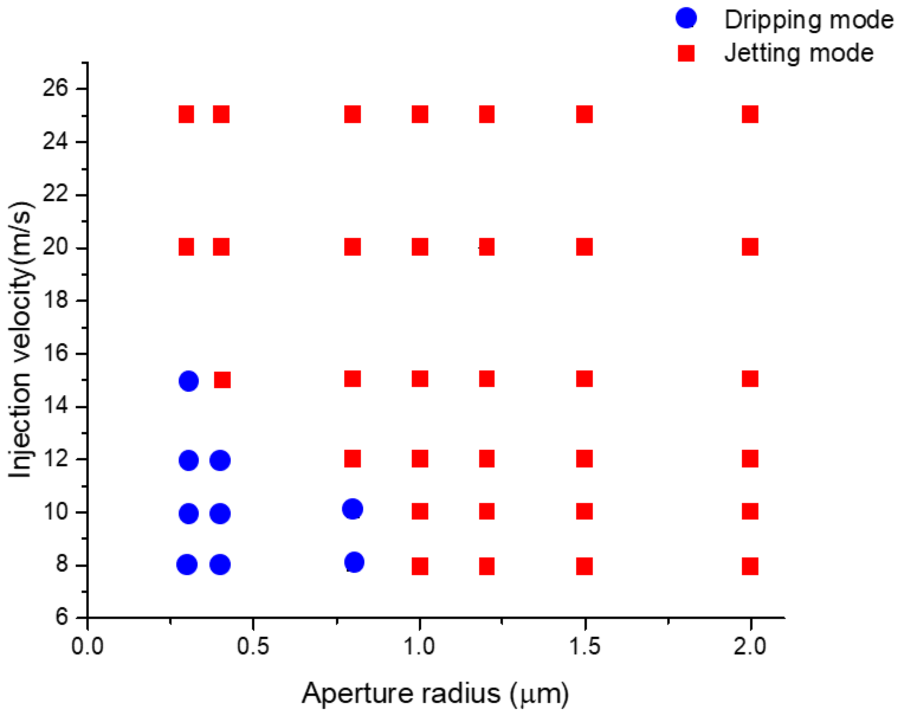

Figure 4. 8: Parametric study on injection velocity and aperture radius

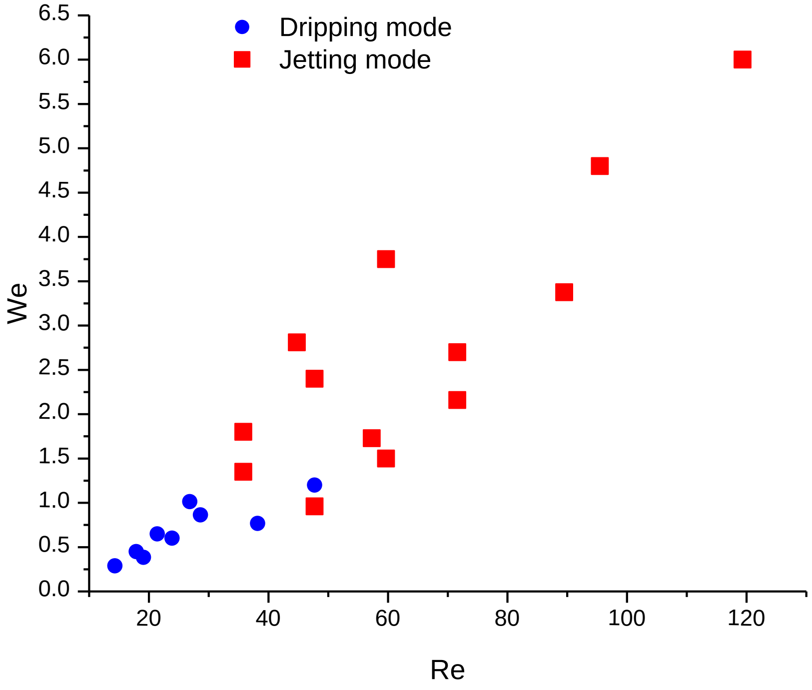

Figure 4. 9: Parametric study on Reynolds number and Weber number

When We is larger than 1.0 or Re is larger than 40, the molten copper is always in jetting mode. That means, the jetting mode can be guaranteed, provided that the surface tension is not smaller than the inertia or inertia has to be more than 40 times as large as the viscous force. This result confirms that inertia and surface tension are two major factors influencing the hydrodynamics of the molten copper.

Droplet size after droplet pinch-off is measured for 1.0μm, 1.2μm and 1.5μm apertures at the injection velocity ranging from 10m/s to 100m/s. For the velocity smaller than 40m/s, droplets are always expanding, lower velocity results in a bigger droplet. 6.0μm, 5.7μm and 5.0μm diameter droplet are ejected to the receiver when the molten copper flows into the aperture of 1.0μm, 1.2μm and 1.5μm at 10m/s. Starting the injection velocity larger than 40m/s, the droplet size is always equivalent to the aperture size. As a result, 40m/s is regarded as a threshold for molten copper on controlling droplet size. Spot size is still unpredictable when the velocity is smaller than 40m/s, however, spot size is equal to the aperture size as long as the velocity is larger than the threshold. This theoretical analysis proves one of the advantages of aperture based LIFT technique, that the aperture has the ability to control the ejected spot size if the injection velocity of the molten metal is large enough.

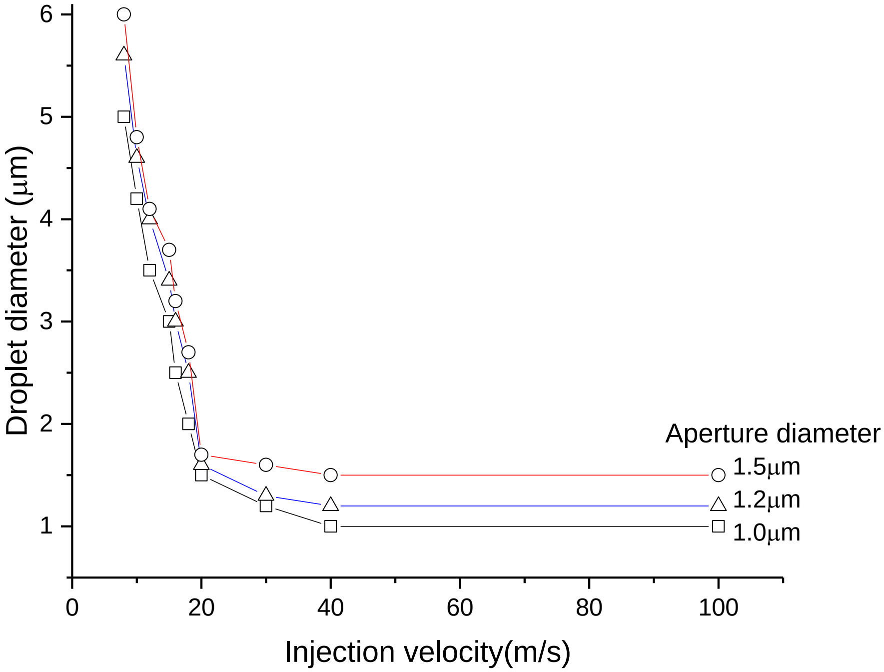

Figure 4. 10: Injection velocity dependent droplet diameter

for aperture size of 1.0 μm, 1.2 μm, 1.5 μm

Chapter 5

Pulsed Laser Transfer of Micro-Droplets through Patterned Thin Copper Films: An Experimental Study

5.1 Introduction

This chapter presents experimental measurements using the mask-based approach to control the transfer of molten droplets from a donor film to a target substrate by locally heating thin copper films with a Q-switched nanosecond pulsed laser. The presence of apertures in the donor film facilitate the generation of micro-bumps with small protrusions that extend into micro-jets with diameters of between 1-2 μm and a height of up 5 μm above the donor film surface. The micro-jets eventually break-up into single or multiple droplets that are deposited on the target substrate. It is observe that the number of transferred droplets for a single laser shot depends on the film thickness and the laser fluence. The smallest diameter of a single droplet observed on the target substrate is below 3 μm, obtained from an 800 nm thick donor film. Furthermore, the thermal and hydrodynamic models described in chapters 3 and 4 are used to provide a qualitative explanation for the micro-bumps and micro-jets observed in the experimental data, and to identify the regime where controlled melting of the donor film and transfer of molten droplets to the target substrate can be facilitated. The numerical results suggest that the aperture-based approach has the potential to control the minimum size of droplets transferred to the target substrate, thus allowing for controlled synthesis of micro- and nanosized metal particles, which have significant interests in sensing and catalysis applications, and microscale ballistic experiments.

Aperture controlled droplets are an integral aspect of the conventional LIFT process. For example, Zenou *et. al.* [58] showed that at moderately low input laser fluence, the donor film melts from the film-substrate interface to the free surface of the film without experiencing vaporization, and the intersection of the melt front and free surface creates an aperture through which droplets can be transferred to the target substrate. One advantage of aperture-based droplet ejection is the ability to transfer droplets with low angular divergence angle to a target substrate, and with a large offset distance (~ 1 mm) between the donor film and target. Consequently, the landing accuracy of the droplets on the target substrate can be well controlled. The aperture size obtained in conventional LIFT processes is limited by the heating dynamics of the donor film, and the input laser source parameters (spot size, fluence, and pulse duration). Alternatively, the droplet size can be controlled by the use of apertures in a mask layer covering the donor film. These apertures can be directly patterned on the donor film by standard lithographic processes, as demonstrated in this work, or fabricated in a capping layer with a higher melting point than the donor film.

An important component of this type of work is the availability of visualization tools that can provide access to time-resolved images of the droplet transfer dynamics. This chapter is formulated as follows: First, a general review of experimental methods for imaging droplet transfer in LIFT processes are discussed in section 5.2. In sections 5.3 and 5.4, details of the experimental setup and sample preparation methods used in this project are discussed. In Section 5.5, experimental results showing the morphology of the donor film and target substrate before and after the transfer of molten droplets are presented and the results are discussed.

5.2 Experimental Visualization of LIFT Process

In order to describe the details of the transfer characteristics during LIFT, time-resolved imaging techniques are widely used. High-speed camera is one of the two most popular methods. For example, in Riester *et al.*[69]'s experimental setup on investigation of the jetting behavior, a high-speed camera (Fastcam SA5, Photron) with up to 300,000 frames per second, equivalent to a time resolution of 3.3μs, is used for monitoring the emerging jet. The camera automatically starts to work by detecting any changes in the scene. The setup is shown in Figure 5. 1. A zoom objective is used to adjust the magnification that the field view in the vertical axis corresponds to the gap between the transfer and the target substrate. The gap distance in this setup is around 1mm. The authors recorded the jet formation for a laser fluence from 0.5J/cm^2 to 3J/cm^2, and studied the effect of concentration of liquid layer on the jetting behavior.

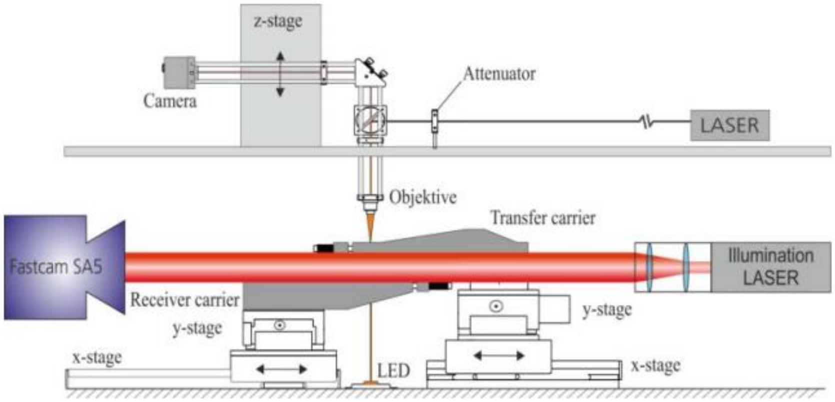

Figure 5. 1: Sketch of LIFT setup for high speed imaging [69].

The other popular method is pump probe imaging techniques. The common high- speed cameras often suffer from limited spatial resolution in favor of high frame-rates. Due to this disadvantage, common high-speed cameras are not feasible to capture the LIFT ejection dynamics, when the ejection velocities is over 2000 m/s at the required spatial resolution in the single micrometer range. Therefore, pump-probe or laser-induced shadowgraphic imaging techniques are typically employed in this case. Pump probe measurement can be used to obtain information on ultrafast phenomena. The general principle is the following, a sample is hit by some pump pulse, which generates some kind of excitation in the sample. After an adjustable time delay controlled with an optical delay line. A probe pulse hit the sample, and its transmission of reflection is measured. By monitoring the probe signal as a function of the time delay. It is possible to obtain information on the decay of the generated excitation, or on the other processes initiate d by the pump pulses. The probe signal is typically averaged over many pules. A fast photodetector it not required. The temporal resolution of a single measurement is determined by the pulse duration of the probe source, which is often provided by an additional laser source, often connected to an external fluorescence cell. Papazoglou *et al.* [70] investigated the dynamics of sub-picosecond LIFT of 200nm InOx films by means of time-resolved shadowgraphy. The setup is shown in Figure 5. 2. The LIFT process was investigated for time delays between 10 nanoseconds and 10 microseconds. The LIFT ejection was found to be highly directional, exhibiting an angular divergence of 3◦ while achieving velocities of 400 ± 10 m/s, depending on the laser fluence. Besides, the recorded images clearly show that the LIFT ejection is driven by a shockwave and most of the material is transferred in solid state, as shown in Figure 5. 3a. Feinaeugle *et al.* [71] investigated the transfer of solid phase material by femtosecond LIFT by means of the same technique with Papazoglou *et al*.[70]. For intact transfer of 1.1 µm thick Bi2Se3, the ejection velocity 48 m/s, and for intact transfer of 1.8 µm thick PZT, the velocity is 34 m/s. In another case of 0.5 µm thick Terfenol-D, the velocity is 140m/s. In contrast to prior observations, no shockwave was observed during the transfer. Due to the low ejection velocity and the absence of a shockwave, it is implied that femtosecond LIFT is suitable for intact transfer of solid materials.

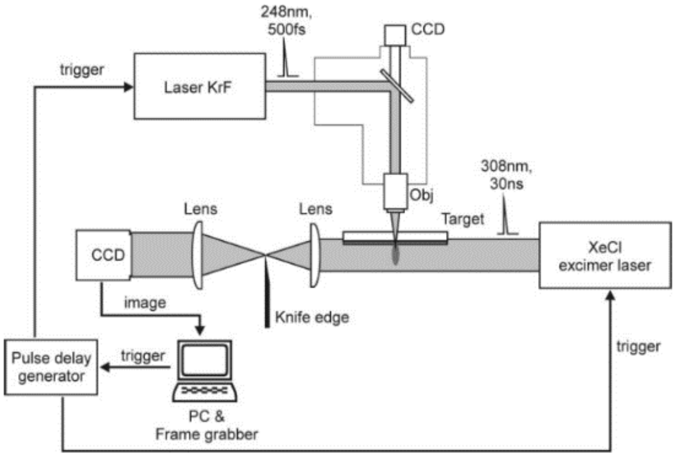

Figure 5. 2: Schematic diagram of the pump-probe imaging setup [70].

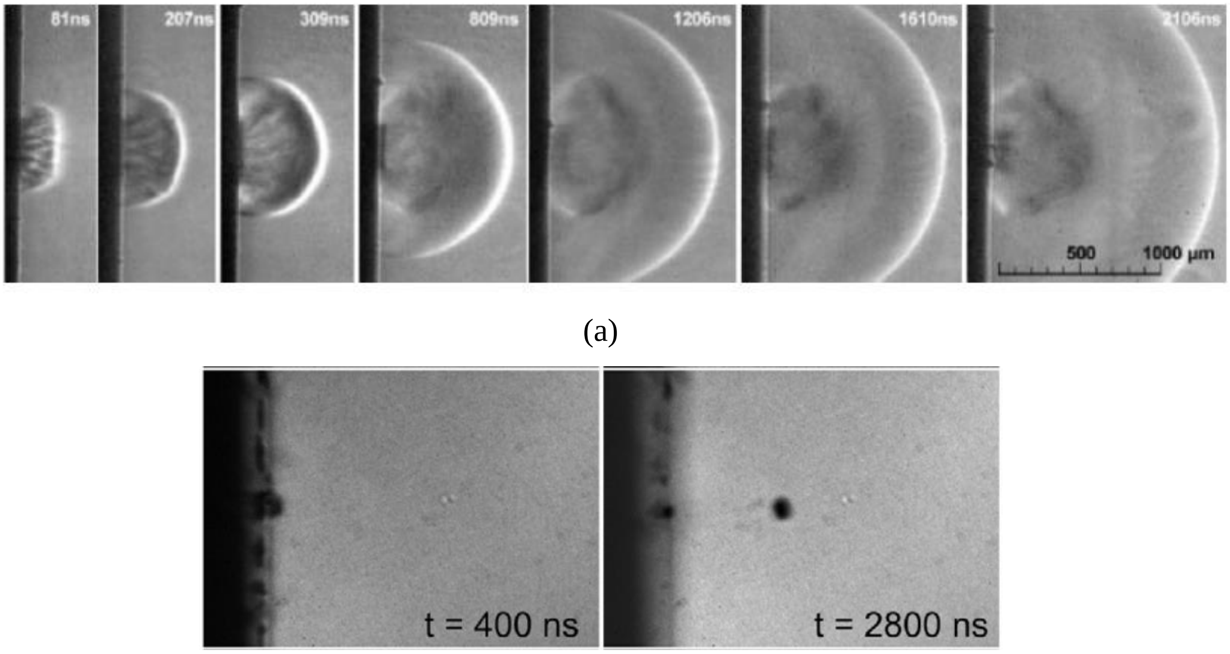

(a)

(b)

Figure 5. 3: (a) Shadowgraph images of the InOx film under backward laser irradiation of the InOx film at various delay times. The laser fluence was 430 mJ/cm^2. [70]

(b). Series of shadowgraph images of fs-LIFT of a Bi2Se3 flyer. Each frame was taken at a different camera delay time. The fluence used was 130 mJ/cm^2. [71]

Time resolved study of the LIFT process based on both high-speed camera and pump-probe measurement is popular for both liquid and solid phase LIFT, however M.Zenou *et al.* [72] proposed a new method to measure the droplet velocity. Moreover, it allows for measuring the incubation time, which is the sum of the droplet build-up time and the time it takes for the droplet to eject from the donor substrate, and the solidification time of droplet on the target substrate. The new method overcomes the limitation of conventional optical method, which is a requirement of a large donor-to-acceptor gaps. A schematic view of the setup for measuring the droplet velocities is shown in Figure 5. 4. Here, the method takes advantage of the metal droplets being electrically conducting. In the beginning. two parallel thin gold pads (100nm thick and prepared by standard evaporation followed by photolithography) are coated on a glass substrate, the two pads are separated from each other by a narrow gap of 0.5 μm, which is much smaller than the droplets diameter after landing (typically>3 μm). As the printed droplet is ejected, approaches the receiving surface and covers the gap between the gold pads, an electrical contact is formed, indicating the droplet arrival time. A programmable DC source-measure unit (Keithley model 2200-20-5) is connected to the probe along with a 300 X resistor in an arrangement that allows accurate measurement of the voltage time-trace. The laser pulse timing is monitored using a photo-diode (PD) that serves to determine the time delay between laser pulse arrival on the donor and the droplet landing time on the target substrate.

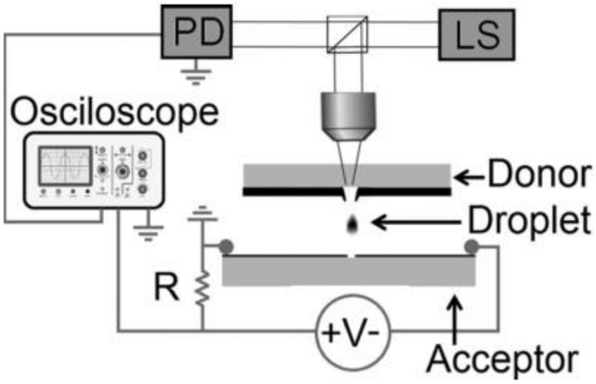

Figure 5. 4: Schematic diagram of the pump-probe imaging setup from M.Zenou *et al.* [72]

5.3 Experimental Setup

The schematic of the experimental setup is shown in Figure 5. 5**Error! Reference source not found.**. A neodymium doped yittrium-aluminum garnate (Nd:YAG) laser with wavelength of 1064 nm, pulse duration of 15 ns and pulse-to-pulse repetition rate of 20 Hz is used, as shown in Figure 5. 6. The laser is directed through a 5x long working distance microscope objective with a numerical aperture of 0.1, focusing the laser at the interface between the transparent carrier substrate and the copper donor film. The spot size of the laser source is 14 μm at the full-width-at-half maximum intensity level, obtained from knife-edge measurements of laser source profile at the focal plane of the microscope objective. The target substrate is a single crystal silicon substrate. The sample-target assembly is supported on a three-axis linear translation stage. A standard optical microscope connected to a charge coupled device (CCD) is incorporated into the experimental setup, for alignment of the focused laser source within the field-of-view of the microscope. A set of alignment marks, visible at the film/substrate interface are used to align the laser spot relative to the position of the dimple array, since the dimples are not visible within the field-of-view of the microscope. Each of the heated positions on the donor-carrier interface is subjected to a single laser pulse, and the resulting profiles of the donor film and the target substrate are inspected with the SEM.

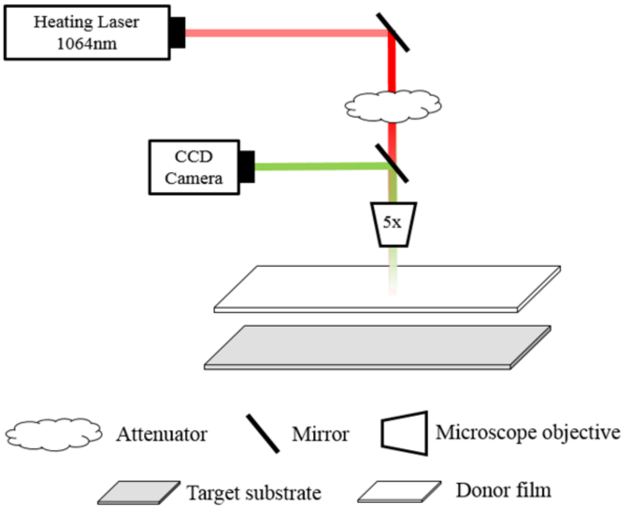

Figure 5. 5: Schematic diagram of the experimental setup

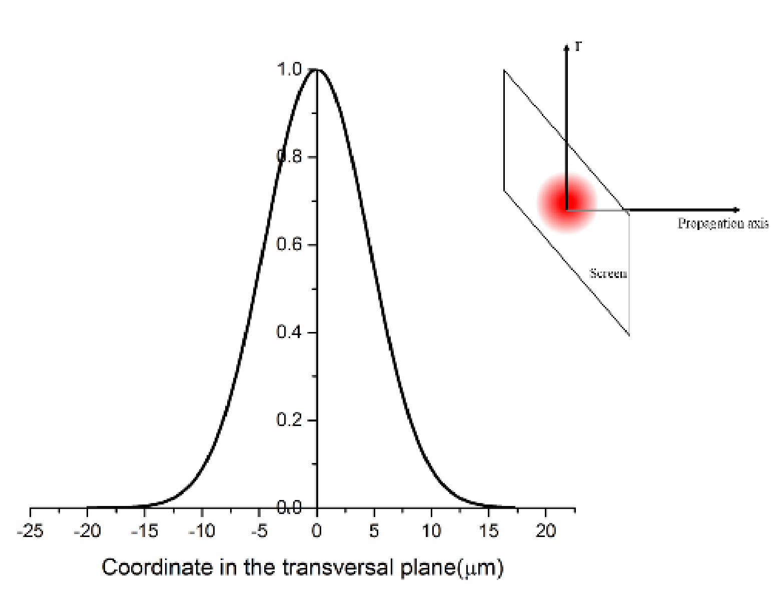

(a)

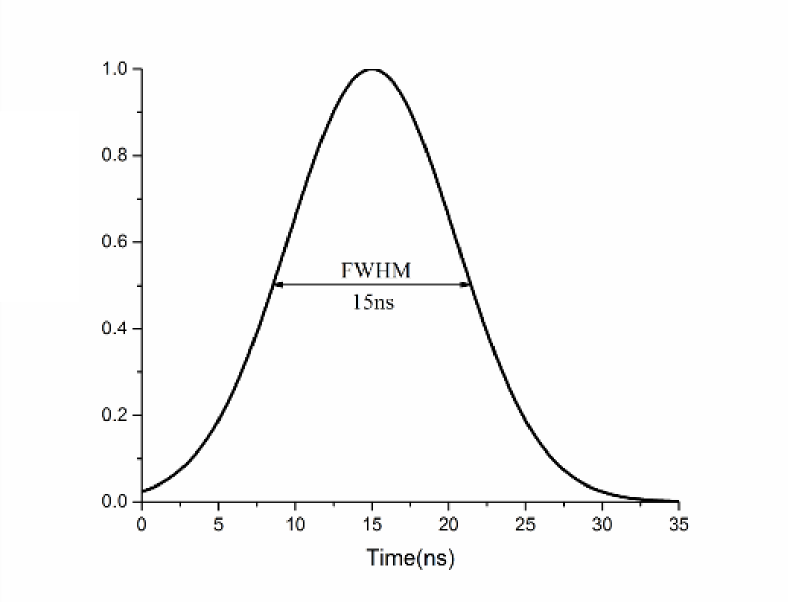

(b)

Figure 5. 6: (a) Spatial and (b) temporal distribution of laser intensity

5.4 Sample Fabrication

Samples comprised of thin copper donor films with thicknesses of 1.5 μm and 800 nm respectively on a 500 μm thick fused silica substrate are used. The metal films are deposited on the substrate by electron beam deposition. Fused silica is chosen as the substrate for two reasons. First, the softening and melting temperatures of fused silica, which are 1938 K and 1988 K are higher than the melting point of copper. Second, the coefficient of thermal expansion of fused silica is small, 5.5×10^{-7}/°C, which limits the deformation of the substrate during pulsed laser heating. Samples with templated circular apertures are fabricated using maskless photolithography. In the technique, a thin coating of positive photoresist (S1805) is deposited on the metalized fused silica plate, and the sample is spun at 3000 revolutions per minute for 30 seconds to produce a coating with uniform thickness. The photoresist coating is baked on a hot plate maintained at 110 ^{0}C for 70 seconds to remove the excess photoresist solvent. After baking, the photoresist layer is exposed to a focused ultraviolet light source with wavelength of 390 nm, and the laser spot is scanned in a two dimensional grid to selectively polymerize the photoresist. The photoresist layer is developed by dipping the sample in the AZ917 M1F solution for 15 seconds, followed by a dilute solution of ferric chloride ($FeCl_3$) that etches through the copper film, leading to an array of circular dimples in the film. The dimple depth is controlled by the residence time of the sample in the $FeCl_3$ solution. To achieve etch depths of 1 μm and 0.5 μm, the sample was dipped in the solution for 5 and 2 minutes respectively. In the final processing step, the developed photoresist left on the sample is lifted off, leaving the copper film with dimples. Figure 5. 6 shows a representative scanning electron microscopy (SEM) image of the 1.5 μm thick copper film with a 2D grid of dimples and a line profile of the height change across a single dimple obtained with a tapping mode atomic force microscopy (AFM) probe. The dimple depth is approximately 0.56 μm and the opening diameter is close to 3 μm. Since the dimple depth is smaller than the thickness of the donor film, an aperture is produced when the melt front in the film intersects the dimple. For the 800 nm donor film, the dimple depth is close to 400 nm.

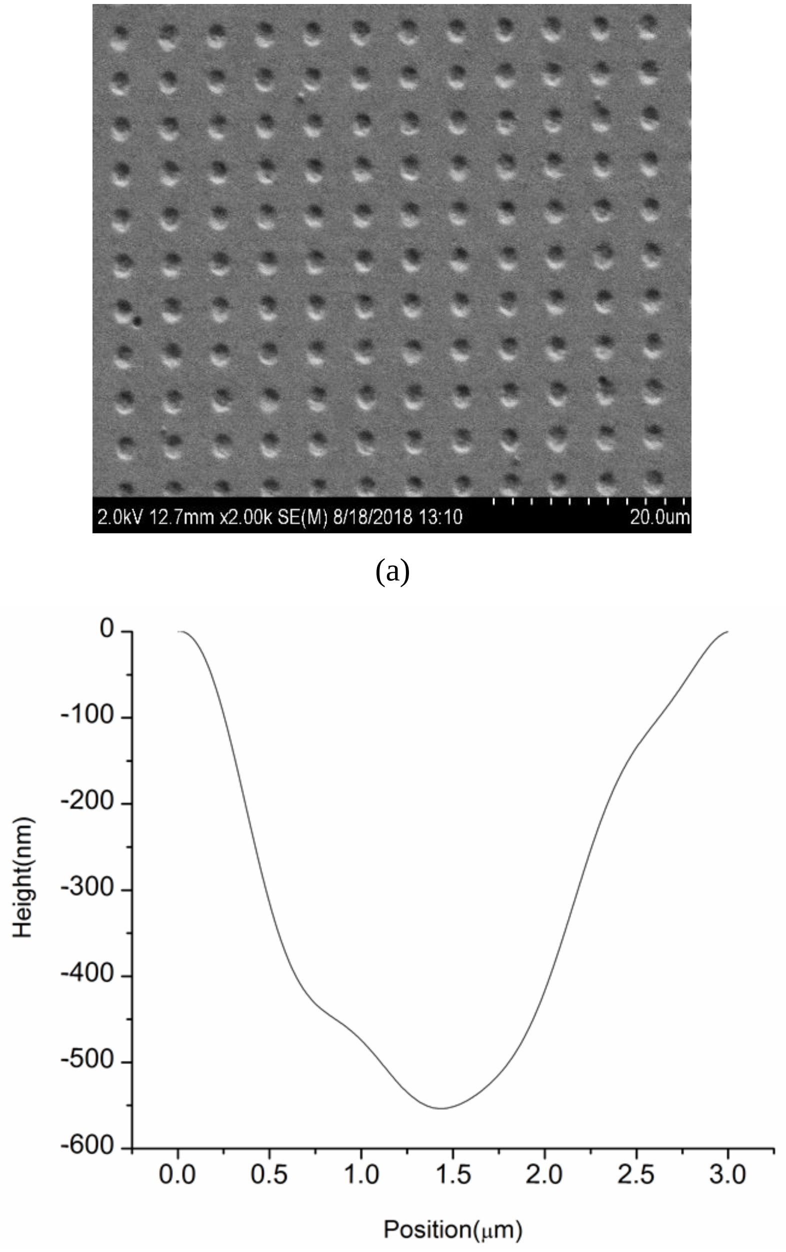

(a)

(b)

Figure 5. 7: (a). Scanning electron microscopy image of a 1.5mm thick copper film with patterned dimples, (b). AFM line profile of the height change across a single dimple

5.5 Results and Discussions

5.4.1 Standard LIFT technique

Using the model described in Chapter 3, we analyzed the heat dynamics for different values of the laser fluence and film thicknesses and proposed a mechanistic hypothesis for the experimental observations. In Regime 1, the donor film is partially melted, and micro-bumps possibly occur due to the difference in density between the molten and solid region of copper film. Above the melting point of copper, the density of the molten metal decreases with temperature, and the resulting volumetric expansion of the molten copper is constrained by the carrier substrate and the un-melted film. Results in the literature suggest that micro-bumps are generated as a means of relieving the compressive stress in the molten copper, and as such, the bumps tend to have a hollow interior [27]. Figure 5. 8 shows the molten bump solidified in its bulged state as the temperature of the liquid metals falls below the melting point of the copper film. In Regime 2, the melt front reaches the free surface while the film-substrate interface temperature remains below the boiling point of the copper film. The molten metal at the free surface can expand without mechanical constraint to for surface protrusion as seen in Figure 5. 9. In regime 3 and 4, the laser fluence is high enough to induce vaporization, it is possible that similar features may be the result of partial vaporization of the donor film, as shown in Figure 5. 10.

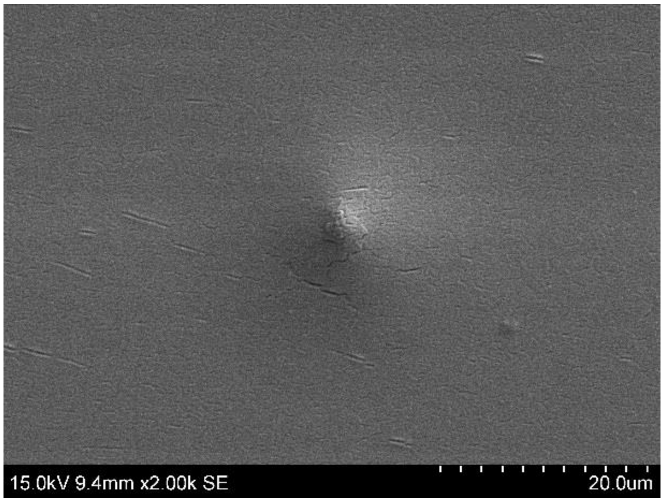

Figure 5. 8: Atomic force microscopy height profile of a single bump

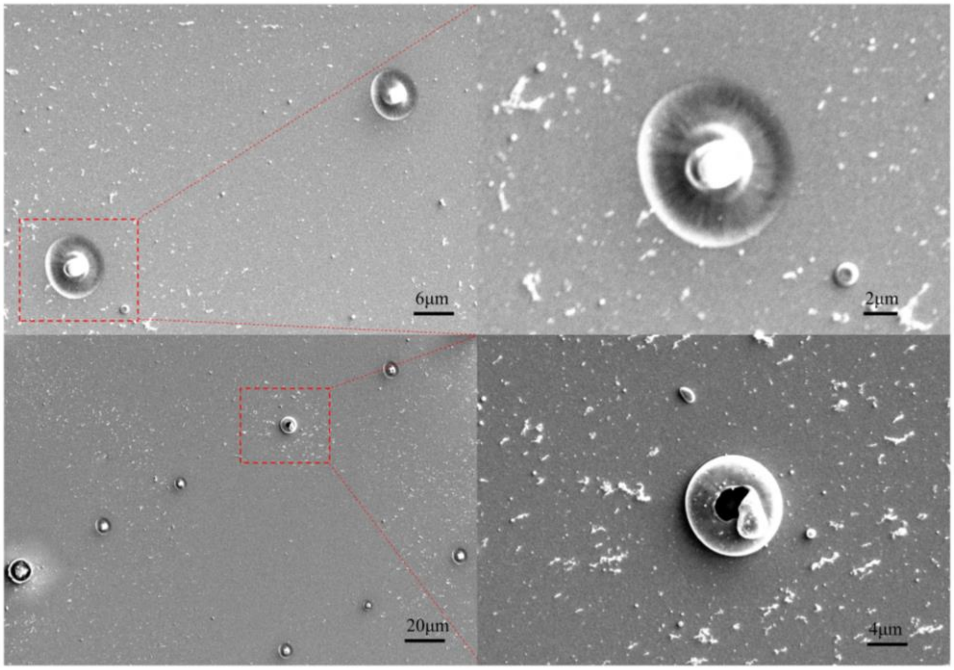

Figure 5. 9: SEM images of Regime2 features on the non-patterned 800 nm donor film

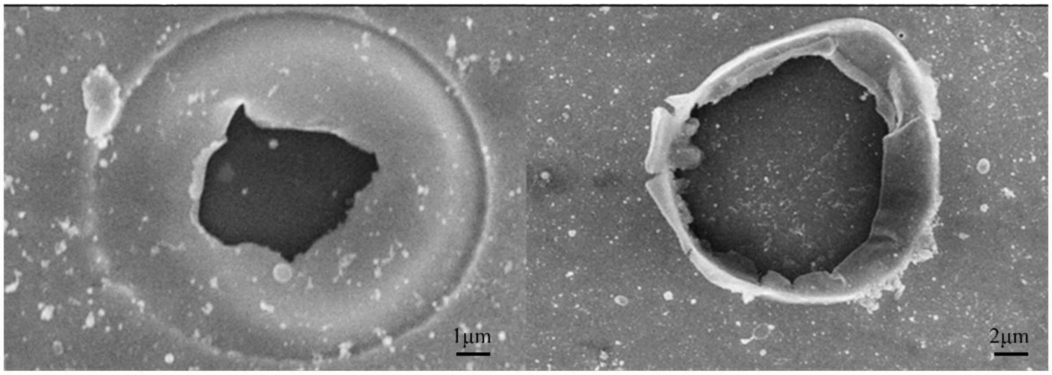

Figure 5. 10:. SEM images of Regime3&4 features on the non-patterned 800 nm donor film

The SEM image in Figure 5. 11 shows the droplets on the target substrate at 20 kJ/cm^2. There exist numerous droplets deposited on the target substrate. The droplet size is between 1~2μm, which is much smaller than the spot size (15μm) because of the breakup of needlelike jets. Furthermore, it can be notices that the droplets are dispersed over the place, another notorious drawback of LIFT process has been confirmed in this experiment, which is high angular divergence of ejected droplets

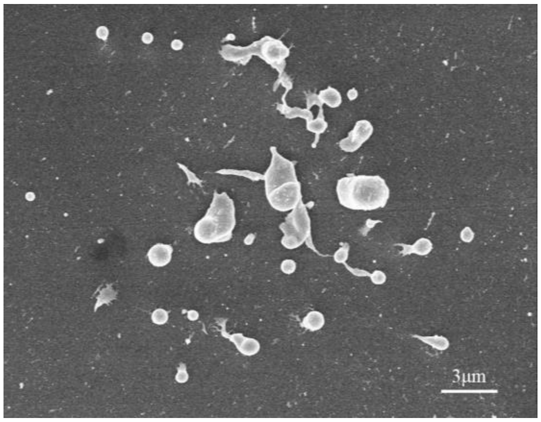

Figure 5. 11: SEM images of spreaded droplets landed on receiver target substrate

5.4.2. Patterned LIFT technique

Figure 5.12-5.17 show a set of SEM images of the patterned copper donor film with 1.5 μm thickness, after irradiating the film-substrate interface with a single laser pulse. Depending on the input fluence, impulsive heating of the donor film leads to the formation of micro-bumps, frozen micro-jets, or ruptured blisters. In Figure 5. 12, the micro-bumps and ruptured blisters are observed at a laser fluence of 9.2 J/cm^2 and 12.0 J/cm^2 respectively. Figure 5. 13 shows representative micro-bump geometries obtained at different locations on the donor film. The circular micro-bumps have a small protrusion at the location of the film aperture. Figure 5. 14 shows a height profile taken with a tapping mode atomic force microscope (AFM) tip across one of the bumps. The image is saturated near the protrusion where the height of the sample exceeds the limit of the AFM probe (~2μm). Two line scans of the height change on the bump taken away from the saturation points show that the width of the bump is close to 12 μm, and the maximum height change is 1.4 μm. Increasing the input laser fluence close to 10 J/cm^2 leads to the extension of the protrusion into a vertical micro-jet that is frozen in place, as shown in Figure 5. 15. The apparent height of the micro-jets is up to 5 μm and the diameter is between 2 and 3 μm. When the laser fluence is increased to 12.0 J/cm^2, the micro-jet is ripped from the micro-bump leaving a hollow bump or the entire micro-bump is torn from the edge, as seen in Figure 5. 16. Figure 5. 17 shows SEM images of droplets transferred to the silicon target substrate at a laser fluence slightly above the threshold for the micro-jet formation. Multiple droplets are stacked on top of each other, or in close proximity on the target substrate. In the experiment, the donor film was placed directly on the target substrate. The prominent droplets in the SEM images have diameters in the range of 2 to 3 μm. Figure 5. 18 shows SEM images of the micro-jets formed on the 800 nm donor film. In this case, a lower threshold fluence of 1.8 J/cm^2 was needed for initiation of the micro6 jets. Figure 5. 19 shows images of individual droplets transferred to the target substrate without the random splatter pattern obtained with the 800 nm thick donor film. The single droplets in the image are circular in shape and have a diameter of close to 2.8 μm and a thickness of 600 nm. To confirm that the formation of the protruded micro-jet is associated with the presence of the apertures in the donor film, the experiments were repeated on the un-patterned 800 nm thick donor film. The SEM images of the donor film after irradiating sample with the pulsed laser are shown in Figure 5. 9. Two types of patterns are obtained namely, a frozen protrusion surrounded by an annular recession in the film, and a torn blister. The latter is obtained at a laser fluence slightly above 1.8 J/cm^2. The apparent differences in the geometry of the frozen jets obtained in the patterned and un-patterned films suggest that the aperture plays a role in the formation of the protruded micro-jet.

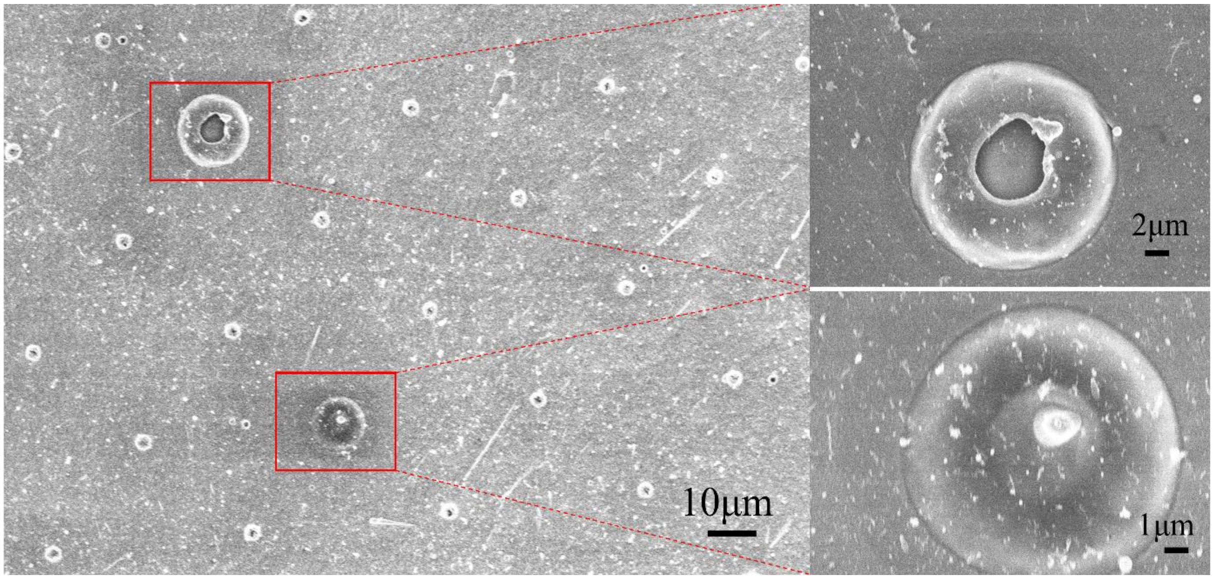

Figure 5. 12: Scanning electron microscopy images of features in place on the 800nm thick donor film

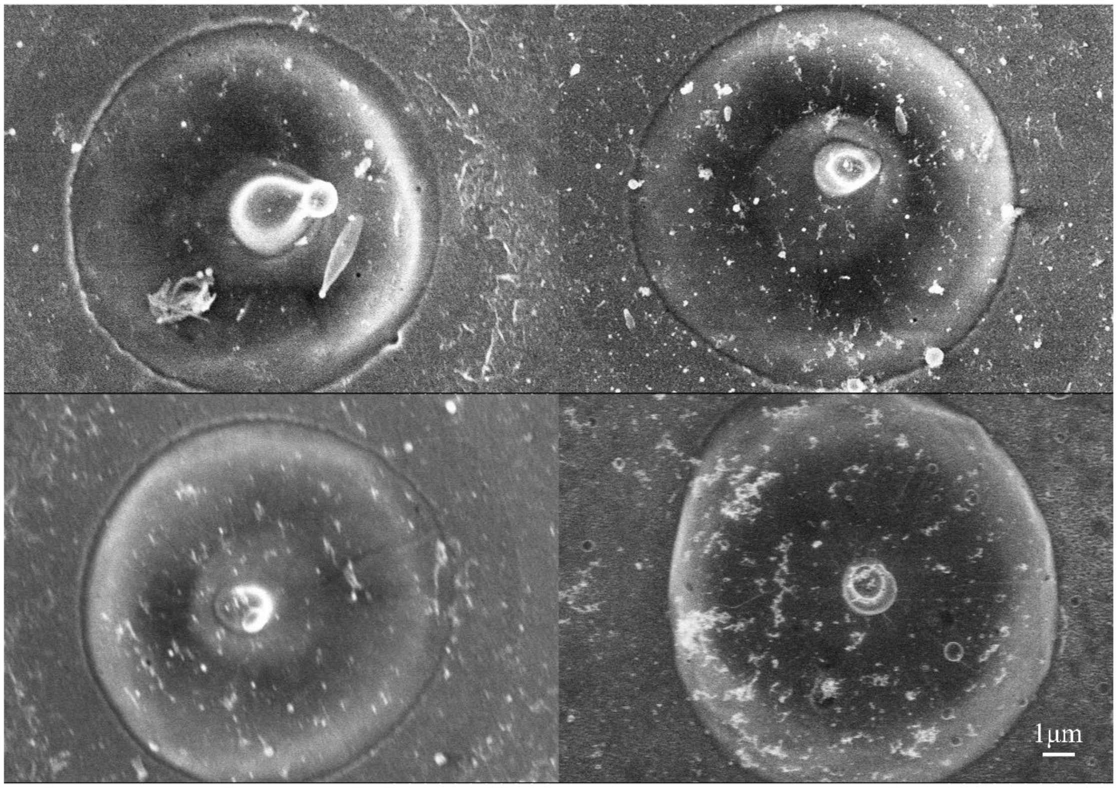

Figure 5. 13: Scanning electron microscopy images of micro-bumps generated on the film for an input fluence of 9 J/cm^2

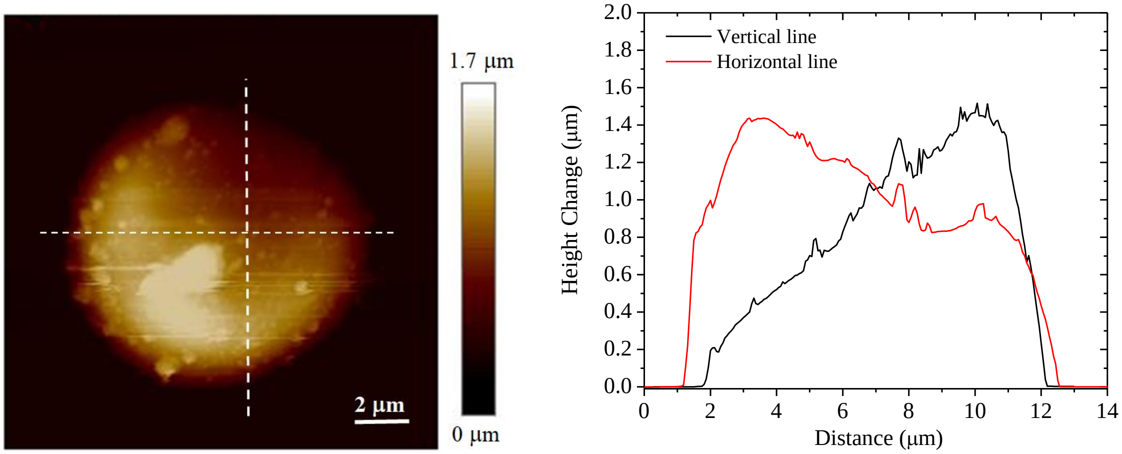

Fig. 50

Figure 5. 14: Atomic force microscopy height profile of a single bump

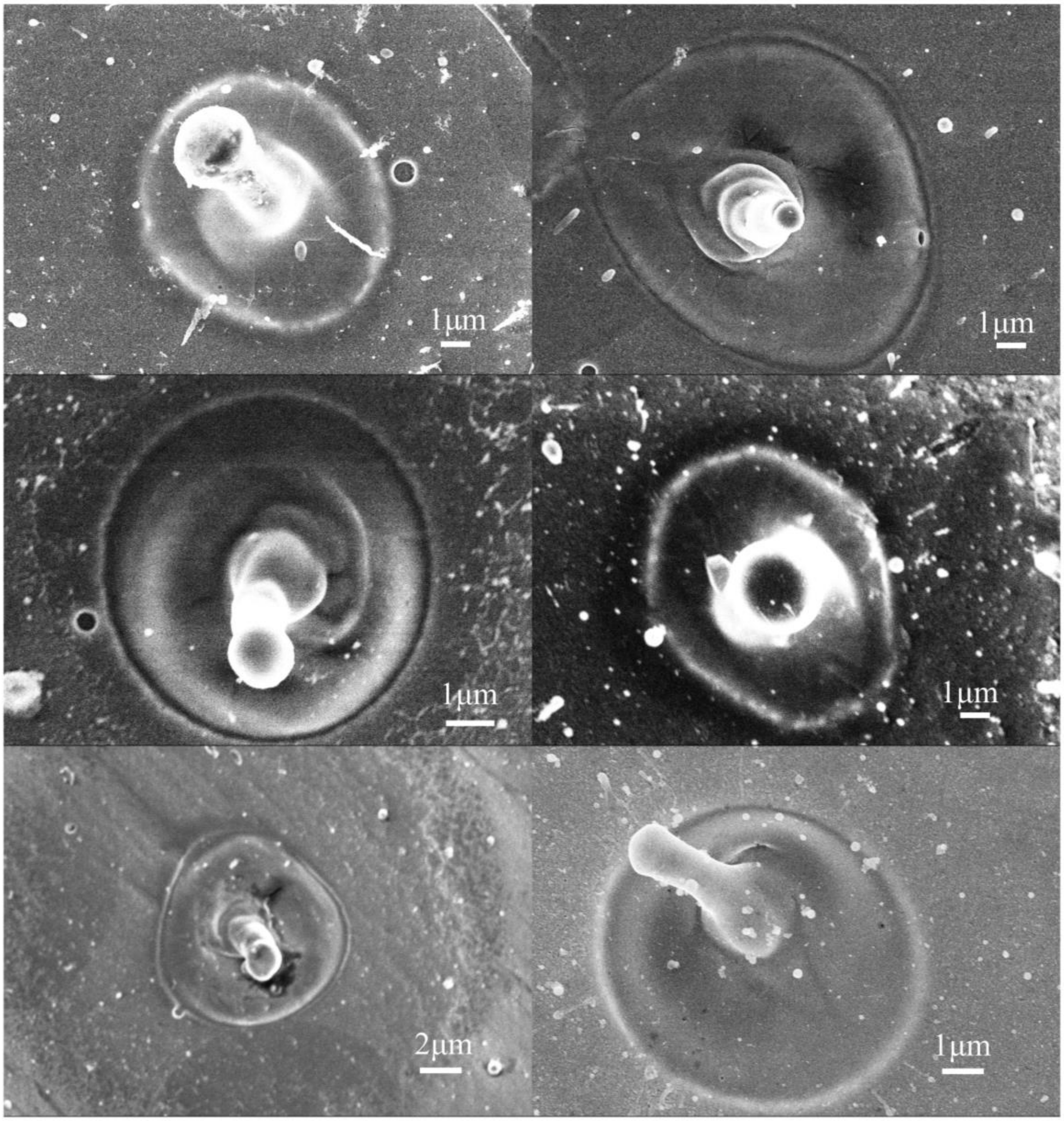

Figure 5. 15: Scanning electron microscopy images of vertical micro-jets frozen in place on the 1.5 μm thick donor film for a laser fluence close to 10 J/cm^2

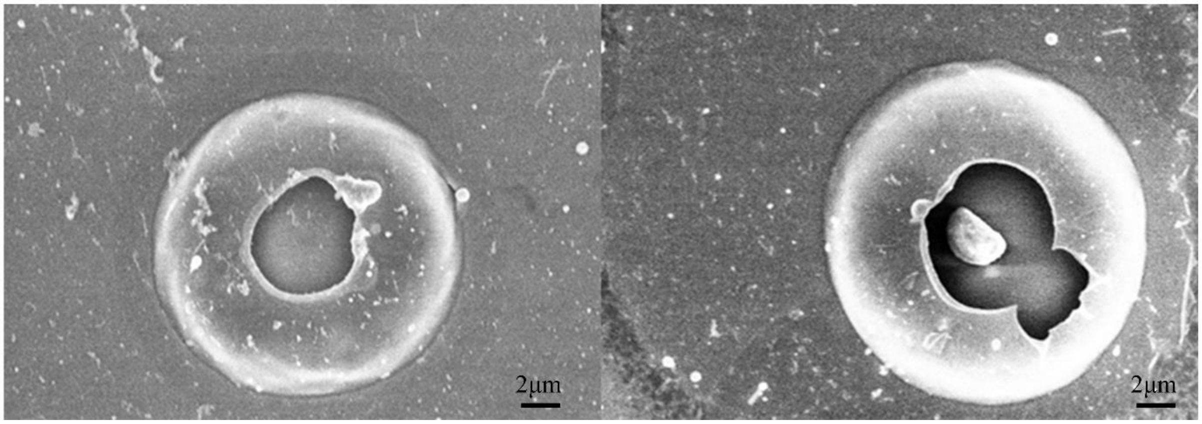

Figure 5. 16: Film fracture patterns obtained for a laser fluence close to 12 J/cm^2

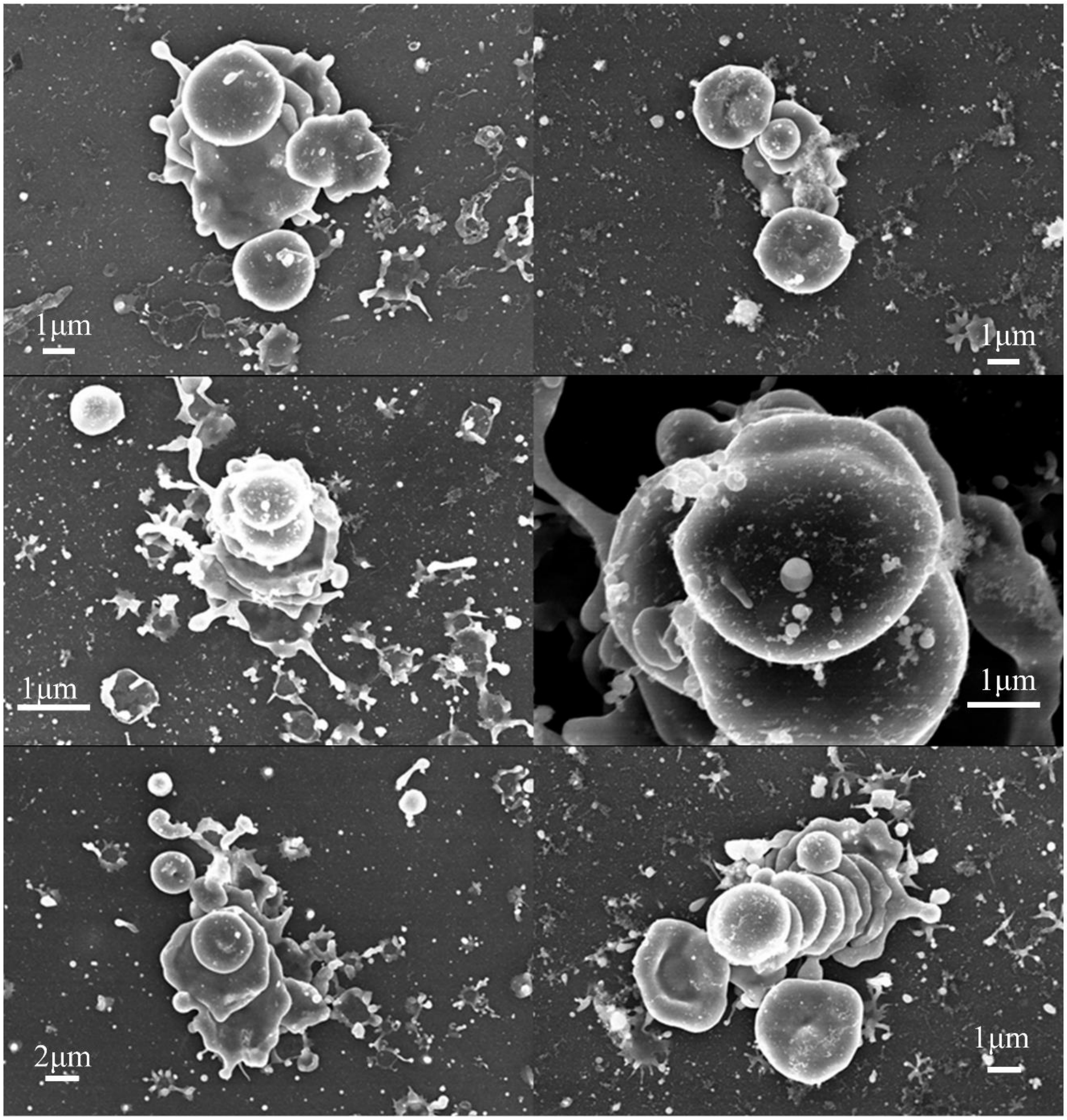

Figure 5. 17: Scanning electron microscopy images of metal droplets transferred to a silicon target substrate

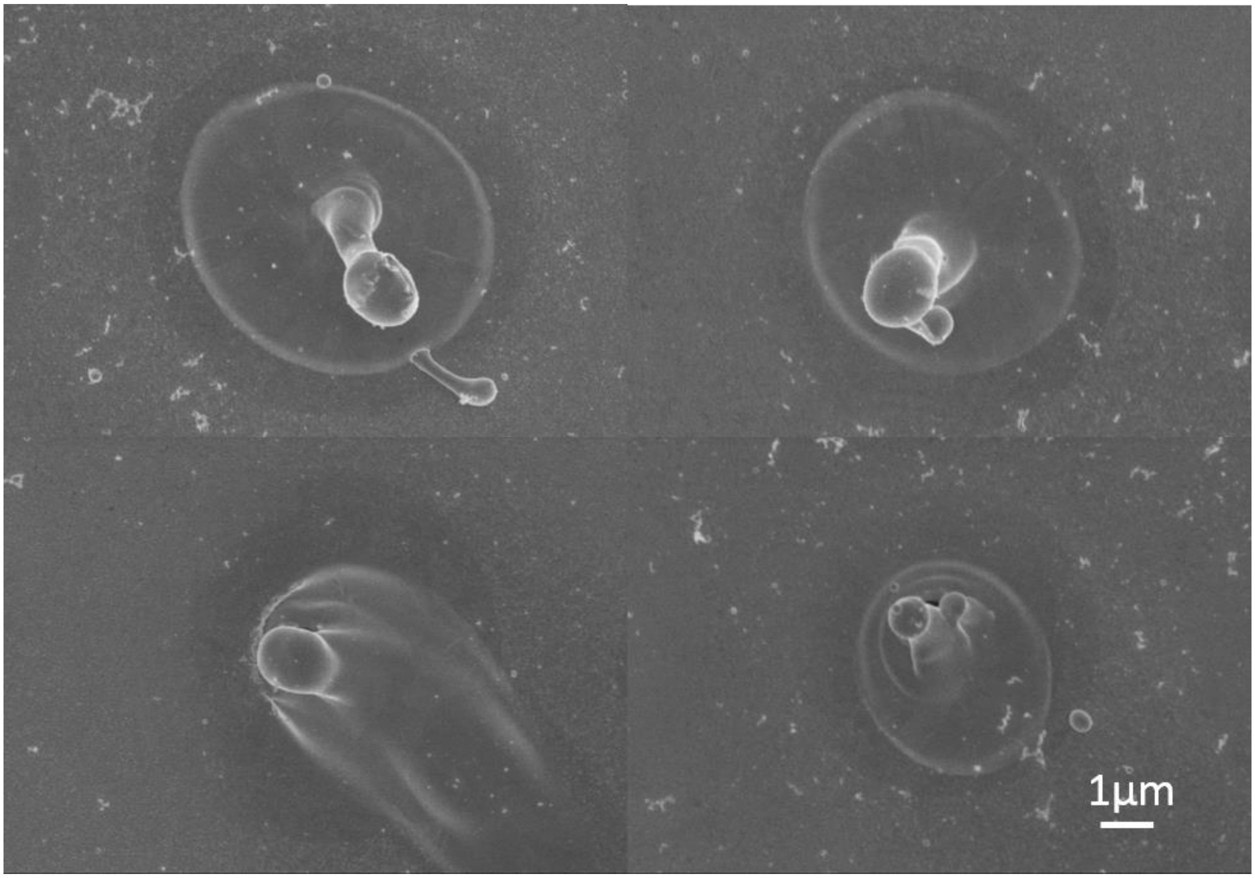

Figure 5. 18: Scanning electron microscopy images of vertical micro-jets frozen in place on the 800nm thick donor film

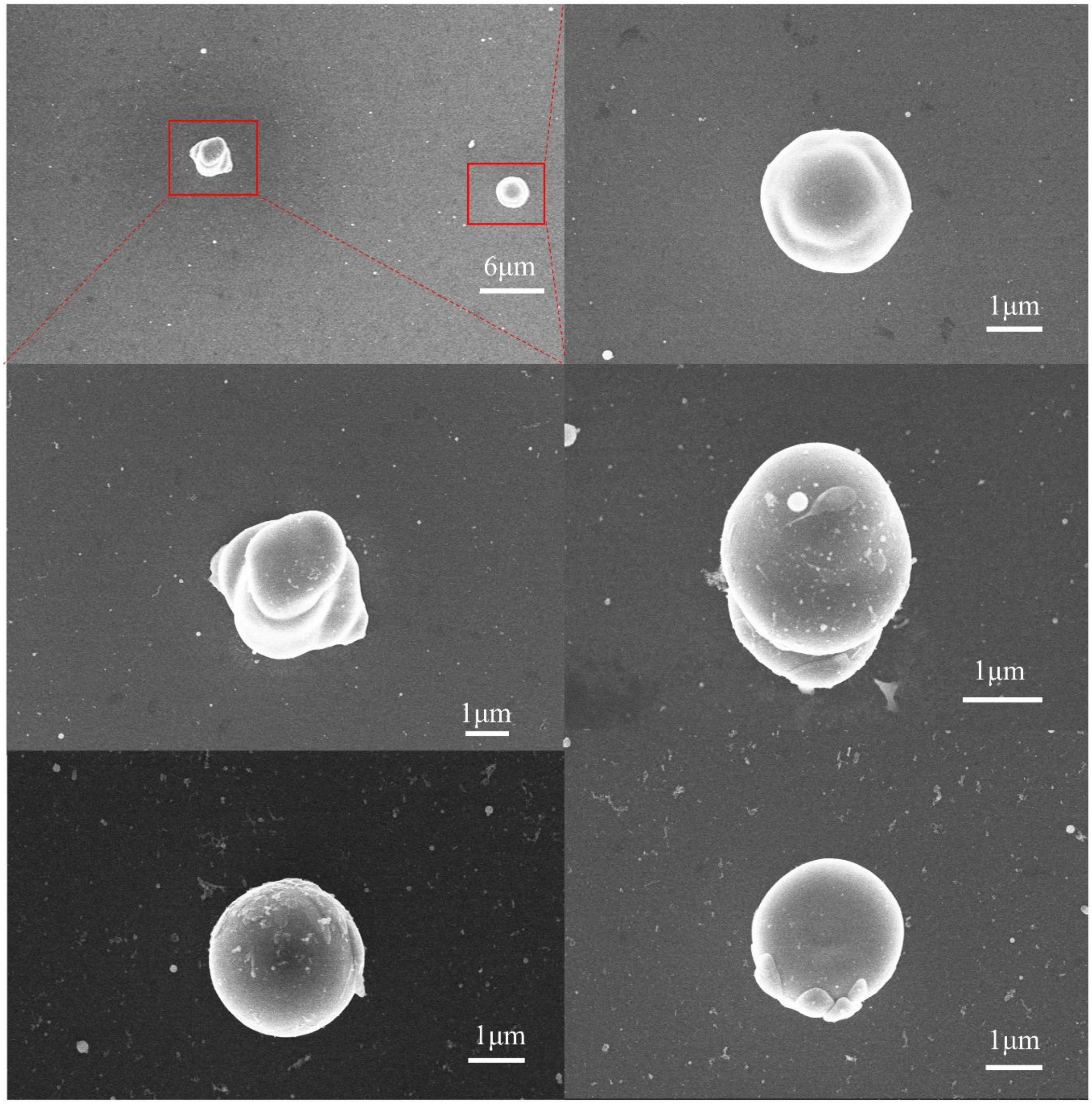

Figure 5. 19: Scanning electron microscopy images of copper droplets transferred to the target substrate.

Chapter 6

Conclusions and Recommendations

6.1 Conclusions

In conclusion, an aperture-based LIFT approach is explored to transfer individual droplets from an impulsively melted donor film to the target substrate. Using a donor film thickness of 800 nm with pre-patterned apertures terminated at the depth of 400 nm from the free surface, we are able to transfer individual droplets with sizes in the range of 2-3 μm to the target substrate. For the 800 nm, heating with a nanosecond laser pulse produces a near-uniform temperature within the film. The presence of the aperture leads to the formation of micro-jets of molten metal that either freeze in place as vertical columns, or are broken up into droplets ejected towards the target substrate. An axisymmetric heat conduction model is used to predict the temperature distribution with the heated film and to provide a qualitative explanation of the features observed in the donor film in our experiments. Further modeling work that couples the mechanical deformation of the un-melted donor film, the dynamic flow of molten metal through the aperture, and the temperature distribution in the film, will provide new insight into the complicated physics involved in the formation of the micro-bumps and molten microjets, and allow for controlling the size and landing accuracy of the droplets transferred to the target substrate. The results presented in this work suggest that the aperture based LIFT approach may have potential for microscale surface engineering of thin films for applications in sensing and catalysis, and controlled transfer of microscale metal particles for applications in microscale ballistics.

6.2 Recommendations

Further work needs to be done both numerically and experimentally.

To ensure the model is complete and robust, the following are some recommendations that can be investigated as a continuation of this research:

i. Transient injection velocity is recommended to be fetched from the thermal model due to the phase change of the metal material, this transient velocity is the time dependent injection velocity in the simplified hydrodynamic model. In that way, a more realistic model can be built up to represent the jetting profile.

ii. Improve the hydrodynamic model by coupling the deformation of the copper film. In the current research work, the copper film is assumed to be rigid which is not affected by the expansion of the metal material. However, in reality, the expansion of the fluid may widen the aperture size. Therefore, a fluid structure interaction model needs to be investigated on the interaction between the solid film and the molten metal.

iii. Investigation of the droplet impact on the target substrate at certain gap distance. Provided the ejection velocity and size of the droplet from the donor film, how the impact will influence the landing droplet size and adhesion between two droplets will be the next challenge to be overcome.

Provided the strong background on the numerical understanding of LIFT, to take a further step on the experimentally printing methodology, the following are some recommendations that can be explored:

i. Time resolved imaging system is necessary to further study the droplet formation, ejection and landing on the target substrate.

ii. A three dimensional structure is recommended to be built up with the optimization of the laser fluence, film thickness and aperture characterization.

iii. Investigation on the various shape of the mask. Instead of having aperture on the donor film, triangle mask and square mask are worthwhile to be tested to diverse the printing geometry.

Chapter 7

Appendices

7.1 Blister actuated LIFT approach

7.1.1 Finite element modeling of blister deformation

The dynamic response of the blister cavity created by partial melting and vaporization of the film is calculated by feeding the time dependent temperature calculations into an explicit FE model in ABAQUS. The blister deformation is calculated by modeling the film as a circular thin plate. The initial radius of the blister cavity *is* a_0, defined by the size of the vapor cavity from the temperature calculations. Influence of the membrane force cannot be neglected in the analysis of blistering deformation, a certain amount of residual stress is developed from the E-beam evaporation method and a possibility of large deformation can generate a transverse component from the membrane force. Meanwhile, a certain amount of residual stress is developed in the deposition process, the presentation of residual stress has to be considered. The time dependent nonlinear elastic deformation of the thin plate is obtained by solving the Foppl-Von Karman equation expressed below in polar coordinates [73],

$$D\nabla^4 w + \rho\frac{\partial^2 w}{\partial t^2} = h\left((\frac{1}{r}\frac{\partial\varphi}{\partial r} + \frac{1}{r^2}\frac{\partial^2\varphi}{\partial\theta^2})\frac{\partial^2 w}{\partial r^2} + \frac{\partial^2\varphi}{\partial r^2}\frac{\partial^2 w}{\partial\theta^2} - 2\frac{\partial}{\partial r}(\frac{1}{r}\frac{\partial\varphi}{\partial\theta})\frac{\partial^2 w}{\partial\theta\partial r}\right) + p(t) \tag{7.1}$$

where, $D = Eh^3/12(1-\gamma^2)$ is the film's flexural rigidity, E is the Young's modulus, γ is the Poisson's ratio, h is the film thickness, φ is the Airy stress function, r and θ are position variables in the plane of the film, and $w(r,\theta,t)$ is the film deflection. The source term $p(t)$ is the excess cavity vapor pressure, i.e. the difference between the cavity vapor pressure and atmospheric pressure, which is assumed to be uniform in the depth directions. The following boundary conditions, $w(r,\theta,t) = 0$,

$\frac{\partial w}{\partial r}$=0, at $r = a_0$ is applied. The solution to Eq. 7.1 yields the transient blister defection due to the excess cavity vapor pressure in the cavity. The calculated deflection is corrected for the linear thermal expansion of the solid film, $\nabla V = \alpha_v V \Delta T$, where V is the volume of the solid portion of the film, and ΔT is the calculated film temperature change.

In the FE numerical calculations, the source term $p(t)$ is obtained in a piecewise fashion since it depends on the heat input from the pump laser. First, at the beginning of each calculation time step (t_0), the volume of the vapor cavity $V(t_0)$ is determined from FDTD temperature calculations up to t_0. The cavity is assumed to be filled with vapor and the volume is time dependent. Next, heat is added to the system through the heat equation at a constant volume and the new average cavity temperature $T(t_0)$ and volume are calculated. The cavity volume at the beginning of the numerical calculation $V(t=0)$ is zero, since vaporization does not occur instantaneously as observed in the temperature calculations. The corresponding cavity pressure $P(t_0)$ is determined using the ideal gas model,

$$P(t) = \frac{R}{M}\frac{m(t)T(t)}{V(t)} \tag{7.2}$$

where m *and* M are the vapor and molar masses, T and P are the average vapor temperature and pressure, and R is the ideal gas constant. Using $P(t_0)$, the deformation of the blister cavity is calculated. At the end of the time step, the volume of the cavity increases from $V(t_0)$ to $V(t_1)$ due to the blister deformation and thermal expansion, where $t_1 = t_0 + \Delta t$. The vapor inflator property in ABAQUS FE, provides the time dependent vapor mass in the cavity, based on the prior calculation of vapor mass flow rate $\dot{m}(t)$, i,e., $m(t) = \int_0^{tn} \dot{m}(t)dt$, where t_n is the current simulation time.

The corresponding cavity pressure $P(t_1)$ at the beginning of the next time step t_1, is recalculated based on the ideal gas model,

$$P(t_1) = \frac{P(t_0)V(t_0)m(t_1)T(t_1)}{V(t_1)m(t_0)T(t_0)} \tag{7.3}$$

The approach described is repeated from time step to time step to construct the time dependent cavity pressure, volume, and blister displacement profile.

7.1.2 Cohesive Zone Modeling of Interface Fracture

The film substrate interface is modeled as a cohesive zone. Elastic deformation of the film creates stress concentration at the interface, which combined with the laser induced cavity pressure, leads to delamination at the interface. An interface crack separating the film from the substrate advances along the interface as the cavity pressure increases. Film interfacial fracture typically involves a combination of local model I (tension) and modes II and III (in-plane and out-of plane shear) effects, which can be modeled using either linear elastic fracture mechanics (LEFM) [74] or cohesive zone modeling (CZM) [74]. The latter is preferred because it can be used to predict crack nucleation at corners between biomaterials [75]. In the CZM, the constitutive behavior of the interface is assumed to follow a traction-separation law that characterizes the fracture toughness and strength of interfacial adhesion. Figure 7. 2 shows a schematic of a 2D cohesive zone and the traction separation law. The interface traction σ consists of normal and shear stress components σ_n and σ_t, such that, $\sigma = \sqrt{\sigma_n^2 + \sigma_t^2}$. The relative displacement across the interface δ, also have normal δ_n and shear δ_t crack opening displacements, where, $\delta = \sqrt{\delta_n^2 + \delta_t^2}$. The traction separation law consists of a linear elastic response with stiffness K, until the traction reaches the interfacial strength, at which damage initiates at the interface and strength softening occurs.

Following the approach by Cao *et al.* [76], the softening process is described by a damage parameter D that increases from 0 representing the case of no damage to 1 representing complete damage. The traction-separation law is described by the relationship, $\sigma_i = (1 - D)K\delta_i, \quad i = n, t$, throughout the fracture process. The interface fracture toughness is given by the area under the traction-separation relation. The interface damage initiation criteria used in this work is based on the maximum stress criterion,

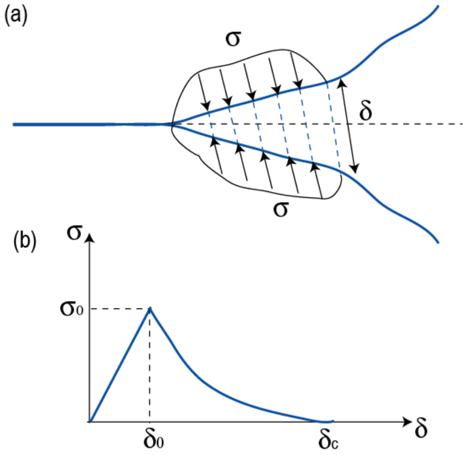

Figure 7. 2: A schematic of a 2D cohesive zone and the traction separation law

$$max\left\{\left|\frac{\sigma_n}{\sigma_n^0}\right|,\left|\frac{\sigma_t}{\sigma_t^0}\right|\right\}=1, \tag{7.4}$$

where σ_n^0 and σ_t^0 are the normal and shear interfacial strengths. The softening parameter is described by an exponential function [74],

$$D_s=1-\frac{\delta_0}{\delta_m}\left\{1-\frac{\exp\left(-\alpha\frac{\delta_m-\delta_0}{\delta_c-\delta_0}\right)}{1-\exp(-\alpha)}\right\}, \tag{7.5}$$

where δ_m is the maximum interface separation, α is a shape parameter, and δ_c is the critical separation, which is directly related to the interface fracture toughness. The CZM is implemented in the FE model.

7.1.3 Numerical results of blister dynamics

Figure 7. 3 shows a snapshot of the blister displacement for the copper film using an input laser fluence of 0.8J/cm^2, 0.88J/cm^2 and 0.96J/cm^2 on the film substrate interface, and the initial cavity radius is 40 μm. Before digging into the details of the blistering, the traction separation law of the cohesive interface has to be considered. For convenience, the traction-separation law used in the numerical calculation is limited to normal traction forces, applied to the cohesive elements closest to the crack zone. It is assumed to be bilinear, and the linear stiffness in the CZM is assumed to be K = 2.0x 10^{14} N/m. The interface strength and fracture toughness used in the model are two critical parameters for the interfacial parameters. Sensitivity analysis on the influence of strength and toughness has been tested as shown in Figure 7. 3. Under certain fixed amount of load, a bunch of tests with two varying parameters have been done. Each pattern in the figure represents different adhesive strength, and delamination length. Observation tells that for different adhesive strength, they almost follow the same trend of the adhesive energy dependent delamination length. It turns out that adhesive energy is a more sensitive parameter compared with the strength. So far, the adhesive energy is from the literature estimates, in the later future, a simple adhesive test will be run to confirm the adhesive energy between the substrate and the thin film.

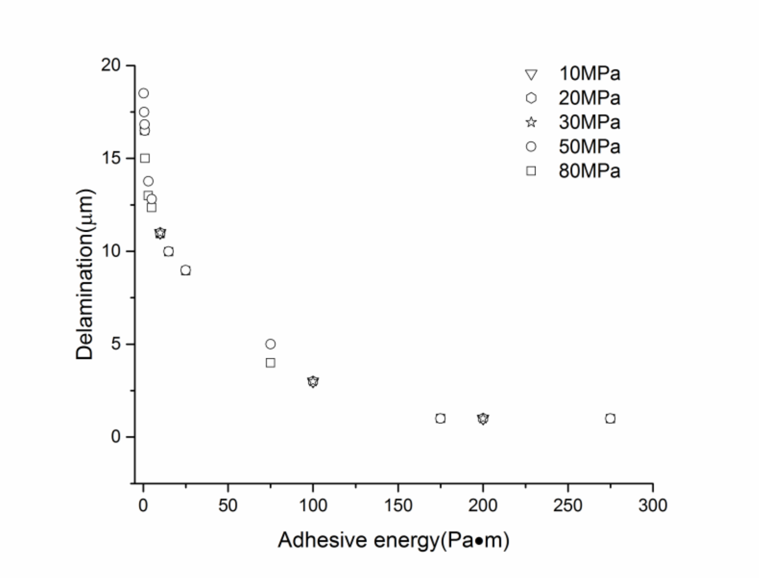

Figure 7. 3: Sensitivity analysis on adhesive strength and adhesive energy of the interfacial property

In the calculated blistering results, three sets of numerical simulation have been conducted, as shown in Figure 7. 4. It can be noticed, for all experiments, the blister height increases rapidly to a maximum of close to 4.5 μm, 5.25 μm and 7.12 μm within the first 15ns, and is followed by an underdamped oscillatory displacement respectively. The vibration frequency, for each case, are 5.72MHz, 7.57MHz, and 8.34MHz. While the numerical results appear to capture the expected dynamics, i.e. steady state blister vibration super-imposed on a transient film height change, the full CZM described in section 7.1.2 will be fully implemented and validated based on experimental measurements of the blister displacement. These calculations will enable prediction of the spatial extents of melted and vaporized metal, and the dependence of the blister cavity vapor pressure on the laser fluence. Since the blister displacement dynamics is correllated to the time dependent vapor pressure, experimental measurements of the blister displacement can be used to validate the numerical prediction of the time dependent vapor pressure.

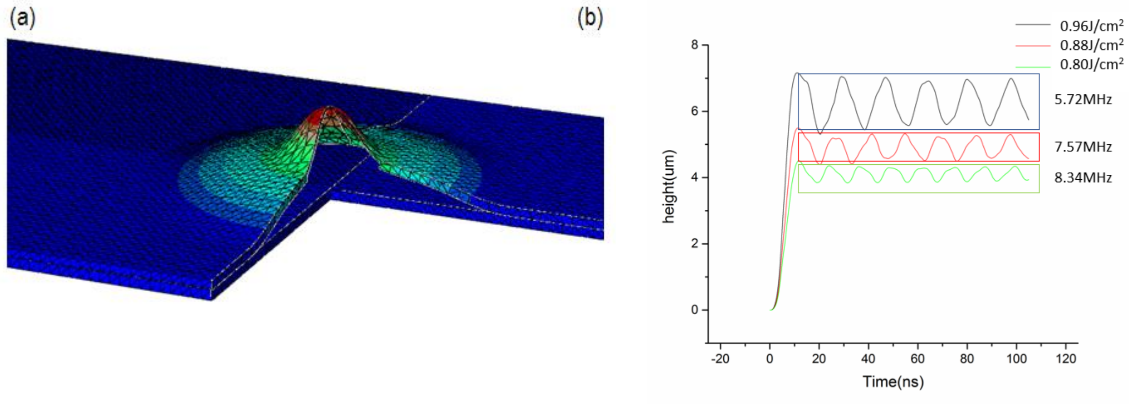

Figure 7. 4: (a) Snapshot of blister displacement at 50ns, (b) time resolved surface displacement at center of blister. Bright red region in (a) has the largest displacement.

7.1.4 Experimental characterization of the blister dynamics and size as a function of pump laser fluence

Time resolved images of the blister shape will be captured for validation of the modeling work developed. Specifically, the shape of the laser generated blister will be obtained as function of pump laser fluence at the donor-carrier interface for different metal films (for example, titanium, copper, chromium, gold, and aluminum). The FE numerical model developed will be matched to time dependent blister dynamics to predict the time dependent vapor pressure within the cavity. Additional experimental mechanics measurements using the peel test will be used to determine the appropriate properties for the cohesive zone model. A displacement Michelson interferometer is used to measure the blistering dynamics. In the experiment, the 1064 nm pump laser is focused at the interface between a 500nm thick titanium film and a soda lime glass substrate. The focused spot size of the pump laser is approximately 200 μm. The normal surface displacement of the film was obtained by focusing a CW laser on the top surface of the film, and redirecting the reflected light into the interferometer. At a pump laser fluence to 967 mJ/cm^2, the interferometer signal (see Figure 7.4(a) shows several transient spikes larger than the noise floor, and for several microseconds. The oscillations are due to vibration modes of a blister produced in the film, and signal folding that occurs when the interferometer moves through multiple fringes as the surface displacement becomes larger than the probe source wavelength (532nm). To confirm that a blister is generated, an additional experiment was performed at a laser fluence below the blistering threshold, where laser induced differential thermal expansion of the debonded film and substrate, leads to transient excitation of a pure blister vibration mode, shown in Figure 7.4(b). The measurement shows a transient thermal expansion followed by beating oscillations with frequencies close to 5.1 MHz and 6 MHz, corresponding to the eigen vibration modes of the blister cavity. Repeating the measurements at lower pump laser fluences sufficient to induce film blistering, led to an increase in the fundamental vibration frequency, as shown in Figure 7.4(c). This can be explained by the fact that the blister width decreases at low fluencies, thus increasing the film bending stiffness. Figure 7.4(d) shows a scanning electron microscopy SEM image of an edge fractured blister obtained at a laser fluence of 1.2 J/cm2. No permanent blister profiles were observed in the SEM images taken for laser fluencies around the blister threshold, suggesting that there is no plastic deformation in the film and the blistered film reattaches to the substrate due to direct loading under atmospheric pressure. At present, the time resolved blister displacements do not agree with the numerical predictions presented. Performing these measurements with the proposed time resolved streak camera in the future, will allow for full-field imaging of blister dynamics, providing representative information for further refinement of the numerical model.

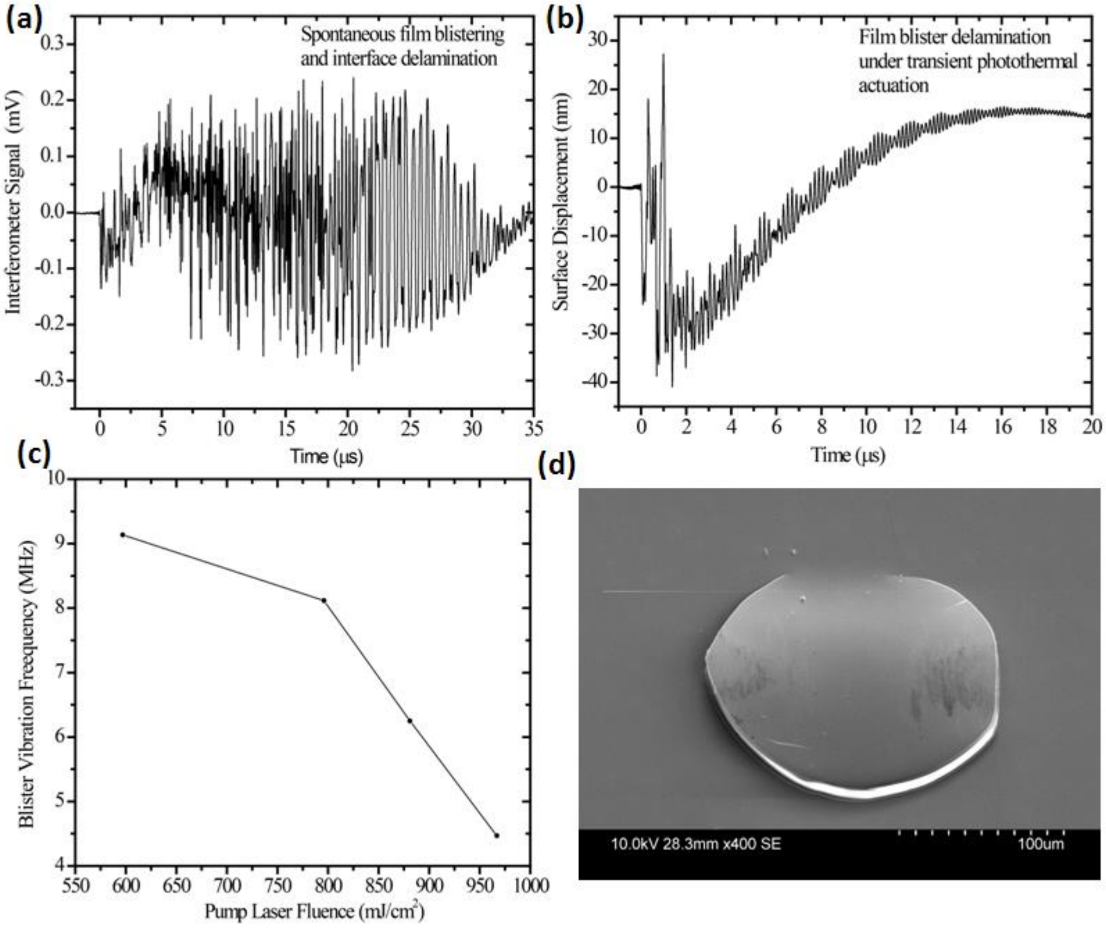

Figure 7. 5: Interferometry measurement of film surface displacement during (a) spontaneous film blistering and (b) post blistering. (c) variation in the blister vibration frequency with pump laser fluence, (d) SEM image of edge fractured blister obtained at a pump laser fluence of 1.2 J/cm^2.

REFERENCE

[1] Huang, Y., Leu, M. C., Mazumder, J. & Donmez, A. Additive Manufacturing: Current State, Future Potential, Gaps and Needs, and Recommendations. *J. Manuf. Sci. Eng.* **137,** 014001 (2015).

[2] Jurrens, K. & Energetics Incorporated. Measurement Science Roadmap for Metal-Based Additive Manufacturing. *Addit. Manuf.* 86 (2013). doi:10.1007/s13398-014-0173-7.2

[3] Fan, Z. & Liou, F. Numerical Modeling of the Additive Manufacturing (AM) Processes of Titanium Alloy. *Titan. Alloy. - Towar. Achiev. Enhanc. Prop. Divers. Appl.* 3–29 (2012). doi:10.5772/34848

[4] Gu, D. D., Meiners, W., Wissenbach, K. & Poprawe, R. Laser additive manufacturing of metallic components: materials, processes and mechanisms. *Int. Mater. Rev.* **57,** 133–164 (2012).

[5] Melchels, F. P. W. *et al.* Additive manufacturing of tissues and organs. *Prog. Polym. Sci.* **37,** 1079–1104 (2012).

[6] Tekinalp *et al.* Highly Oriented Carbon Fiber in Polymer Composite Structures via Additive Manufacturing . (2014).

[7] Sames, W. J., List, F. A., Pannala, S., Dehoff, R. R. & Babu, S. S. The metallurgy and processing science of metal additive manufacturing. *Int. Mater. Rev.* **61,** 315–360 (2016).

[8] Hanzl, P., Zetková, I. & Daňa, M. Issues of lattice structures production via metal additive manufacturing. *Manuf. Technol.* **17,** 853–857 (2017).

[9] Campoli, G. *et al.* Mechanical properties of open-cell metallic biomaterials manufactured using additive manufacturing. *Mater. Des.* **49,** 957–965 (2013).

[10] 1. Wang, X. *et al.* Topological design and additive manufacturing of porous metals for bone scaffolds and orthopaedic implants: A review. *Biomaterials* **83,** 127–141 (2016).

[11] Yang, L. & Miyanaji, H. Ceramic Additive Manufacturing: a review of current status and challenges. *Solid Free. Fabr. 2017 Proc. 28th Annu. Int.* 652–679 (2017).

[12] Charbonnier, B., Laurent, C. & Marchat, D. Porous hydroxyapatite bioceramics produced by impregnation of 3D-printed wax mold: Slurry feature optimization. *J. Eur. Ceram. Soc.* **36,** 4269–4279 (2016).

[13] Huang, R. *et al.* Energy and emissions saving potential of additive manufacturing: the case of lightweight aircraft components. *J. Clean. Prod.* **135,** 1559–1570 (2016).

[14] Song, Y., Yan, Y., Zhang, R., Xu, D. & Wang, F. Manufacture of the die of an automobile deck part based on rapid prototyping and rapid tooling technology. *J. Mater. Process. Technol.* **120,** 237–242 (2002).

[15] Emelogu, A., Marufuzzaman, M., Thompson, S. M., Shamsaei, N. & Bian, L. Additive manufacturing of biomedical implants: A feasibility assessment via supply-chain cost analysis. *Addit. Manuf.* **11,** 97–113 (2016).

[16] Bohandy, J., Kim, B. F. & Adrian, F. J. Metal deposition from a supported metal film using an excimer laser. *J. Appl. Phys.* **60,** 1538–1539 (1986).

[17] Menezes, V., Mathew, Y., Takayama, K., Kanno, A. & Hosseini, H. Laser Plasma Jet Driven Microparticles for DNA/Drug Delivery. *PLoS One* **7,** 7–12 (2012).

[18] Zergioti, I. *et al.* Time resolved schlieren study of sub-pecosecond and nanosecond laser transfer of biomaterials. *Appl. Surf. Sci.* **247,** 584–589 (2005).

[19] Palla-Papavlu, A. *et al.* Laser induced forward transfer of soft materials. *J. Opt.* **12,** (2010).

[20] Thomas, B. *et al.* Experimental investigations of laser-induced forward transfer process of organic thin films. *Appl. Surf. Sci.* **254,** 1206–1210 (2007).

[21] Grant-Jacob, J. A. *et al.* Micron-scale copper wires printed using femtosecond laser-induced forward transfer with automated donor replenishment. *Opt. Mater. Express* **3,** 747 (2013).

[22] Palla-Papavlu, A. *et al.* Microfabrication of polystyrene microbead arrays by laser induced forward transfer. *J. Appl. Phys.* **108,** 1–7 (2010).

[23] Nakata, Y., Okada, T. & Maeda, M. Transfer of particles by laser-induced forward transfer technique. *Pacific Rim Conf. Lasers Electro-Optics, CLEO - Tech. Dig.* **1,** I52–I53 (2001).

[24] Smits, E. C. P., Walter, A., De Leeuw, D. M. & Asadi, K. Laser induced forward transfer of graphene. *Appl. Phys. Lett.* **111,** 1–5 (2017).

[25] Shaw-Stewart, J. *et al.* Improved laser-induced forward transfer of organic semiconductor thin films by reducing the environmental pressure and controlling the substrate-substrate gap width. *Appl. Phys. A Mater. Sci. Process.* **105,** 713–722 (2011).

[26] Shaw Stewart, J., Lippert, T., Nagel, M., Nüesch, F. & Wokaun, A. Red-green-blue polymer light-emitting diode pixels printed by optimized laser-induced forward transfer. *Appl. Phys. Lett.* **100,** (2012).

[27] Kuznetsov, A. I., Unger, C., Koch, J. & Chichkov, B. N. Laser-induced jet formation and droplet ejection from thin metal films. *Appl. Phys. A Mater. Sci. Process.* **106,** 479–487 (2012).

[28] Banks, D. P., Grivas, C., Mills, J. D., Eason, R. W. & Zergioti, I. Nanodroplets deposited in microarrays by femtosecond Ti:sapphire laser-induced forward transfer. *Appl. Phys. Lett.* **89,** 2004–2007 (2006).

[29] Kordas, K., Bali, K., Leppvuori, S., Uusimki, A. & Nanai, L. Laser direct writing of copper on polyimide surface from solution. *Appl.Surf.Sci.* **154–155,** 399–404 (2000).

[30] Germain, C., Charron, L., Lilge, L. & Tsui, Y. Y. Electrodes for microfluidic devices produced by laser induced forward transfer. *Appl. Surf. Sci.* **253,** 8328–8333 (2007).

[31] Visser, C. W. *et al.* Toward 3D Printing of Pure Metals by Laser-Induced Forward Transfer. *Adv. Mater.* **27,** 4087–4092 (2015).

[32] Oosterhuis, G., Prenen, A. & Huis In't Veld, A. J. Laser induced forward transfer of interconnects for 3D integration. *ECS Trans.* **41,** 81–90 (2012).

[33] Zenou, M. & Kotler, Z. Printing of metallic 3D micro-objects by laser induced forward transfer. *Opt. Express* **24,** 1431–1446 (2016).

[34] Si, Y., Yu, J., Tang, X., Ge, J. & Ding, B. Ultralight nanofibre-assembled cellular aerogels with superelasticity and multifunctionality. *Nat. Commun.* **5,** 1–9 (2014).

[35] Willis, D. A. & Grosu, V. The effect of melting-induced volumetric expansion on initiation of laser-induced forward transfer. *Appl. Surf. Sci.* **253,** 4759–4763 (2007).

[36] Zentrum, L. Formation of microbumps and nanojets on gold targets by femtosecond laser pulses. **881,** 879–881 (2004).

[37] Munoz-Martin, D. *et al.* Laser-induced forward transfer of high-viscosity silver pastes. *Appl. Surf. Sci.* **366,** 389–396 (2016).

[38] Bohandy, J., Kim, B. F., Adrian, F. J. & Jette, A. N. Metal deposition at 532 nm using a laser transfer technique. *J. Appl. Phys.* **63,** 1158-1162 (1988)

[39] Shugaev, M. V. & Bulgakova, N. M. Thermodynamic and stress analysis of laser-induced forward transfer of metals. *Appl. Phys. A Mater. Sci. Process.* **101,** 103–109 (2010).

[40] Rapp, L., Constantinescu, C., Larmande, Y., Alloncle, A. P. & Delaporte, P. Smart beam shaping for the deposition of solid polymeric material by laser forward transfer. *Appl. Phys. A Mater. Sci. Process.* **117,** 333–339 (2014).

[41] Pohl, R., Jansink, M., Römer, G. R. B. E. & Huis in 't Veld, A. J. Solid-phase laser-induced forward transfer of variable shapes using a liquid-crystal spatial light modulator. *Appl. Phys. A Mater. Sci. Process.* **120,** 427–434 (2015).

[42] Blanchet, G. B., Loo, Y.-L., Rogers, J. A., Gao, F. & Fincher, C. R. Large area, high resolution, dry printing of conducting polymers for organic electronics. *Appl. Phys. Lett.* **82,** 463–465 (2003).

[43] Banks, D. P., Grivas, C., Zergioti, I. & Eason, R. W. Ballistic laser-assisted solid transfer (BLAST) from a thin film precursor. *Opt. Express* **16,** 3249–54 (2008).

[44] Tolbert, W.A., Lee, I.-Y.S., Doxtader, M.M., Ellis, E.W., and Dlott, D.D. High-speed color imaging by laser ablation transfer with a dynamic release layer: fundamental mechanisms. J. Imaging Sci. Technol., 37 (4), 411–421 (1993).

[45] Boutopoulos, C., Tsouti, V., Goustouridis, D., Chatzandroulis, S. & Zergioti, I. Liquid phase direct laser printing of polymers for chemical sensing applications. *Appl. Phys. Lett.* **93,** 2006–2009 (2008).

[46] Dinca, V. *et al.* Polymer pixel enhancement by laser-induced forward transfer for sensor applications. *Appl. Phys. A Mater. Sci. Process.* **101,** 559–565 (2010).

[47] Fardel, R., Nagel, M., Nüesch, F., Lippert, T. & Wokaun, A. Laser forward transfer using a sacrificial layer: Influence of the material properties. *Appl. Surf. Sci.* **254,** 1322–1326 (2007).

[48] Inui, T. *et al.* Laser-induced forward transfer of high-viscosity silver precursor ink for non-contact printed electronics. *RSC Adv.* **5,** 77942–77947 (2015).

[49] Doraiswamy, A. *et al.* Excimer laser forward transfer of mammalian cells using a novel triazene absorbing layer. *Appl. Surf. Sci.* **252,**4743-4747 (2006)

[50] Duocastella, M., Fernández-Pradas, J. M., Serra, P. & Morenza, J. L. Jet formation in the laser forward transfer of liquids. *Appl. Phys. A Mater. Sci. Process.* **93,** 453–456 (2008).

[51] Tsuboi, Y., Kimoto, N., Kabeshita, M. & Itaya, A. Pulsed laser deposition of collagen and keratin. *J. Photochem. Photobiol. A Chem.* **145,** 209–214 (2001).

[52] Colina, M., Serra, P., Fernández-Pradas, J. M., Sevilla, L. & Morenza, J. L. DNA deposition through laser induced forward transfer. *Biosens. Bioelectron.* **20,** 1638–1642 (2005).

[53] Hopp, B. *et al.* Survival and Proliferative Ability of Various Living Cell Types after Laser-Induced Forward Transfer. *Tissue Eng.* **11,** 1817–1823 (2005).

[54] Brown, M. S., Kattamis, N. T. & Arnold, C. B. Time-resolved study of polyimide absorption layers for blister-actuated laser-induced forward transfer. *J. Appl. Phys.* **107,** (2010).

[55] Han, T. H., Hah, J. M. & Yoh, J. J. Drug injection into fat tissue with a laser based microjet injector. *J. Appl. Phys.* **109,** 107–110 (2011).

[56] Sopeña, P., González-Torres, S., Fernández-Pradas, J. M. & Serra, P. Spraying dynamics in continuous wave laser printing of conductive inks. *Sci. Rep.* **8,** 1–12 (2018).

[57] Kuznetsov, A. I. *et al.* Laser fabrication of large-scale nanoparticle arrays for sensing applications. *ACS Nano* **5,** 4843–4849 (2011).

[58] Zenou, M., Sa'ar, A. & Kotler, Z. Digital laser printing of aluminum micro-structure on thermally sensitive substrates. *J. Phys. D. Appl. Phys.* **48,** 205303 (2015).

[59] Zenou, M. & Kotler, Z. Printing of metallic 3D micro-objects by laser induced forward transfer. *Opt. Express* **24,** 1431–1446 (2016).

[60] Zenou, M., Sa'ar, A. & Kotler, Z. Laser jetting of femto-liter metal droplets for high resolution 3D printed structures. *Sci. Rep.* **5,** 17265 (2015).

[61] Bogaerts, A., Chen, Z., Gijbels, R. & Vertes, A. Laser ablation for analytical sampling: What can we learn from modeling? *Spectrochim. Acta - Part B At. Spectrosc.* **58,** 1867–1893 (2003).

[62] Bennett, T. D., Grigoropoulos, C. P. & Krajnovich, D. J. Near-threshold laser sputtering of gold. *J. Appl. Phys.* **77,** 849–864 (1995).

[63] Seifert, N., Betz, G. & Husinsky, W. Droplet formation on metallic surfaces during low-fluence laser irradiation. *Appl. Surf. Sci.* **103,** 63–70 (1996).

[64] Seifert, N., Betz, G. & Husinsky, W. Hydrodynamic phenomena during laser irradiation: A finite difference approach. *Appl. Surf. Sci.* **96–98,** 33–38 (1996).

[65] Seifert, N. & Betz, G. Computer simulations of laser-induced ejection of droplets. *Appl. Surf. Sci.* **133,** 189–194 (1998).

[66] Brown, M. S., Brasz, C. F., Ventikos, Y. & Arnold, C. B. Impulsively actuated jets from thin liquid films for high-resolution printing applications. *J. Fluid Mech.* **709,** 341–370 (2012).

[67] Kattamis, N. T., Brown, M. S. & Arnold, C. B. Finite element analysis of blister formation in laser-induced forward transfer. *J. Mater. Res.* **26,** 2438–2449 (2011).

[68] 1.Homma, S., Koga, J., Matsumoto, S., Song, M. & Tryggvason, G. Breakup mode of an axisymmetric liquid jet injected into another immiscible liquid. *Chem. Eng. Sci.* **61,** 3986–3996 (2006).

[69] Riester, D., Budde, J., Gach, C., Gillner, A. & Wehner, M. High speed photography of laser induced forward transfer (LIFT) of single and double-layered transfer layers for single cell transfer. *J. Laser Micro Nanoeng.* **11,** 199–203 (2016).

[70] Papazoglou, D. G., Karaiskou, A., Zergioti, I. & Fotakis, C. Shadowgraphic imaging of the sub-ps laser-induced forward transfer process. *Appl. Phys. Lett.* **81,** 1594–1596 (2002).

[71] Feinaeugle, M., Alloncle, A. P., Delaporte, P., Sones, C. L. & Eason, R. W. Time-resolved shadowgraph imaging of femtosecond laser-induced forward transfer of solid materials. *Appl. Surf. Sci.* **258,** 8475–8483 (2012).

[72] Zenou, M., Sa'Ar, A. & Kotler, Z. Supersonic laser-induced jetting of aluminum micro-droplets. *Appl. Phys. Lett.* **106,** (2015).

[73] L.D. Landau and E.M. Lifshitz, Theory of Elasticity, Third Edition, (Elsevier, Burlington, MA, 1976).

[74] M.L. Williams, "The stress around a fault or crack in dissimilar media", Bull. Seismol. Soc. Am. **49**, 199-204, (1959)

[75] A Needleman, "An analysis of tensile decohesion along an interface", J. Mech. Phys. Solids, **38**, 289-324, (1990)

[76] Cao, Z. *et al.* A blister test for interfacial adhesion of large-scale transferred graphene. *Carbon N. Y.* **69,** 390–400 (2014).